

**Allosteric regulation of bacterial Enzyme I: Toward the discovery of a new class of antimicrobial compounds**

by

**Trang Truc Nguyen**

A dissertation submitted to the graduate faculty  
in partial fulfillment of the requirements for the degree of

DOCTOR OF PHILOSOPHY

Major: Chemistry

Program of Study Committee:  
Vincenzo Venditti, Major Professor  
Amy Andreotti  
Robbyn Anand  
Julien Roche  
Levi Stanley

The student author, whose presentation of the scholarship herein was approved by the program of study committee, is solely responsible for the content of this dissertation. The Graduate College will ensure this dissertation is globally accessible and will not permit alterations after a degree is conferred.

Iowa State University

Ames, Iowa

2021

Copyright © Trang Truc Nguyen, 2021. All rights reserved.

## TABLE OF CONTENTS

	Page
ACKNOWLEDGMENTS .....	iv
ABSTRACT.....	v
CHAPTER 1. GENERAL INTRODUCTION .....	1
CHAPTER 2. THE OLIGOMERIZATION STATE OF BACTERIAL ENZYME I (EI) DETERMINES EI'S ALLOSTERIC STIMULATION OR COMPETITIVE INHIBITION BY $\alpha$ - KETOGLUTARATE.....	6
Abstract.....	6
Introduction .....	7
Results .....	9
Discussion.....	14
Materials and Methods .....	15
References .....	21
Figures .....	24
CHAPTER 3. STRUCTURE ELUCIDATION OF THE ELUSIVE ENZYME I MONOMER REVEALS THE MOLECULAR MECHANISMS LINKING OLIGOMERIZATION AND ENZYMATIC ACTIVITY .....	31
Abstract.....	31
Significant Statements .....	32
Introduction .....	32
Results .....	35
Discussion.....	41
Materials and Methods .....	43
Acknowledgement .....	44
References .....	44
Figures .....	49
Supporting Materials .....	52
Supporting Figures .....	57
Supporting Tables.....	61
Supporting References.....	62
CHAPTER 4. AN ALLOSTERIC POCKET FOR INHIBITION OF BACTERIAL ENZYME I IDENTIFIED BY NMR-BASED FRAGMENT SCREENING.....	64
Abstract.....	64
Introduction .....	64
Results and Discussion .....	67
Conclusion .....	73
Materials and Methods .....	75
Acknowledgement .....	79

References .....	79
Figures .....	83
CHAPTER 5. GENERAL CONCLUSION .....	92
References .....	94

## ACKNOWLEDGMENTS

I would like to express my gratitude and appreciation to my professor Dr. Vincenzo Venditti for giving me the opportunity to work with many exciting projects and providing invaluable guidance throughout this research. His expertise, curiosity, and empathy have inspired and motivated me to successfully complete my study.

I extend my appreciation to the committee members for triggering deeper thoughts and different ideas to approach my research aims. It's my great pleasure to collaborate with Dr. Julien Roche who enthusiastically support me to implement a great technique to tackle one of my challenging research problems. I would like to express my admiration to Dr. Robbyn Annand, a founder of Midwest Retreat for Diversity in Chemistry. I am glad to join the retreat in 2019 and it has impacted my career planning. Many thanks also go out to the support I receive from our collaborators and people in the Chemical Instrumental Facility.

Special thanks to all very smart and interesting members in our lab. I learned not only their working experience but also their unique characteristics. I sincerely enjoyed listening to all sharing in the lab and during our trips to Kansas every year, except 2020. Also, some friends came to work in our lab for a short time but left me with an unforgettable memory.

Finally, I acknowledge the endless support of my big family in Viet Nam for staying healthy and happy so that I could spend time for working and taking care of my small family. I especially share my little achievement during six years with my husband who is extremely busy carving our own path in a foreign country but readily supports my work and taking great care of our kids. To Nguyen and Eric, thanks for being my lovely and energetic boys!

## ABSTRACT

Recent structural studies reveal that protein conformational transitions are fundamental to signaling, enzyme catalysis, and assembly of cellular structures. Understanding how the interconversion between different folded structures affects function is challenging but would create a huge impact in treating a large number of diseases that are linked to signaling cascades or enzymes. Although advanced techniques in structural biology have been well-developed to decipher the effects of changes in structures of biological molecules into their functions, these methods have been applied mostly to low molecular weight systems. Enzymes, however, are typically large oligomeric proteins with complex molecular features, and their function is often regulated by long-range communication between structural domains mediated by substrate binding. Therefore, there is a critical need to increase our understanding of how modulation of the local conformational dynamics upon ligand binding propagates into broader scale inter-domain rearrangements that ultimately determine the function of complex multi-domain proteins. Enzyme I (EI) serves as an interesting model for investigating the interplay between regional dynamics and their dissipating effects.

During my research project, I have developed an NMR-based enzymatic assay to investigate the contribution of the EI monomer-dimer equilibrium in the regulation of its enzymatic activity. In addition, the same method was used to study how the EI oligomerization equilibrium determines pluripotency of the small molecule metabolite  $\alpha$ -ketoglutarate ( $\alpha$ KG) against the enzyme. In a follow-up work, I have investigated the structure and dynamics of the elusive monomeric state of EI. Indeed, although the dimeric state of EI has been deeply characterized for structure, dynamics, and function, the monomeric state of EI is difficult to observe at the experimental conditions commonly used in biophysical approaches. Using a

combination of protein engineering and pressure perturbation, I was able to isolate the monomeric state of EI and perform a comprehensive structural and functional characterization of the enzyme by NMR. My study unveils that the catalytic loops near the dimer interface become disordered upon monomerization and, therefore, fail to bind the substrate in the active site. These data explain why only dimeric EI is active and required for a fully functional phosphotransferase system (PTS). Finally, I have explored the possibility of inhibiting bacterial EI with small organic molecules. PTS is ubiquitous and indispensable in prokaryotes but is absent in eukaryotes. Therefore, blocking the PTS pathway is a possible strategy for the development of new antimicrobial drugs. EI is the first enzyme in PTS and is highly conserved in bacteria. Thus, EI is the ideal target for a screening campaign aimed at inhibiting the PTS pathway. Here, I have used NMR-based fragment screening to identify novel inhibitors of EI. I have found three molecular fragments that allosterically inhibit the phosphoryl transfer reaction catalyzed by EI by interacting with the enzyme at a surface pocket located more than 10 Å away from the active site. My study provides the basis for developing second-generation allosteric inhibitors of EI that can potentially address the antibiotic-resistant problem.

## CHAPTER 1. GENERAL INTRODUCTION

### Background

Enzymes are dynamic molecules and their conformational diversity plays an important role in enzyme catalysis<sup>1-7</sup>, allosteric regulation<sup>8</sup>, and molecular recognition<sup>9-10</sup> in biological processes to sustain life.<sup>11-12</sup> Conformational changes in enzymes take place at different timescales. Bond vibration and side-chain conformational changes occur faster (ps to ns), whereas loop motions required for substrate binding and product release often take longer (ns to  $\mu$ s). Domain motions and allosteric transitions, on the other hand, are much slower ( $\mu$ s to ms). The distribution of this conformational ensembles is dynamic and highly sensitive to changes in external conditions such as binding state,<sup>13</sup> ligand concentration,<sup>14</sup> ionic strength,<sup>15</sup> and posttranscriptional modifications.<sup>16</sup> Therefore, obtaining a deep understanding of the regulatory role played by conformational dynamics is important to gain insight into the dysfunction of disease-related mutants, and the molecular basis of physiological regulatory mechanisms. In addition, carefully examining different factors that trigger conformational changes in biomolecules will open new opportunities in drug design, diagnostics, and protein engineering.<sup>17</sup> While interesting findings on how conformational dynamics regulate the biological function of small proteins have been published recently, our understanding of how the coupling among multiple conformational equilibria determines the activity of multi-domain, multi-subunit systems have not gained much progress. This study combines a multidisciplinary approach that integrates atomic-resolution information obtained by NMR, crystallography, and Molecular Dynamics (MD) simulations with enzyme kinetic assays to shed light on the contribution of local and interdomain conformational equilibria to the biological activity of large multidomain enzymes.

Enzyme I (EI) is the first protein of the bacterial phosphotransferase system (PTS), a signal transduction pathway that is involved in both transport and phosphorylation of a large number of carbohydrates and many important regulatory functions such as chemotaxis, biofilm formation, catabolic gene expression, and cross-talk between carbon and nitrogen metabolisms.<sup>18-20</sup> The signal for all these different regulatory processes is ignited by the phosphorylation of EI by phosphoenolpyruvate (PEP).<sup>21</sup> PEP acts as phosphoryl donor for EI, which, together with the phosphocarrier protein HPr and one of the sugar-specific EIIA/EIIB pairs, forms a phosphorylation cascade that allows phosphorylation of the PTS carbohydrate bound to the membrane-spanning EIIC. As such, the regulatory functions of PTS are strongly impaired by malfunctioning of EI. The crystal structure of EI shows that it is a 128-kDa dimer of identical subunits comprising two structurally and functionally distinct domains. The N-terminal phosphoryl-transfer domain (EIN) contains the phosphorylation site (H189) and the binding site for the histidine phosphocarrier protein HPr. The C-terminal domain (EIC) is responsible for dimerization and contains the binding site for PEP. The EIN and EIC domains are connected to one another by a long helical linker. Interestingly, the biological activity of the enzyme depends on the synergistic coupling among four intradomain, interdomain, and inter-subunit conformational equilibria modulated by substrate binding.

EI is an excellent system to investigate the implication of oligomerization equilibria in regulation of protein activity. Indeed, only dimeric EI can transfer the phosphoryl group to HPr, and the monomer-dimer equilibrium has been shown to affect several other aspects of the enzyme lifecycle. Despite the observation that the monomer-dimer equilibrium of EI plays a crucial role in regulation of its activity and potentially controls the phosphorylation state of the overall PTS, very little is known about the changes in structure, dynamics, and substrate binding



properties that EI undergoes upon monomerization. Filling this gap would provide an atomic level description of precisely how oligomerization affects the activity of a large and dynamic multidomain protein and inform on potential strategies for allosteric inhibition of EI.

EI is also a promising target for antimicrobial design because (i) it is highly conserved in bacteria but does not have an eukaryotic counterpart,<sup>22</sup> (ii) its phosphorylation state controls multiple cellular processes,<sup>23</sup> (iii) small-molecule inhibitors of EI prevent bacterial growth in rich media,<sup>24-25</sup> (iv) EI deficient bacteria are 10- to 1000-fold less virulent than wild-type strains,<sup>26-27</sup> and (v) experimental screens for virulence factors reported that mutations in EI result in attenuated pathogenesis.<sup>28-29</sup> Therefore, EI inhibitors can potentially function as a new class of antimicrobial compounds that can work synergistically with currently available treatments to address the antibiotic-resistance problem.

In the past, small libraries of 12-mer peptides have been screened against EI and resulted in discovery of a few peptidic inhibitors of the enzyme with IC<sub>50</sub> in the  $\mu$ M range.<sup>30</sup> The actual antimicrobial efficacy of these sequences, however, has not been investigated. More recently, EI has been the target of a virtual screening effort that identified two small molecule that successfully inhibited bacterial growth in rich media.<sup>31</sup> However, the mechanism underlying the antimicrobial activity of the latter molecules remains largely unclear. Despite these promising preliminary results, no experimental screening campaigns have targeted EI with small molecule libraries, probably due to the difficulty of establishing a high throughput assay for detection and quantification of the highly unstable phosphorylated PTS proteins or pyruvate.<sup>32</sup> Since pyruvate is also the product of PEP hydrolysis catalyzed in-vitro by EI, this side-reaction further complicates the development of a pyruvate-based assay to probe the phosphoryl transfer activity of the enzyme. Therefore, there is an urge to design a novel method to quickly detect EI

inhibition by small molecules. Completing this study would also result in development of several small molecules binding to EI with antimicrobial capability and establish the PTS as a novel target for the development of broad-spectrum antimicrobial compounds.

### **Dissertation organization**

This dissertation is organized as follow.

Chapter 1 presents the background information, current progresses on the interested fields and points out the missing information that this research is trying to fill in. The organization of this dissertation is also described.

Chapter 2 is a modified manuscript published in Journal of Biological Chemistry titled “The oligomerization state of bacterial enzyme I (EI) determines EI’s allosteric stimulation or competitive inhibition by  $\alpha$ -ketoglutarate”. This study introduces an NMR-based enzymatic assay to investigate the effect of the small-molecule metabolite  $\alpha$ -ketoglutarate ( $\alpha$ KG) on the kinetics of the EI-catalyzed phosphoryl transfer reaction. It also emphasizes that monomer-dimer equilibrium contributes significantly to the EI activity and must be taken into account to assess the inhibiting or enhancing effects of small molecules toward the enzyme activity.

Chapter 3 is a modified manuscript accepted in Proceedings of the National Academy of Sciences of the United States titled “Structure elucidation of the elusive Enzyme I monomer reveals the molecular dynamic mechanisms linking oligomerization and enzymatic activity”. This study combines molecular engineering and high pressure to disturb the monomer- dimer equilibrium of the dimerization domain of EI (EIC) to study its dissociation from 1 bar to 2.5 kbar in the absence and the presence of small molecules. Backbone residual dipolar couplings collected under high-pressure conditions reveal that the catalytic loops near the dimerization interface become unstructured upon monomerization, preventing the monomeric enzyme from

binding its substrate. This study provides the first atomic-level characterization of EI's monomeric state and highlights the role of the catalytic loops as allosteric connectors controlling both the activity and oligomerization of the enzyme.

Chapter 4 is a modified manuscript published in Journal of Structural Biology titled “An allosteric pocket for inhibition of bacterial Enzyme I identified by NMR-based fragment screening”. This study presents an NMR-based fragment screening protocol to identify novel inhibitors of EI. Three molecular fragments interacting with the enzyme at the same pocket, which is more than 10 Å away from the substrate binding site, inhibit the phosphoryl transfer reaction catalyzed by EI. Proposed inhibiting mechanisms and possible ways to enhance binding affinity of fragments to the EI are also discussed.

Chapter 5 concludes the overall study to highlight some interesting results and propose ideas to move forward.

## CHAPTER 2. THE OLIGOMERIZATION STATE OF BACTERIAL ENZYME I (EI) DETERMINES EI'S ALLOSTERIC STIMULATION OR COMPETITIVE INHIBITION BY $\alpha$ -KETOGLUTARATE

Trang T. Nguyen<sup>1</sup>, Rodolfo Ghirlando<sup>2</sup> and Vincenzo Venditti<sup>1,3</sup>

<sup>1</sup>Department of Chemistry, Iowa State University, Ames, Iowa 50011, USA

<sup>2</sup>Laboratory of Molecular Biology, National Institute of Diabetes and Digestive and Kidney Diseases, National Institutes of Health, Bethesda, Maryland 20892, USA

<sup>3</sup>Roy J. Carver Department of Biochemistry, Biophysics and Molecular Biology, Iowa State University, Ames, Iowa 50011, USA

Modified from a manuscript published in *Journal of Biological Chemistry*

### Abstract

The bacterial phosphotransferase system (PTS) is a signal transduction pathway that couples phosphoryl transfer to active sugar transport across the cell membrane. The PTS is initiated by phosphorylation of enzyme I (EI) by phosphoenolpyruvate (PEP). The phosphorylation state of EI determines the phosphorylation state of all other PTS components, and is thought to play a central role in regulation of several metabolic pathways and to control the biology of bacterial cells at multiple levels, affecting for example virulence and biofilm formation. Here, we describe a novel enzymatic assay, based on fast NMR techniques, to investigate the effect of the small molecule metabolite  $\alpha$ -ketoglutarate ( $\alpha$ KG) on the kinetics of the phosphoryl transfer reaction catalyzed by EI. We show that, at experimental conditions favoring the monomeric form of EI,  $\alpha$ KG acts as an allosteric stimulator of the enzyme. However, when the oligomeric state of EI is shifted toward the dimeric species,  $\alpha$ KG functions as a competitive inhibitor. We develop a kinetic model that fully accounts for the experimental data, and indicates that the observed interplay between allosteric stimulation and competitive

inhibition of EI by  $\alpha$ KG might be used by bacterial cells to respond to physiological fluctuations of the intracellular environment. We expect the mechanism for regulation of EI activity revealed here to be common to several other oligomeric enzymes.

### Introduction

Enzyme I (EI) is the first protein of the bacterial phosphotransferase system (PTS), a signal transduction pathway that results in active sugar transport across the cell membrane (1-3). The PTS is initiated by phosphorylation of EI by the small molecule phosphoenolpyruvate (PEP). Phosphorylated EI transfers the phosphoryl group to the phosphocarrier protein HPr. Thereafter, the phosphoryl group is transferred to a sugar-specific enzyme II (EII), and finally to the incoming sugar (Figure 1a). Recently, the small-molecule metabolite  $\alpha$ -ketoglutarate ( $\alpha$ KG) was shown to act as a competitive inhibitor of EI (inhibition constant,  $K_i$ ,  $\sim 2.2$  mM) (4,5). The intracellular concentration of  $\alpha$ KG varies considerably in response to a change in the availability of nitrogen source in the culturing medium (from 0.5 mM, in the presence of 10 mM  $\text{NH}_4\text{Cl}$ , to 10 mM, in the absence of nitrogen source) (4). Thus, inhibition of EI by  $\alpha$ KG has been proposed as a biochemical mechanism that links the uptake of sugars to the availability of nitrogen source (4,5). In addition to playing a primary role in coupling carbon and nitrogen metabolism in bacteria, the phosphorylation state of EI strictly controls the phosphorylation state of all other PTS components (6), which, in turn, regulates a large number of bacterial functions, including catabolic gene expression, virulence, biofilm formation, chemotaxis, potassium transport, and inducer exclusion, via phosphorylation-dependent protein-protein interactions (2). Therefore, EI is a central regulator of bacterial metabolism, and obtaining a comprehensive understanding of the mechanisms tuning its biological activity may suggest new strategies in bioengineering and antimicrobial design, and might help elucidating the coupling between metabolic networks that controls the biology of all living cells.

EI is a multidomain protein comprising a N-terminal domain (EIN, residues 1-249) that contains the phosphorylation site (His189) and the binding site for HPr, and a C-terminal domain (EIC, residues 261-575) that is responsible for protein dimerization and contains the binding site for PEP and the competitive inhibitor  $\alpha$ KG. The EIN and EIC domains are connected by a short helical linker (residues 250-260) (1,7). EI undergoes a series of large scale conformational rearrangements during its catalytic cycle (Figure 1b), including: (i) a monomer-dimer transition (8), (ii) an expanded-to-compact conformational change within EIC (9), and (iii) an open-to-close transition describing a reorientation of EIN relative to EIC (10-12). PEP binding to EIC shifts the conformational equilibria toward the catalytically competent dimer/compact/close form and activates the enzyme for catalysis (Figure 1b) (11). The monomer-dimer equilibrium of EI has been often suggested as a major regulatory element for PTS since (i) only dimeric EI can be phosphorylated by PEP (13), (ii) the interaction of the enzyme with its physiological ligands  $Mg^{2+}$  and PEP (Michaelis constant,  $K_M$ ,  $\sim 300 \mu M$ ) decreases the equilibrium dissociation constant for dimerization ( $K_D$ ) by more than 10-fold (from  $\sim 5$  to  $<0.1 \mu M$ ) (5,8), and (iii) the intracellular concentrations of EI and PEP were reported to vary substantially depending on the experimental conditions (from  $\sim 30$  to  $\sim 300 \mu M$  for PEP and from  $\sim 1$  to  $\sim 10 \mu M$  for EI) (14-16).

Here, we develop a flexible enzymatic assay to investigate the effect of perturbations of the monomer-dimer equilibrium of *Escherichia coli* EI on the activity of  $\alpha$ KG against the enzyme. We show that, at physiological concentrations of EI and PEP that promote dimerization of EI ( $[EI] > K_D$ ,  $[PEP] > K_M$ ),  $\alpha$ KG acts as a competitive inhibitor of EI. In contrast, at physiological conditions favoring the monomeric form of the enzyme ( $[EI] < K_D$ ,  $[PEP] < K_M$ ),  $\alpha$ KG allosterically stimulates EI autophosphorylation. To the best of our knowledge, this is the first case of a small molecule metabolite being reported to both inhibit and stimulate the activity

of the same enzyme depending on the experimental conditions. The fact that the intracellular concentrations of EI, PEP and  $\alpha$ KG are modulated by the composition of the culturing medium (4,14-16) suggests that this interplay between allosteric stimulation and competitive inhibition of EI might be used by bacterial cells to regulate the phosphorylation state of PTS in response to a change in the extracellular environment.

## Results

*Effect of PEP and  $\alpha$ KG on the monomer-dimer equilibrium of EI* – The effect of the EI ligands, PEP and  $\alpha$ KG, on the monomer-dimer equilibrium of the enzyme was investigated by Analytical Ultracentrifugation (AUC). The sedimentation velocity data indicate that the monomer-dimer equilibrium of EI is shifted toward the monomeric species at concentrations of the enzyme  $< 1 \mu\text{M}$  (Figure 2a), and that addition of PEP or  $\alpha$ KG results in a substantial stabilization of the dimeric state (Figure 2b,c). Our results are consistent with the more than 10-fold decrease in dimerization  $K_D$  reported previously for EI upon addition of PEP or  $\alpha$ KG (5,8).

*Kinetics of the phosphoryl transfer reaction* – Addition of 10 mM PEP to a NMR sample containing 1 mM  $^{15}\text{N}$ -labeled E. coli HPr and  $\sim 0.05 \mu\text{M}$  E. coli EI (unlabeled) results in substantial chemical shift perturbations for the  $^1\text{H}$ - $^{15}\text{N}$  TROSY (Transverse Relaxation Optimized Spectroscopy) (17) peaks originating from HPr residues located in the vicinity of the phosphorylation site (His15, Figure 3a and 3c). As previously noted, HPr does not interact directly with PEP, nor it can be phosphorylated in the absence of EI (18). Therefore, the observed spectral changes are attributed to HPr phosphorylation via EI. After 24 h incubation at  $37^\circ\text{C}$ , the HPr spectrum relaxes back to the unphosphorylated form (Figure 3a), which is consistent with the low thermodynamic stability of phosphorylated histidine residues (19).

Here, we use  $^1\text{H}$ - $^{15}\text{N}$  SOFAST-TROSY spectra(20) to monitor the time evolution of the phosphoryl transfer reaction from PEP to HPr via EI. SOFAST NMR experiments are ideally

suited for real-time investigations on reaction kinetics, because they allow acquisition of 2D NMR spectra within seconds (20). For this particular case,  $\sim 0.05\ \mu\text{M}$  unlabeled EI and 1 mM  $^{15}\text{N}$ -labeled HPr are mixed in 500  $\mu\text{l}$  of reaction buffer (see Experimental procedures) and incubated at  $37^\circ\text{C}$  for 30 minutes in a conventional 5 mm NMR tube. Thereafter, the reaction is started by addition of the desired amount of PEP (note that the PEP stock solution is pre-incubated at  $37^\circ\text{C}$ ). The sample is mixed in the NMR tube and equilibrated at  $37^\circ\text{C}$  for 1 minute in the NMR magnet. The reaction is then monitored for 20 minutes by running a series of 2D  $^1\text{H}$ - $^{15}\text{N}$  SOFAST-TROSY spectra (1 minute each). The phosphoryl transfer reaction is slow on the chemical-shift timescale, and distinct NMR peaks are observed for the phosphorylated and unphosphorylated species (Figure 3b). To monitor the evolution of the phosphoryl transfer reaction, we have used the NMR peak intensities of residues Ala10, Gly13 and Gly54 because they are characterized by high signal-to-noise ratio (S/N) and are well resolved throughout the experiment (Figure 3b). Since the early time points are more important in determining the initial rate of the reaction, we limited our analysis to the disappearance of the unphosphorylated species, for which NMR peaks with high S/N are obtained at the beginning of the phosphoryl transfer reaction (note the phosphorylated HPr peaks are not present at time zero, Figure 3b). Signal intensities are plotted versus time, and the linear portion of the decay is fit to obtain the initial rate of change (Figure 3d). In order to convert the reaction rate from change in signal intensity over time to change in concentration of unphosphorylated HPr over time, the NMR signal intensities at time zero for Ala10, Gly13 and Gly54 were obtained by extrapolation (Figure 3d) and considered to correspond to the expected signal intensity for a 1 mM HPr sample. Unphosphorylated HPr concentration at any time-point is reported as the average over the three analyzed peaks (Figure 3e).



To evaluate the effect of an increased concentration of dimeric EI on the activity of the enzyme, enzyme kinetic data were collected at a fixed concentration of EI ( $\sim 0.05 \mu\text{M}$ ), PEP (1 mM) and HPr (1 mM), and with increasing concentration of the inactive EI mutant His189Gln ( $\text{EI}^{\text{Q}}$ ).  $\text{EI}^{\text{Q}}$  cannot receive the phosphoryl group from PEP, but can still interact with the wild-type protein ( $\text{EI}^{\text{WT}}$ ) to form an active EI dimer (11). As expected, increasing the concentration of  $\text{EI}^{\text{Q}}$  from 0 to 10  $\mu\text{M}$  doubles the HPr phosphorylation rate measured by our NMR assay (Figure 4a). It is worth noticing that  $\text{EI}^{\text{Q}}$  is inactive in the absence of  $\text{EI}^{\text{WT}}$  (Figure 4a). Therefore, the increased enzymatic activity observed by adding  $\text{EI}^{\text{Q}}$  to a sample with a low concentration of  $\text{EI}^{\text{WT}}$  ( $\sim 0.05 \mu\text{M}$ ) is due to an increased population of dimeric EI (which goes from 8% in the absence of  $\text{EI}^{\text{Q}}$ , to 80% in the presence of 10  $\mu\text{M}$   $\text{EI}^{\text{Q}}$ ) and not to the eventual presence of  $\text{EI}^{\text{WT}}$  contaminations in purified  $\text{EI}^{\text{Q}}$ . The dependence of the HPr phosphorylation rate on the total concentration of EI ( $[\text{EI}^{\text{TOT}}] = [\text{EI}^{\text{WT}}] + [\text{EI}^{\text{Q}}]$ ) can be fit considering that (i) only dimeric EI can catalyze the phosphoryl transfer reaction, (ii) binding of PEP to both monomeric subunits results in stabilization of the EI dimer, and (iii) binding of PEP to one monomeric subunit affects the  $K_D$  for EI dimerization to a minor extent. To reduce the number of fitted parameters we have assumed that the dimer  $K_D$  is not affected by binding of a single molecule of PEP to EI (see equations 1-12 in Experimental procedures). The fit was performed in DynaFit 4.0 (21) by keeping  $K_M$  and  $K_D$  for the free enzyme ( $K_{D,\text{free}}$ ) to their measured values (300 and 1  $\mu\text{M}$ , respectively), (5) and by optimizing the dissociation constant for the EI dimer saturated with PEP ( $K_{D,\text{bound}}$ ) and the catalytic rate constant for phosphoryl transfer ( $k_{\text{phosp}}$ ). Results of the fitting are shown in Figure 4a and are consistent with the pronounced stabilization of the EI dimer induced by PEP binding observed by AUC experiments (fitted  $K_{D,\text{bound}} < 10^{-7} \mu\text{M}$ ). A similar kinetic model (equations 13-20 in Experimental procedures) and the same equilibrium constants were

used to fit the dependence of the rate of HPr phosphorylation on the concentration of PEP at a fixed concentration of enzyme ( $\sim 0.05 \mu\text{M}$ , Figure 4b). It is worth noticing that increasing the concentration of PEP beyond 1 mM makes the phosphoryl transfer reaction too fast to be monitored by our method at our experimental conditions ( $37^\circ\text{C}$  and  $\sim 0.05 \mu\text{M}$  enzyme). Therefore,  $k_{phosp}$  cannot be accurately determined by the available data. However, our fitted results ( $k_{phosp} > 10,000 \text{ s}^{-1}$ ) are in good agreement with the fast conversion rates previously reported for the EI autophosphorylation reaction (22).

*Effect of  $\alpha\text{KG}$  on the activity of EI* – Data reported in the previous sections indicate that dimerization stimulates the phosphoryl transfer activity of EI (Figure 4a), and that increasing the concentration of  $\alpha\text{KG}$  from 0 to 20 mM shifts the monomer-dimer equilibrium toward the enzymatically active EI dimer (Figure 2). In this section, we evaluate the effect of  $\alpha\text{KG}$  on the phosphoryl transfer activity of EI at experimental conditions that promote the monomeric or dimeric form of the enzyme.

At low concentration of enzyme ( $< K_{D,free}$ ) and substrate ( $< K_M$ ), we expect EI to exist predominantly as a monomer. In this case, addition of small concentrations of  $\alpha\text{KG}$  ( $< K_I$ ) will act synergistically with PEP in saturating the binding sites on EI (Figure 5a). The increased population of EI-ligand adducts will result in stabilization of the enzymatically active EI dimer and allosteric stimulation of the phosphoryl transfer reaction (Figure 5a). In contrast, increasing the concentration of  $\alpha\text{KG}$  to values larger than  $K_I$  will result in oversaturation of the binding sites on EI, and consequential competitive inhibition of enzymatic activity (Figure 5a). Indeed, enzyme kinetic data collected at  $\sim 0.05 \mu\text{M}$  EI,  $200 \mu\text{M}$  PEP and increasing concentrations of  $\alpha\text{KG}$  (0-10 mM) show an initial stimulation of enzymatic activity followed by a decrease in the rate of phosphoryl transfer at high concentration of  $\alpha\text{KG}$  ( $> 2 \text{ mM}$ , Figure 6a). At concentrations

of  $EI > K_{D,free}$  and/or concentrations of  $PEP > K_M$ , we expect EI to exist predominantly as a dimer, and  $\alpha KG$  to act exclusively as an inhibitor of the enzyme (Figure 5b-d). Experimental data collected at  $\sim 0.05 \mu M$  EI and  $1000 \mu M$  PEP (Figure 6b),  $10 \mu M$  EI and  $200 \mu M$  PEP (Figure 6c), and  $10 \mu M$  EI and  $1000 \mu M$  PEP (Figure 6d) confirm the expected behavior. Interestingly all kinetic data reported in Figure 6 can be fit considering that (i) only dimeric EI can catalyze the phosphoryl transfer reaction, (ii) saturation of the EI dimer binding sites with PEP and/or  $\alpha KG$  (dissociation constants  $K_M$  and  $K_I$ , respectively) decreases the  $K_D$  for EI dimerization, and (iii) binding of PEP or  $\alpha KG$  to one monomeric subunit affects the  $K_D$  for EI dimerization to a minor extent. As done in the previous section when fitting the dependence of the phosphoryl transfer reaction on the concentration of enzyme, the model has been simplified by setting the dissociation constant of the EI dimer occupied by a single ligand molecule to  $K_{D,free}$  (see equations 21-37 in Experimental procedures). Fits were performed by keeping  $K_M$ ,  $K_I$  and  $K_{D,free}$  to their measured values ( $300$ ,  $2200$  and  $1 \mu M$ , respectively) (5), and optimizing values for  $K_{D,bound}$  and  $k_{phosp}$ . In all cases a  $K_{D,bound} < 10^{-7} \mu M$  was obtained.

The kinetic model summarized by equations 21-37 was used to simulate the effect of physiological fluctuations in the intracellular environment on the activity of  $\alpha KG$  against EI (Figure 7). In this simulation,  $K_m$  and  $K_I$  were set to the literature values for the EI-PEP and EI- $\alpha KG$  interactions (5), respectively.  $K_{D,bound}$  was set to  $10^{-7} \mu M$ , the upper bound value obtained by fitting the enzyme kinetic data in Figures 4 and 6 (this work). The intracellular concentrations of EI, PEP and  $\alpha KG$  were considered to vary in the  $0.5$ - $10 \mu M$  (16),  $30$ - $300 \mu M$  (14,15) and  $0$ - $10$  mM (4) range, respectively.  $K_{D,free}$  is strongly affected by the presence of divalent cations in the buffer (8). Therefore,  $K_{D,free}$  was set to  $5$  or  $1 \mu M$  (8) to simulate low ( $0.1$  mM) or high ( $4$  mM) intracellular concentration of free  $Mg^{2+}$ , respectively. Our simulation (Figure 7) suggests that

$\alpha$ KG binding can provide up to 1.5 times stimulation of EI activity at physiological conditions that promote the monomeric form of the enzyme (low concentrations of EI, PEP and  $\text{Mg}^{2+}$ ), but results in strong inhibition of enzymatic activity at physiological concentrations of EI, PEP and  $\text{Mg}^{2+}$  that stabilize the EI dimer.

## Discussion

Cellular metabolism is the result of a large number of metabolic reactions involving the conversion of the carbon source (usually glucose) into the building blocks needed for macromolecular biosynthesis. Within cells, these reactions form metabolic networks that are interconnected and tightly regulated in order to allow the organism to quickly respond to changes in the external environment.

The PTS is a central regulator of bacterial metabolism and controls important cellular functions, such as sugar uptake, virulence, biofilm formation and chemotaxis (1-3). The PTS-mediated regulatory mechanisms are based either on direct phosphorylation of the target protein by one of the PTS components, or on phosphorylation-dependent interactions (2). As such, the regulatory functions of PTS can be finely tuned by careful modulation of the EI autophosphorylation reaction (Figure 1a).

Here, we have developed a novel method based on fast NMR techniques to assay the activity of EI under a wide range of experimental conditions. Our data indicate that the small molecule metabolite  $\alpha$ KG can act either as an allosteric stimulator or as a competitive inhibitor of EI depending on the oligomeric state of the enzyme (Figures 5 and 6). Indeed, at experimental conditions favoring the dimeric form of EI,  $\alpha$ KG inhibits the phosphoryl transfer activity of the enzyme (Figure 6b-d). In contrast, at experimental conditions favoring monomeric EI, addition of  $\alpha$ KG results in a shift of the monomer-dimer equilibrium toward the enzymatically active dimeric form and a consequential stimulation of enzymatic activity (Figure 6a). Interestingly, the

intracellular concentration of EI was measured to be close to the equilibrium dissociation constant for protein dimerization (16), and the dimer  $K_D$  of the free enzyme was shown to be affected substantially by varying the concentration of  $Mg^{2+}$  in the experimental buffer (from 5 to 1  $\mu$ M moving from 0 to 4 mM  $Mg^{2+}$ ) (8). In addition, the intracellular amount of PEP and  $\alpha$ KG are close to the dissociation constants for PEP and  $\alpha$ KG binding to the enzyme, respectively (4,14,15). In this scenario, small fluctuations in the intracellular concentrations of EI,  $Mg^{2+}$ , PEP and  $\alpha$ KG induced by a change in the extracellular environment would drastically affect the activity of  $\alpha$ KG on the PTS (Figure 7). The PTS was shown to play multiple regulatory function in bacterial metabolism (1-3). Thus, the interplay between allosteric stimulation and competitive inhibition of EI by  $\alpha$ KG revealed here may be required to promptly adjust the phosphorylation state of PTS in response to a change in the extracellular environment. Finally, this work shows how the activity of small molecule metabolites against their biological targets can change significantly in response to small changes in experimental conditions, and illustrates that the dependence of the oligomeric state of the enzyme on the experimental conditions must be considered with great care when interpreting enzyme kinetic data.

### **Materials and Methods**

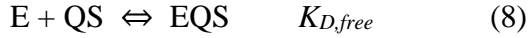
*Protein expression and purification* – Uniformly  $^{15}N$ -labeled E. coli HPr was expressed and purified as previously described (23). The His189Gln ( $EI^Q$ ) mutant of E. coli EI was created using the QuikChange Site-Directed Mutagenesis Kit (Stratagene). Genes for EI and  $EI^Q$  were cloned into a pET-15b vector (Novagen) incorporating a N-terminal His-tag. The plasmid was introduced into E. coli strain BL21star (DE3) (Invitrogen) and the transformed bacteria were plated onto an LB-agar plate containing ampicillin (100  $\mu$ g/ml) for selection. Cell were grown at 37°C in Luria Bertani (LB) medium. At  $A_{600} \sim 0.4$  the temperature was reduced to 20°C and expression was induced with 1 mM isopropyl-D-thiogalactopyranoside (IPTG). Cells were

harvested by centrifugation (4,000g for 30 min) after 16 h of induction and the pellet was resuspended in 20 ml of 20 mM Tris, pH 8.0 (buffer A). The suspension was lysed using a microfluidizer and centrifuged at 40,000g for 40 min. The supernatant was filtrated through a 0.45  $\mu$ m filter membrane to remove cell debris and applied to a His affinity column (GE Healthcare). After the sample was loaded, the column was washed with buffer B (buffer A containing 20 mM imidazole), and the target protein was eluted with buffer C (buffer A containing 300 mM imidazole). The fractions containing the protein were confirmed by SDS-polyacrylamide gel electrophoresis and farther purified by gel filtration on a Superdex-200 column (GE Healthcare) equilibrated with 20 mM Tris, pH 7.4, 200 mM NaCl, 2 mM dithiothreitol (DTT), and 1 mM ethylenediaminetetraacetic acid (EDTA). Relevant fractions were loaded on an EnrichQ anion exchange column (Biorad), and the protein was eluted with a 400 ml gradient from 150 mM to 400 mM NaCl.

*Analytical ultracentrifugation* – Sedimentation velocity experiments were carried out on a Beckman Coulter ProteomeLab XL-I analytical ultracentrifuge at 50 krpm and 20°C following standard protocols (24). A 2.0 mM stock solution of EI was diluted 50-fold in 100 mM NaCl, 20 mM Tris buffer, pH 7.4, 2 mM DTT and 1 mM EDTA (buffer A), and used to prepare a series of solutions ranging from approximately 1 to 40  $\mu$ M by serial dilution. Samples were loaded into 2 channel epon centerpiece cells (12 or 3 mm path length depending on the concentration). Absorbance (280 nm) and Rayleigh interference (655 nm) scans were collected, time-corrected (25), and analyzed in SEDFIT 15.01c (26) in terms a continuous c(s) distribution covering an s range of 0.0 – 10.0 S with a resolution of 200 and a maximum entropy regularization confidence level of 0.68. Good fits were obtained with r.m.s.d. values corresponding to typical instrumental noise values. Identical experiments were carried out in buffer A containing 20 mM PEP (buffer

B) or 20 mM  $\alpha$ KG (buffer C). Weighted-average sedimentation coefficients obtained by integration of the  $c(s)$  distributions for EI in buffer A were used to create an isotherm that was analyzed in SEDDPHAT 13.0a in terms of a reversible monomer-dimer equilibrium to obtain a  $K_d$  of 1  $\mu$ M, which is consistent with previous investigations of the EI monomer-dimer equilibrium.(5,8) The solution density ( $\rho$ ) and viscosity ( $\eta$ ) for buffer A were calculated based on the solvent composition using SEDNTERP (27). Solution densities for buffers B and C were measured at 20°C on an Anton-Paar DMA 5000 density meter; solution viscosities were measured at 20°C using an Anton Paar AMV rolling ball viscometer. The partial specific volume ( $v$ ) and absorption extinction coefficient for EI were calculated in SEDNTERP (27) based on the amino acid composition. The corresponding interference signal increment (28) was calculated in SEDFIT15.01c (26).

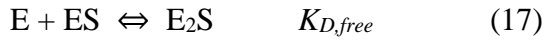
*Enzyme kinetic assay* – The ability of EI to transfer the phosphoryl group from PEP to HPr was assayed at 37°C using fast NMR methods (20) as described in Results. NMR spectra were recorded on a Bruker 700 MHz spectrometer equipped with a z-shielded gradient triple resonance cryoprobe. Spectra were processed using NMRPipe (29) and analyzed using the program SPARKY (<http://www.cgl.ucsf.edu/home/sparky>). The  $^1\text{H}$ - $^{15}\text{N}$  correlation spectrum of unphosphorylated HPr was assigned according to previously reported chemical shift tables (30). Composition of the reaction buffer was as follow: 20 mM Tris, pH 7.4, 100 mM NaCl, 4 mM  $\text{MgCl}_2$ , 2 mM DTT, 1 mM EDTA, and 95%  $\text{H}_2\text{O}$ /5%  $\text{D}_2\text{O}$  (v/v). Unless stated otherwise, all enzymatic assays were run in a reaction volume of 500  $\mu$ l and at fixed concentrations wild-type EI ( $\sim 0.05$   $\mu$ M) and HPr (1 mM). Assays were run in triplicate. Initial velocities for the phosphoryl transfer reaction in the presence of different amount of EI<sup>Q</sup> (see Results and Discussion) were fit in DynaFit 4.0 (21) using the following kinetic model:



where E is the wild-type enzyme ( $EI^{WT}$ ), Q is the concentration of  $EI^Q$ , S is the substrate (PEP), ES is the  $EI^{WT}$ -PEP complex, QS is the  $EIQ$ -PEP complex, EQ is the mixed  $EI^{WT}E^Q$  dimer, EQS is the mixed dimer with PEP bound to the  $EI^Q$  subunit, ESQ is the mixed dimer with PEP bound to the  $EI^{WT}$  subunit, ESQS is the mixed dimer with two PEP molecules, P is the product,  $K_{D,free}$  (1  $\mu$ M) is the dimer dissociation constant for free EI,  $K_{D,bound}$  (fitted) is the dimer dissociation constant for EI when saturated with ligands,  $K_M$  (300  $\mu$ M) is the Michaelis constant for the EI-PEP interaction,  $k_{phosp}$  (fitted) is the rate constant for the phosphoryl transfer interaction,  $\rightleftharpoons$  indicates a thermodynamic equilibrium, and  $\Rightarrow$  indicates the unidirectional chemical step. Note that given the small amount of  $EI^{WT}$  compared to  $EI^Q$ , the amount of  $EI^{WT}EI^{WT}$  dimer is considered to be negligible in this model.

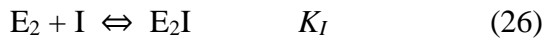


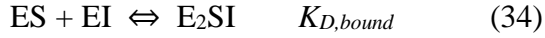
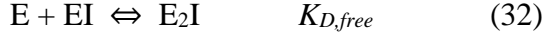
Initial velocities for the phosphoryl transfer reaction in the presence of different amount of PEP (see Results and Discussion) were fit in DynaFit 4.0 (21) using the following kinetic model:



where  $E_2$  is the  $EI^{WT}EI^{WT}$  dimer,  $E_2S$  is the EI dimer complexed to one molecule of PEP and  $E_2S_2$  is the dimer complexed with two molecules of PEP.

Enzyme kinetic data measured at different concentration of  $\alpha$ KG were fit in DynaFit 4.0 (21) using the following kinetic model:





where I is the inhibitor ( $\alpha$ KG), EI is the EI- $\alpha$ KG complex,  $E_2I$  is the EI dimer complexed with one  $\alpha$ KG molecule,  $E_2I_2$  is the EI dimer complexed with two  $\alpha$ KG molecules,  $E_2SI$  is the EI dimer complexed with one  $\alpha$ KG molecule and one PEP molecule, and  $K_I$  (2.2 mM) is the dissociation constant for free EI- $\alpha$ KG interaction. In the fits, the concentration of EI is considered to be the sum of the active ( $EI^{WT}$ ) and inactive ( $EI^Q$ ) species.

### Acknowledgments

We thank Dr. Scott Nelson for helpful discussions. This work was supported by funds from the Roy J. Carver Charitable Trust and Iowa State University (to V.V.), and by the Intramural Research Program of the NIH, the National Institute of Diabetes and Digestive and Kidney Diseases (NIDDK) (to R.G.).

Conflict of interest: The authors declare that they have no conflicts of interest with the contents of this article.

## References

1. Clore, G. M., and Venditti, V. (2013) Structure, dynamics and biophysics of the cytoplasmic protein-protein complexes of the bacterial phosphoenolpyruvate: sugar phosphotransferase system. *Trends Biochem Sci* 38, 515-530
2. Deutscher, J., Ake, F. M., Derkaoui, M., Zebre, A. C., Cao, T. N., Bouraoui, H., Kentache, T., Mokhtari, A., Milohanic, E., and Joyet, P. (2014) The bacterial phosphoenolpyruvate:carbohydrate phosphotransferase system: regulation by protein phosphorylation and phosphorylation-dependent protein-protein interactions. *Microbiol Mol Biol Rev* 78, 231-256
3. Postma, P. W., Lengeler, J. W., and Jacobson, G. R. (1996) Phosphoenolpyruvate:Carbohydrate Phosphotransferase Systems. in *Escherichia coli and Salmonella: Cellular and Molecular Biology* (Neidhardt, F. C., Lin, E. C., and Curtiss, R. eds.). pp 1149-1174
4. Doucette, C. D., Schwab, D. J., Wingreen, N. S., and Rabinowitz, J. D. (2011) alpha-Ketoglutarate coordinates carbon and nitrogen utilization via enzyme I inhibition. *Nat Chem Biol* 7, 894-901
5. Venditti, V., Ghirlando, R., and Clore, G. M. (2013) Structural basis for enzyme I inhibition by alpha-ketoglutarate. *ACS Chem Biol* 8, 1232-1240
6. Hogema, B. M., Arents, J. C., Bader, R., Eijkemans, K., Yoshida, H., Takahashi, H., Aiba, H., and Postma, P. W. (1998) Inducer exclusion in *Escherichia coli* by non-PTS substrates: the role of the PEP to pyruvate ratio in determining the phosphorylation state of enzyme IIAGlc. *Mol Microbiol* 30, 487-498
7. Chauvin, F., Brand, L., and Roseman, S. (1996) Enzyme I: the first protein and potential regulator of the bacterial phosphoenolpyruvate: glycolate phosphotransferase system. *Res Microbiol* 147, 471-479
8. Patel, H. V., Vyas, K. A., Savtchenko, R., and Roseman, S. (2006) The monomer/dimer transition of enzyme I of the *Escherichia coli* phosphotransferase system. *J Biol Chem* 281, 17570-17578
9. Venditti, V., and Clore, G. M. (2012) Conformational selection and substrate binding regulate the monomer/dimer equilibrium of the C-terminal domain of *Escherichia coli* enzyme I. *J Biol Chem* 287, 26989-26998
10. Teplyakov, A., Lim, K., Zhu, P. P., Kapadia, G., Chen, C. C., Schwartz, J., Howard, A., Reddy, P. T., Peterkofsky, A., and Herzberg, O. (2006) Structure of phosphorylated enzyme I, the phosphoenolpyruvate:sugar phosphotransferase system sugar translocation signal protein. *Proceedings of the National Academy of Sciences of the United States of America* 103, 16218-16223

11. Venditti, V., Tugarinov, V., Schwieters, C. D., Grishaev, A., and Clore, G. M. (2015) Large interdomain rearrangement triggered by suppression of micro- to millisecond dynamics in bacterial Enzyme I. *Nat Commun* 6, 5960
12. Venditti, V., Schwieters, C. D., Grishaev, A., and Clore, G. M. (2015) Dynamic equilibrium between closed and partially closed states of the bacterial Enzyme I unveiled by solution NMR and X-ray scattering. *Proc Natl Acad Sci U S A* 112, 11565-11570
13. Seok, Y. J., Zhu, P. P., Koo, B. M., and Peterkofsky, A. (1998) Autophosphorylation of enzyme I of the *Escherichia coli* phosphoenolpyruvate:sugar phosphotransferase system requires dimerization. *Biochem Biophys Res Commun* 250, 381-384
14. Albe, K. R., Butler, M. H., and Wright, B. E. (1990) Cellular concentrations of enzymes and their substrates. *J Theor Biol* 143, 163-195
15. Lagunas, R., and Gancedo, C. (1983) Role of phosphate in the regulation of the Pasteur effect in *Saccharomyces cerevisiae*. *Eur J Biochem* 137, 479-483
16. Mattoo, R. L., and Waygood, E. B. (1983) Determination of the levels of HPr and enzyme I of the phosphoenolpyruvate-sugar phosphotransferase system in *Escherichia coli* and *Salmonella typhimurium*. *Can J Biochem Cell Biol* 61, 29-37
17. Pervushin, K., Riek, R., Wider, G., and Wuthrich, K. (1997) Attenuated T2 relaxation by mutual cancellation of dipole-dipole coupling and chemical shift anisotropy indicates an avenue to NMR structures of very large biological macromolecules in solution. *Proc Natl Acad Sci U S A* 94, 12366-12371
18. Weigel, N., Powers, D. A., and Roseman, S. (1982) Sugar transport by the bacterial phosphotransferase system. Primary structure and active site of a general phosphocarrier protein (HPr) from *Salmonella typhimurium*. *J Biol Chem* 257, 14499-14509
19. Klumpp, S., and Krieglstein, J. (2002) Phosphorylation and dephosphorylation of histidine residues in proteins. *Eur J Biochem* 269, 1067-1071
20. Schanda, P., Kupce, E., and Brutscher, B. (2005) SOFAST-HMQC experiments for recording two-dimensional heteronuclear correlation spectra of proteins within a few seconds. *J Biomol NMR* 33, 199-211
21. Kuzmic, P. (2009) DynaFit--a software package for enzymology. *Methods Enzymol* 467, 247-280
22. Meadow, N. D., Mattoo, R. L., Savtchenko, R. S., and Roseman, S. (2005) Transient state kinetics of Enzyme I of the phosphoenolpyruvate:glycose phosphotransferase system of *Escherichia coli*: equilibrium and second-order rate constants for the phosphotransfer reactions with phosphoenolpyruvate and HPr. *Biochemistry* 44, 12790-12796

23. Suh, J. Y., Cai, M., and Clore, G. M. (2008) Impact of phosphorylation on structure and thermodynamics of the interaction between the N-terminal domain of enzyme I and the histidine phosphocarrier protein of the bacterial phosphotransferase system. *J Biol Chem* 283, 18980-18989
24. Zhao, H., Brautigam, C. A., Ghirlando, R., and Schuck, P. (2013) Overview of current methods in sedimentation velocity and sedimentation equilibrium analytical ultracentrifugation. *Curr Protoc Protein Sci Chapter 20, Unit20 12*
25. Ghirlando, R., Balbo, A., Piszczek, G., Brown, P. H., Lewis, M. S., Brautigam, C. A., Schuck, P., and Zhao, H. (2013) Improving the thermal, radial, and temporal accuracy of the analytical ultracentrifuge through external references. *Anal Biochem* 440, 81-95
26. Schuck, P. (2000) Size-distribution analysis of macromolecules by sedimentation velocity ultracentrifugation and lamm equation modeling. *Biophysical journal* 78, 1606-1619
27. Cole, J. L., Lary, J. W., T, P. M., and Laue, T. M. (2008) Analytical ultracentrifugation: sedimentation velocity and sedimentation equilibrium. *Methods in cell biology* 84, 143-179
28. Zhao, H., Brown, P. H., and Schuck, P. (2011) On the distribution of protein refractive index increments. *Biophys J* 100, 2309-2317
29. Delaglio, F., Grzesiek, S., Vuister, G. W., Zhu, G., Pfeifer, J., and Bax, A. (1995) NMRPipe: a multidimensional spectral processing system based on UNIX pipes. *J Biomol NMR* 6, 277-293
30. Garrett, D. S., Seok, Y. J., Peterkofsky, A., Gronenborn, A. M., and Clore, G. M. (1999) Solution structure of the 40,000 Mr phosphoryl transfer complex between the N-terminal domain of enzyme I and HPr. *Nat Struct Biol* 6, 166-173

## Figures

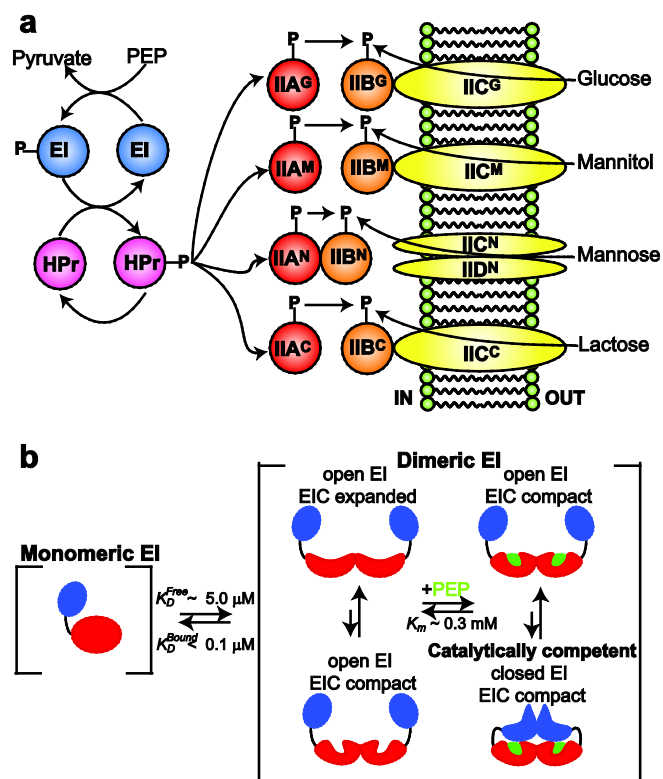


**Figure 1. The bacterial PTS. (a) Diagram of the *E. coli* PTS. The first two steps are common to all branches of the pathway. Thereafter, the pathway splits into four sugar-specific classes: glucose, mannitol, mannose, and lactose/chitobiose. Color code for the enzymes in the pathway is as follow: EI, blue; HPr, pink; EIIA, red; EIIB, orange; EIIC/EIID, yellow. EIIC/EIID enzymes are shown in a lipid bilayer. The phosphorylated site is indicated by –P. (b) Schematic summary of the conformational equilibria of EI during its catalytic cycle. The EIN domain is colored blue, the EIC domain is colored red and PEP is colored green. Equilibrium constants reported in previous research articles (5,8) are shown.**

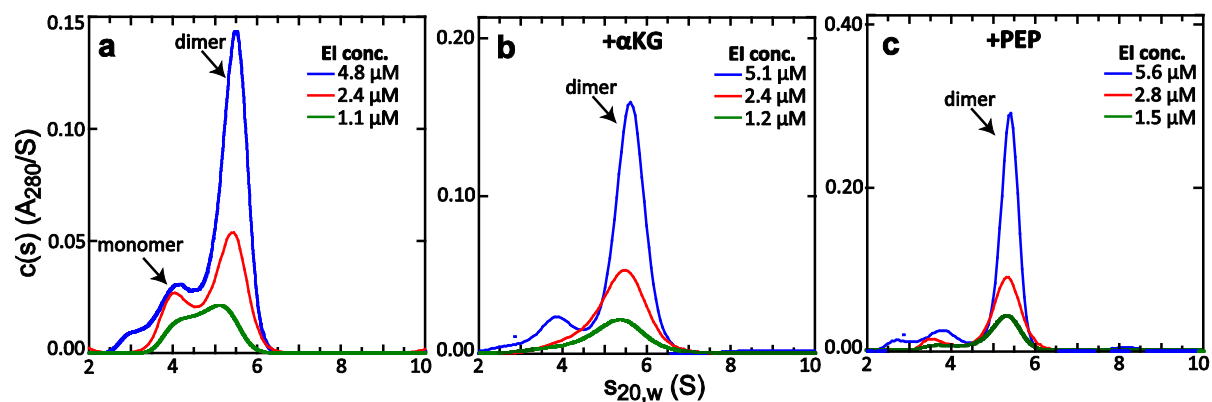


**Figure 2. PEP and  $\alpha$ KG shift the monomer-dimer equilibrium of EI.**  $c(s)$  distributions for EI obtained at different loading concentrations (ranging from  $\sim 5$  to  $\sim 1$   $\mu$ M) based on sedimentation velocity absorbance data collected at 50 krpm and 20.0°C (see Experimental procedures). Data acquired for the free EI (a) revealed concentration dependent  $c(s)$  absorbance profiles typical of a monomer-dimer equilibrium. In the presence of 20 mM  $\alpha$ KG (b) and 20 mM PEP (c) the sedimentation experiments indicate that EI is dimeric within the tested concentration range.

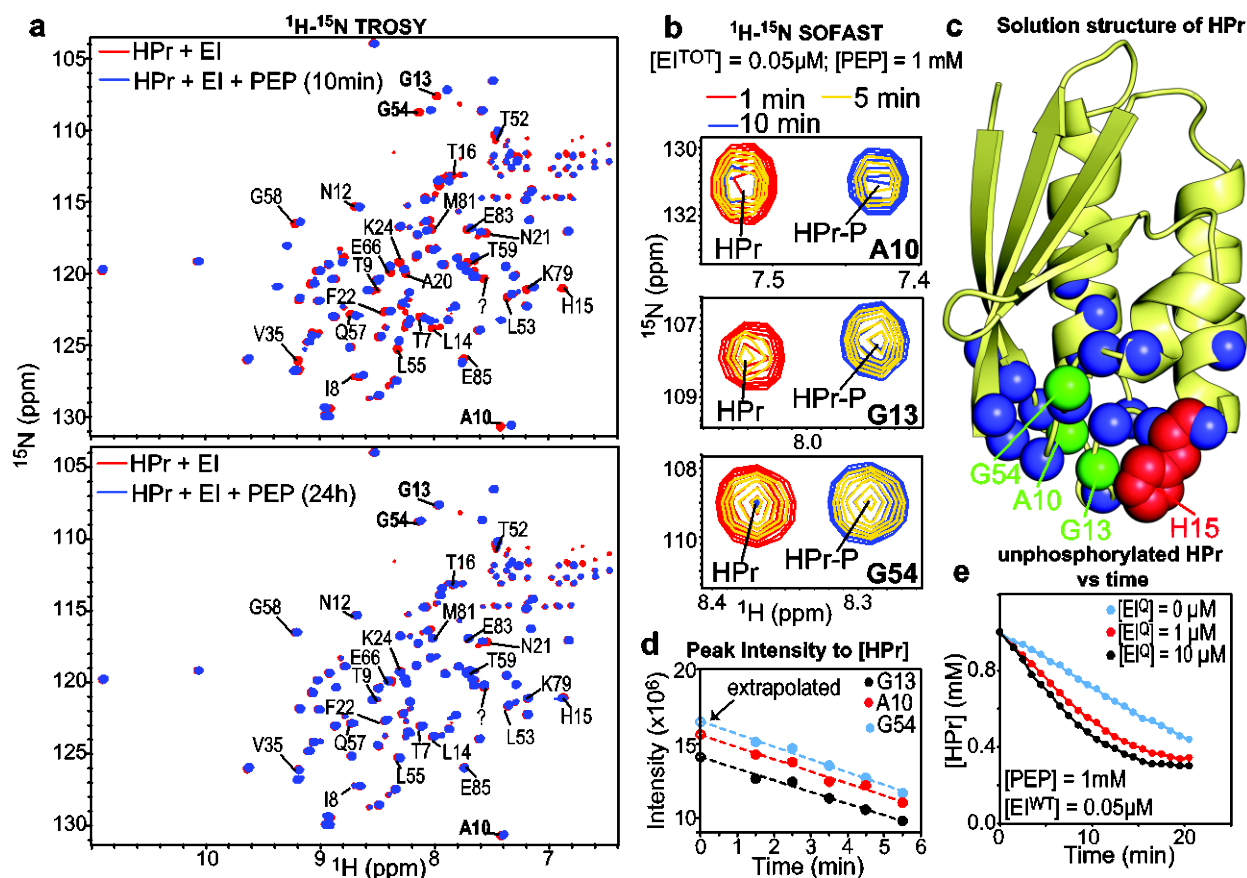


**Figure 3. Activity assay for the phosphoryl transfer reaction.** (a)  $^1\text{H}$ - $^{15}\text{N}$  TROSY spectrum of  $^{15}\text{N}$ -labeled HPr in the presence of 0.05  $\mu\text{M}$  unlabeled EI in the absence (red) and in the presence (blue) of 10 mM PEP. Spectra in the presence of PEP were measured after incubation for 10 minutes (upper panel) or 24 hours (lower panel) at 37°C. Cross-peaks showing chemical shift perturbation upon addition of PEP are labeled. The question mark indicates a peak of unknown assignment. (b) Close-up views of a  $^1\text{H}$ - $^{15}\text{N}$  SOFAST-TROSY spectrum of 1 mM HPr in the presence of 0.05  $\mu\text{M}$  EI and 1 mM PEP showing the cross-peaks for residues Ala10, Gly13 and Gly54 at three different time points during the activity assay: 1 minute, red; 5 minutes, yellow; 10 minutes, blue. For each residue, distinct peaks are observed for the unphosphorylated and phosphorylated HPr species (labeled HPr and HPr-P in the figure, respectively). (c) 3D structure of HPr. Backbone amide groups experiencing chemical shift perturbation upon addition of PEP



to a sample containing HPr and EI are shown as spheres. Amide groups for Ala10, Gly13 and Gly54 are colored green. The phosphorylation site (His15) is shown as red spheres. (d) Intensities of the  $^1\text{H}$ - $^{15}\text{N}$  SOFAST-TROSY cross-peaks of Ala10 (red), Gly13 (black) and Gly54 (blue) are plotted versus time. Intensities at time 0 were obtained by extrapolation. The displayed data were measured on a 1 mM sample of HPr containing 0.05  $\mu\text{M}$  EI<sup>WT</sup> and 1 mM PEP. The extrapolated intensities at time 0 (corresponding to 1 mM HPr) were used to calculate the time-dependence of the unphosphorylated HPr concentration. (d) The concentration of unphosphorylated HPr is plotted versus time. The displayed data were measured on a 1 mM sample of HPr containing 0.05  $\mu\text{M}$  EI<sup>WT</sup>, and 1 mM PEP. Concentrations of EI<sup>Q</sup> were 0 (blue), 1 (red) and 10  $\mu\text{M}$  (black).

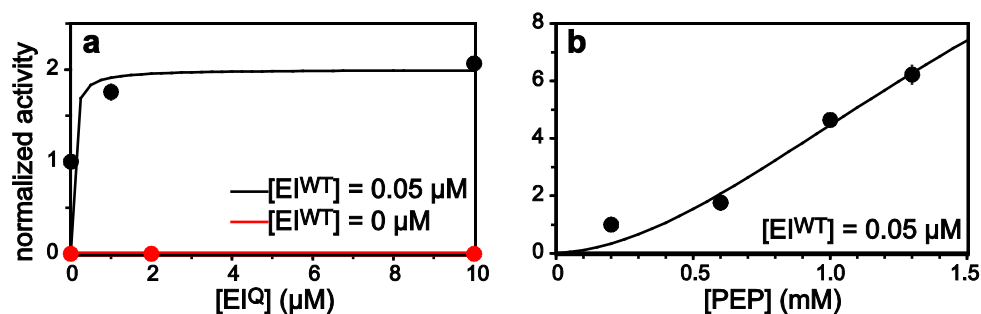


**Figure 4. Dependence of the phosphoryl transfer reaction on the concentration of substrate and enzyme.** (a) The phosphoryl transfer activity of EI is plotted versus the concentration of an inactive mutant of the enzyme (EI<sup>Q</sup>) in the presence of 0 (red) or 0.05  $\mu\text{M}$  wild-type EI (EI<sup>WT</sup>). Data were fit using the kinetic model summarized by equations 1-12 (Experimental procedures). Results of the fits are shown as solid lines. (b) The phosphoryl transfer activity of EI is plotted versus the concentration of PEP. Data were fit using the kinetic model summarized by equations 13-20 (Experimental procedures). Results of the fits are shown as solid lines.

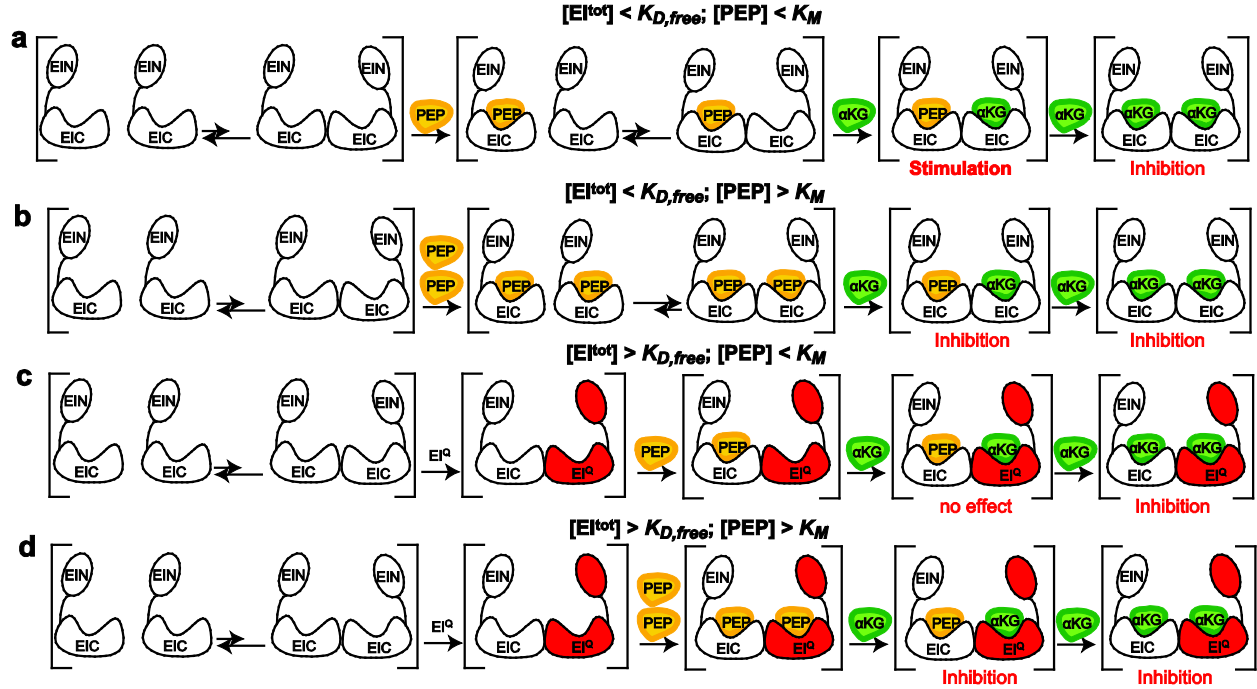


**Figure 5. The monomer-dimer equilibrium of EI regulates the activity of  $\alpha$ KG on the enzyme.** (a) At low concentration of enzyme ( $< K_{D,free}$ ) and PEP ( $< K_M$ ) addition of  $\alpha$ KG stabilizes the catalytically active EI dimer and stimulates the activity of the enzyme. Increasing the concentration of  $\alpha$ KG to values higher than  $K_I$  results in displacement of PEP from the active site and inhibition of EI. (b) At high concentration of PEP ( $> K_M$ ) addition of  $\alpha$ KG does not affect the population of dimeric EI (which is already stabilized by PEP binding to both subunits) and results in inhibition of the enzyme. At EI concentration larger than  $K_{D,free}$  the monomer dimer equilibrium is already shifted toward the dimer form, and no stimulatory effect of  $\alpha$ KG is detected at low (c) or high (d) concentration of PEP. The total concentration of enzyme ( $EI^{TOT}$ ) is the sum of the concentrations of the wild-type EI ( $EI^{WT}$ ) and of an inactive EI mutant ( $EI^Q$ , see Results). PEP and  $\alpha$ KG are colored yellow and green, respectively.  $EI^{WT}$  and  $EI^Q$  are colored white and red, respectively.

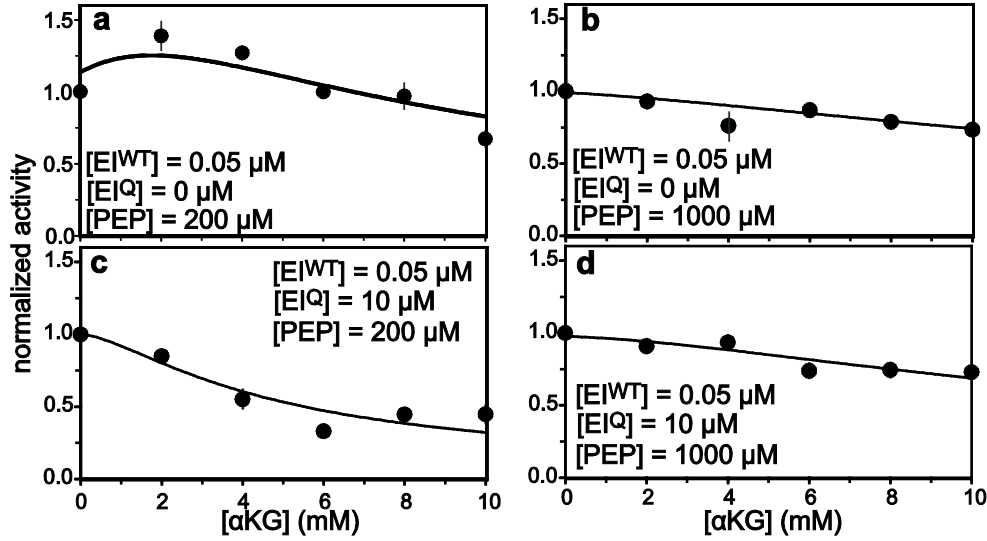


**Figure 6. Dependence of the phosphoryl transfer reaction on the concentration of  $\alpha$ KG.**

Enzyme kinetic data were measured at a fixed concentration of  $EI^{WT}$  ( $\sim 0.05 \mu M$ ).  $EI^Q$  and PEP concentrations were as follow: (a)  $0 \mu M$   $EI^Q$  and  $200 \mu M$  PEP; (b)  $0 \mu M$   $EI^Q$  and  $1000 \mu M$  PEP; (c)  $10 \mu M$   $EI^Q$  and  $200 \mu M$  PEP; (d)  $10 \mu M$   $EI^Q$  and  $1000 \mu M$  PEP. Data in (a)-(d) were fit using the kinetic model summarized by equations 11-37 (Experimental procedures). Results of the fits are shown as solid lines.

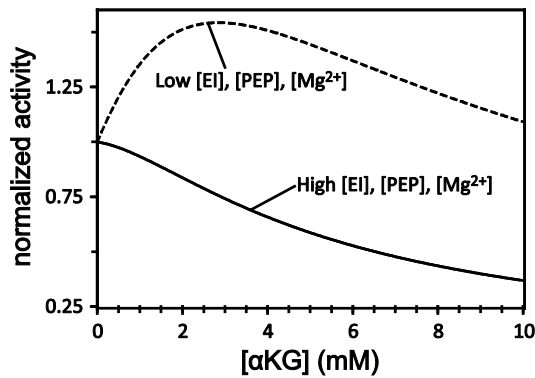


**Figure 7. Effect of physiological fluctuations of the intracellular environment on the activity of  $\alpha$ KG against EI.** The rate of the phosphoryl transfer reaction is simulated in DynaFit 4.0 (21) using the kinetic model summarized by equations 18-32.  $K_M$ ,  $K_I$  and  $K_{D, bound}$  were set to  $300 \mu M$  (5),  $2200 \mu M$  (5) and  $10^{-7} \mu M$  (this work), respectively. The concentration of EI was

set to 0.5  $\mu\text{M}$  (dashed line) or 10  $\mu\text{M}$  (solid line) (16). PEP concentration was 30  $\mu\text{M}$  (dashed line) or 300  $\mu\text{M}$  (solid line) (14,15). The value of  $K_{D,\text{free}}$  depends on the concentration of  $\text{Mg}^{2+}$ . Here, a  $K_{D,\text{free}}$  of 5  $\mu\text{M}$  (dashed line) or 1  $\mu\text{M}$  (solid line) was used to simulate an intracellular environment poor ( $\sim 0.1 \text{ mM}$ ) or rich ( $\sim 4 \text{ mM}$ ) of  $\text{Mg}^{2+}$ , respectively (8).

### CHAPTER 3. STRUCTURE ELUCIDATION OF THE ELUSIVE ENZYME I MONOMER REVEALS THE MOLECULAR MECHANISMS LINKING OLIGOMERIZATION AND ENZYMATIC ACTIVITY

Trang T. Nguyen<sup>1</sup>, Rodolfo Ghirlando<sup>2</sup>, Julien Roche<sup>3\*</sup>, and Vincenzo Venditti<sup>1,3\*</sup>

<sup>1</sup>Department of Chemistry, Iowa State University, Ames, IA 50011, USA

<sup>2</sup>Laboratory of Molecular Biology, NIDDK, National Institutes of Health, Bethesda, Maryland  
20892

<sup>3</sup>Roy J. Carver Department of Biochemistry, Biophysics and Molecular Biology, Iowa State  
University, Ames, IA 50011, USA

Modified from a manuscript accepted in *Proceedings of the National Academy of Sciences of the  
United States of America*

#### **Abstract**

Enzyme I (EI) is a phosphotransferase enzyme responsible for converting phosphoenolpyruvate (PEP) into pyruvate. This reaction initiates a five-step phosphorylation cascade in the bacterial phosphotransferase (PTS) transduction pathway. Under physiological conditions, EI exists in an equilibrium between a functional dimer and an inactive monomer. The monomer-dimer equilibrium is a crucial factor regulating EI activity and the phosphorylation state of the overall PTS. Experimental studies of EI monomeric state have yet been hampered by the dimer's high thermodynamic stability, which prevents its characterization by standard structural techniques. In this study, we modified the dimerization domain of EI (EIC) by mutating three amino acids involved in the formation of intersubunit salt bridges. The engineered variant forms an active dimer in solution that can bind and hydrolyze PEP. Using hydrostatic pressure as an additional perturbation, we were then able to study the complete dissociation of the variant from 1 bar to 2.5 kbar in the absence and the presence of EI natural ligands. Backbone residual dipolar

couplings collected under high-pressure conditions allowed us to determine the conformational ensemble of the isolated EIC monomeric state in solution. Our calculations reveal that three catalytic loops near the dimerization interface become unstructured upon monomerization, preventing the monomeric enzyme from binding its natural substrate. This study provides the first atomic-level characterization of EI's monomeric state and highlights the role of the catalytic loops as allosteric connectors controlling both the activity and oligomerization of the enzyme.

### **Significant Statements**

EI is a central player in bacterial metabolism that controls carbon uptake, virulence, and biofilm formation of bacterial cells. Conserved in Gram-positive and Gram-negative bacteria but absent in eukaryotes, EI is a promising target for antimicrobial design. EI's monomer-dimer equilibrium plays a crucial role in regulating enzymatic activity, yet very little is known about the changes in structure, dynamics, and substrate binding properties undergone upon dimerization. Using a combination of protein engineering and pressure perturbation, we isolated EI monomeric state and characterized its structure in solution by NMR spectroscopy. Our study provides the first atomic-level description of the structural changes accompanying EI dimerization and opens new perspectives for the design of allosteric inhibitors.

### **Introduction**

The carbohydrate phosphotransferase system (PTS) is a key signal transduction pathway controlling the central carbon metabolism and playing important roles in the regulation of several other cellular functions in bacteria, including chemotaxis, biofilm formation, catabolic gene expression, potassium transport, and inducer exclusion (1-5). The PTS comprises a sequential cascade of protein-protein interactions whereby a phosphoryl group originating from phosphoenolpyruvate (PEP) is transferred onto incoming sugars, thereby coupling phosphoryl transfer to active sugar transport across the membrane. There are several sugar-specific branches

of the PTS, but all require Enzyme I (EI) to initiate the phosphoryl transfer cascade (3). Binding of PEP to the C-terminal domain of EI (EIC) initiates the PTS by inducing a series of intra- and interdomain conformational rearrangements (6-13) that result in phosphorylation of EI N-terminal domain (EIN) and subsequent transfer of the phosphoryl group to the histidine phosphocarrier protein HPr. Thereafter, the phosphoryl group is transferred from HPr to the sugar-specific enzymes II and ultimately onto the incoming sugar. Interestingly, EI is ubiquitous and one of the best- conserved proteins in both Gram-positive and Gram-negative bacteria and does not share any significant sequence similarity with eukaryotic proteins, making EI a possible target for the development of wide-spectrum antimicrobials (14-19). In addition, owing to its central metabolic function and complex regulatory role, EI is a frequent objective of metabolic engineering efforts (20-24) and a model system for studying the flux of metabolites across different metabolic networks (25, 26).

The functional form of EI is a ~128-kDa dimer of identical subunits comprising two structurally and functionally distinct domains (27). The EIN domain (residues 1–249) contains the site of phosphorylation (His189) and the binding site for HPr. The EIC domain (residues 261–575) is responsible for dimerization and contains the binding site for PEP. The EIN and EIC domains are connected by a long helical linker (Fig. 1A) (27). EI undergoes a series of large-scale conformational rearrangements during its catalytic cycle, including: (i) a monomer–dimer transition (6, 13), (ii) an expanded-to-compact conformational change within EIC (7, 8), and (iii) an open-to-close transition describing a reorientation of EIN relative to EIC (8, 9, 11, 12). Binding of PEP to EIC shifts the conformational equilibria toward the catalytically competent dimer/compact/close form and activates the enzyme for catalysis (6, 8). As both oligomeric states are present at physiological concentrations of EI (1 - 10  $\mu$ M) (28), the monomer–dimer

equilibrium of the enzyme has often been suggested to be a major regulatory element for PTS (6, 13). Despite the crucial role of the monomer-dimer equilibrium of EI in regulating bacterial metabolism, very little is known about the changes in structure, dynamics, and substrate binding properties that EI undergoes upon monomerization. Therefore, understanding the structural changes upon monomerization would (i) reveal how the coupling among intersubunit conformational dynamics mediates allostery and cooperativity in a functionally dimeric protein, (ii) provide new insight toward the engineering of new bacterial strains for microbial production of chemicals and (iii) indicate new routes for the discovery of antimicrobials that inhibit EI. Yet, at the high protein concentration required by standard structural techniques such as X-ray crystallography or NMR spectroscopy, EI is almost exclusively dimeric ( $K_d < 5 \mu\text{M}$ ) (6, 13), which makes the characterization of the monomeric conformation extremely challenging.

Here we combined protein engineering and hydrostatic pressure perturbation to destabilize the dimeric state of EIC and isolate its monomeric conformation at the high protein concentrations required for solution NMR experiments. We chose pressure perturbation because hydrostatic pressure shifts the system toward a state that occupies the minimal achievable volume, which is reached by increased water density around charged and polar groups and penetration of water molecules in protein cavities (29-31). Therefore, using kbar pressures, it is feasible to finely tune protein-protein interactions and induce partial or total disassembly of protein oligomers (32, 33). Focusing on EIC, the C-terminal domain of EI responsible for dimerization (Fig. 1A), we first designed three single point mutations at the dimerization interface of EIC. At atmospheric pressure the engineered mutant was still able to form an active dimer with a dissociation constant, binding affinity to PEP and enzymatic activity similar to that of the wild type enzyme. In high-pressure conditions ( $> 2 \text{ kbar}$ ) we observed a complete



dissociation of the variant into a stable and well-folded monomer. We then assigned the backbone chemical shift resonances of the monomeric state and obtained an ensemble representation of EIC monomeric conformations in solution by combining Residual Dipolar Couplings with accelerated molecular dynamics simulations. Our data show that three catalytic loops which are part of the dimer interface become more disordered in solution upon monomerization. As a result, the monomeric EIC cannot bind to PEP since those loops are too flexible to orient PEP efficiently towards the binding site. This study provides the first atomic-level characterization of the monomeric EIC conformation, reveals the structural basis for the inactivity of monomeric EI, and highlights the ability of high-pressure perturbation to isolate low-population states that are critical for understanding complex biological pathways.

## Results

*A stable and well-folded monomer of EIC can be isolated at high-pressure.* In this study we focused on the EIC domain of EI from a thermophilic organism (*Thermoanaerobacter tengcongensis*), hereafter called wt-EIC. We chose the thermophilic EIC over its mesophilic homolog because it is more stable in solution and more resilient to structural modifications (34, 35). The full chemical shift assignment of thermophilic EIC is available and besides differences in active site loop dynamics, its sequence and crystal structure are very close to those of the EIC from *E. coli* (60 % similarity; backbone rmsd = 1 Å) (34, 36, 37). We therefore think that wt-EIC is a good model for studying the dimer-to-monomer transition of EI. Inspection of wt-EIC dimerization interface revealed the presence of salt bridge interactions that stabilize the dimeric state of the enzyme. These include salt bridges between R400 and E557 and between D440 and R483 (Fig. 1A). To destabilize the dimerization interface, we mutated R400 into a glutamic acid residue (R400E) and D440 into an arginine residue (D440R). We further destabilized the interface by introducing a third mutation (R559E), a residue nearby the original salt bridge

partner of D400. We first verified if our engineered mutant, henceforth called 3m-EIC, still associates as an active dimer at atmospheric pressure. Analytical ultracentrifugation (AUC) experiments (Fig. S1A,B) and enzymatic activity assays (Fig. S1C) demonstrate that 3m-EIC associates as a dimer at atmospheric pressure with a  $K_d$  comparable to that of the wt-EIC and that the three engineered mutations don't affect the ability of the enzyme to bind and hydrolyze PEP. In this respect, it is important to emphasize that PEP hydrolysis catalyzed by EIC proceeds via the same mechanism as the phosphoryl transfer reaction catalyzed by the full-length EI (the only difference being a water molecule acting as the nucleophile instead of the H189 residue from the EIN domain) and that the enzymatic assays in Fig. S1C are run at experimental conditions in which both wt-EIC and 3m-EIC are fully dimeric.

Next, we investigated the conformational changes experienced by wt-EIC and 3m-EIC under pressure by monitoring the spectral changes in 2D  $^1\text{H}$ - $^{15}\text{N}$  TROSY-HSQC experiments from 1 bar to 2.5 kbar. When pressurized, protein NMR spectra typically display two types of changes: (i) chemical shift changes and (ii) peak intensity changes. The first type of pressure-induced perturbation informs on conformational changes on fast time scale (relative to NMR time scale) typically due to changes in protein surface-water interface and/or small compression of protein native conformations (38). On the other hand, the second type of perturbation (i.e. peak intensity changes) points to major conformational transitions on a slow time scale (e.g. changes in folded/unfolded state populations or monomer/dimer populations) (32, 33, 39). While both wt-EIC and 3m-EIC displayed chemical shift changes under pressure, significant peak intensity changes were only observed for 3m-EIC suggesting that this variant undergoes major conformational transitions from 1 bar to 2.5 kbar (Fig. 1B). Since the 2D  $^1\text{H}$ - $^{15}\text{N}$  spectrum of 3m-EIC collected at 2 kbar shows no evidence of unfolding (Fig. S2), the major peak intensity

changes observed for this variant were interpreted as pressure-induced dissociation of the native dimer into monomers.

To confirm that our engineered variant is monomeric at 2 kbar, we investigated the picosecond to nanosecond time scale dynamics of wt-EIC and 3m-EIC by measuring the transverse ( $^{15}\text{N}$  - $R_2$ ) and longitudinal ( $^{15}\text{N}$  - $R_1$ ) relaxation rates at atmospheric and high-pressure conditions (Fig. 1C). The  $R_2/R_1$  ratio can be used to estimate the protein rotational correlation time ( $\tau_m$ ) (40). We found that the average  $R_2/R_1$  ratios measured for wt-EIC were not affected by pressure, with average values of  $107 \pm 7$  and  $102 \pm 10$  at 1 bar and 2 kbar respectively, which translate into a  $\tau_m \sim 25$  ns that is close to the value predicted for the EIC dimer based on Stokes' Law ( $\sim 29$  ns). At atmospheric pressure, the engineered variant 3m-EIC displays average  $R_2/R_1$  ratios comparable to that of wt-EIC ( $R_2/R_1 = 122 \pm 30$ , for an estimated  $\tau_m$  of 26 ns). Remarkably, the relaxation data measured for 3m-EIC at 2 kbar are drastically different from those measured at atmospheric pressure, with an average  $R_2/R_1$  ratio of  $33 \pm 4$  and a  $\tau_m \sim 13$  ns that is consistent with the rotational correlation time predicted for the monomeric EIC (15 ns) (Fig. 1C). Altogether, these relaxation experiments confirm that the dimeric 3m-EIC dissociates under pressure into a stable monomeric conformation that can be isolated at 2 kbar.

*Thermodynamics of EIC dimer-to-monomer transition.* Using the collection of 2D  $^1\text{H}$ - $^{15}\text{N}$  TROSY-HSQC spectra collected from 1 bar to 2.5 kbar for wt-EIC and 3m-EIC we globally fitted the average change of cross-peak intensity as a function of pressure with a simple two state dimer-to-monomer model. As shown in Figure 1D for the variant 3m-EIC, both the intensity of the native dimer cross-peaks (in orange) and intensity of new cross-peaks attributed to the monomeric conformation (in red) can be accurately fitted with our model. These results show that the midpoint of the dimer-to-monomer transition occurs for 3m-EIC at around 1.3 kbar and

that at 2 kbar the engineered variant is predominantly (> 95%) monomeric. On the other hand, wt-EIC (in blue) is only moderately affected by pressure with at least 70% of the dimeric population subsisting at 2.5 kbar. We also compared the stability of 3m-EIC under pressure in the absence and in the presence of either PEP or  $\alpha$ -ketoglutarate ( $\alpha$ KG). PEP is the natural substrate of EI in the PTS pathway while the small-molecule metabolite  $\alpha$ KG acts as an allosteric stimulator or competitive inhibitor depending on the oligomeric state of the enzyme (6). Both PEP and  $\alpha$ KG have been shown to decrease the equilibrium dissociation constant for EIC dimerization by more than ten-fold (4). By fitting the changes of cross-peak intensities from a series of 2D  $^1\text{H}$ - $^{15}\text{N}$  TROSY-HSQC spectra collected from 1 bar to 2.5 kbar for apo 3m-EIC in the absence and the in presence of PEP or  $\alpha$ KG, we extracted the changes in dimerization free-energy ( $\Delta G$ ), in partial volume ( $\Delta V$ ) and the extrapolated dimer dissociation constants at atmospheric pressure ( $K_d$ ) (Fig. 1E and Table S1).

We found that the  $K_d$  of the apo 3m-EIC is very small, about 0.1 nM, which is consistent with the  $K_d$  of ~5 nM previously reported for the E. coli EIC (41) (the slight difference likely reflects the increased stability of the thermophilic EIC compared to its mesophilic homolog). The addition of PEP and  $\alpha$ KG leads to a decrease in  $K_d$  by 2 and 3 orders of magnitude respectively and a concomitant increase in  $\Delta G$  by more than ~1 kcal and ~2 kcal respectively (Table S1). These data confirm that the engineered mutations in 3m-EIC modify the network of interactions at the dimerization interface rendering it more susceptible to pressure perturbation without drastically affecting its dissociation constant at atmospheric pressure. These results also highlight that the allosteric coupling between the substrate binding site and the dimerization interface, which is a hallmark of EI activity (6), is still effective in 3m-EIC, as evidenced by the dimer stabilization upon addition of PEP and  $\alpha$ KG.

*Three disordered catalytic loops prevent PEP from binding to EIC in the monomeric state.* To characterize structural changes associated with the dimer-to-monomer transition of 3m-EIC, we collected backbone amide  $^1\text{DNH}$  at 1 bar and 2 kbar using Pf1 phage as an alignment medium. Singular value decomposition (SVD) fitting of the 1 bar  $^1\text{DNH}$  RDC from well-defined secondary structures to the X-ray coordinates of a single subunit and of the full dimer of wt-EIC (PDB: 2XZ7) (35) yielded R-factors of 27% and 28%, respectively (Fig. S3 lower left panel). These good correlations between experimental and back-calculated RDC data indicate that the tertiary and quaternary structures of 3m-EIC at 1 bar are similar to those observed in the X-ray structure of wt-EIC. On the other hand, the  $^1\text{DNH}$  RDC measured at 2 kbar are in poor agreement with the crystal structure of wt-EIC (R-factor ~57%) (Fig. S3 lower right panel), indicating that monomerization of 3m-EIC upon increasing pressure is coupled to a change in the tertiary fold. As a control, we also measured a set of  $^1\text{DNH}$  RDC in the same alignment medium for wt-EIC at 1 bar and 2 kbar. For both datasets, the experimental RDCs from well-defined secondary structures are in good agreement with the ones calculated from the reference X-ray structure (R-factors of 25% and 23%, respectively) (Fig. S3 upper panels), confirming that the tertiary and quaternary folds of wt-EIC are not affected by pressure.

In order to visualize the changes in structure and dynamics that EIC undergoes upon monomerization, we have calculated structural ensembles for wt-EIC and 3m-EIC at 1 bar and 2 kbar by coupling the experimental  $^1\text{DNH}$  RDC data with accelerated molecular dynamics (aMD) simulations. This combined aMD/NMR protocol has been proven successful in generating structural ensembles of dynamical proteins that satisfy solution NMR data (42). 7- and 15-member ensembles were necessary to fulfill the complete set (including flexible structural regions) of RDC data measured for wt-EIC at 1 bar (R-factor ~23%) and 2 kbar (R-factor ~27%),

respectively (Fig. S4 upper panels). Similarly, the data measured for 3m-EIC at low and high pressures were satisfied by an 8- (R-factor ~27%) and 20-member (R-factor ~25%) ensemble, respectively (Fig. S4 lower panels). The modeled structural ensembles are visualized in Figure 2A. The average structures from each ensemble are compared to the reference X-ray structure of EIC in Figure 2B. Analysis of the B-factors calculated from the conformational ensembles reveals that dimeric EIC (wt-EIC at 1 bar and 2 kbar, and 3m-EIC at 1 bar) is more rigid than monomeric EIC (3m-EIC at 2 kbar) (Fig. 2A). Interestingly, the more pronounced changes in flexibility upon monomerization occur at the C-terminal helix and at the loops comprising the protein active site (Fig. 2B). These same regions are also the ones displaying the largest conformational changes upon monomerization. Indeed, while the average structures calculated for the wt-EIC at 1 bar, wt-EIC at 2 kbar, and 3m-EIC at 1 bar ensembles are indistinguishable from the X-ray structure of dimeric wt-EIC (Fig. 2C), the average structure obtained for the 3m-EIC ensemble at 2 kbar indicates that formation of monomeric EIC at high pressure is coupled to a conformational transition involving the active site loops  $\alpha 3\beta 3$ ,  $\alpha 6\beta 6$  and  $\alpha 7\beta 7$  (Fig. 2C).

Altogether, these calculations reveal that while the dimer-to-monomer transition of 3m-EIC preserves the overall fold of the monomeric subunit in EIC dimer, it is accompanied by significant changes in local structure and dynamics at the PEP binding site. In particular, the partial unfolding of the catalytic loops  $\alpha 3\beta 3$ ,  $\alpha 6\beta 6$  and  $\alpha 7\beta 7$  (Fig. 2) suggests that the monomeric EIC cannot bind PEP because those loops are too flexible to orient PEP efficiently towards the binding site. To verify this prediction, we compared the 2D  $^1\text{H}$ - $^{15}\text{N}$  TROSY-HSQC spectra acquired for 3m-EIC at 1 bar and 2 kbar in the absence and in the presence of 10 mM PEP. As expected, we observed a significant chemical shift perturbation at atmospheric pressure for the residues located at the binding sites (Fig. 3A). On the other hand, no chemical shift

perturbation was observed for 3m-EIC at 2 kbar (Fig. 3A), indicating that EIC cannot bind to its natural substrate in the monomeric state. Consistent with these data, we found that wt-EIC can still hydrolyze PEP in high-pressure conditions, while 3m-EIC is completely inactive at high-pressure (Fig. 3B), confirming that EIC is unable to bind and subsequently degrade PEP in the monomeric state.

## Discussion

Sparsely populated states involved in conformational selection and enzyme catalysis play a crucial role in many biological pathways but the low population and transient nature of these states make them invisible to most structural biology techniques (43). Solution NMR spectroscopy has emerged as a method of choice for characterizing low-lying states at an atomic level, with multiple experiments dedicated to the indirect detection and characterization of transient intermediate states (38, 44-48). In this work, we focused on the monomeric intermediate state of EI, the enzyme responsible for initiating the phosphoryl transfer cascade in the PTS pathway. The high dimer affinity of EI ( $K_d < 5 \mu\text{M}$ ) renders the structural characterization of the monomeric state extremely challenging. Yet, obtaining an atomic-level description of this intermediate state is crucial to fully understand the molecular mechanisms underlying EI catalytic activity and regulation. Here, we combined protein engineering and pressure perturbation to shift the dimer-monomer equilibrium of EIC in order to isolate and determine the structural ensemble of the monomeric state in solution. We found conditions at which EIC is predominantly monomeric (>95%) and we were therefore able to directly measure backbone  $^1\text{DHN}$  RDCs of EIC monomeric state without relying on indirect detection.

The three mutations engineered in 3m-EIC (R400E, D440R, and R559) were designed to change the balance between the electrostatic and hydrophobic interactions at the dimerization interface to make it more sensitive to pressure perturbation. Analytical ultracentrifugation (Fig.

S1A,B), pressure titration experiments (Fig. 1D), and enzyme kinetic assays (Fig. S1C) show that the mutations did not affect the ability of 3m-EIC to form an active dimer at atmospheric pressure. The calculated dimerization  $K_d$  is very low ( $\sim 0.1$  nM), which is comparable to the  $K_d$  previously reported for the mesophilic EIC (41). We found that the volume change upon monomerization is rather large ( $\Delta V = -153 \pm 2$  ml/mol), which corresponds to the van der Waals volume of about 12 water molecules. The magnitude of  $\Delta V$  likely reflects the preferential hydration of polar and charged side chains exposed upon monomerization as well as the potential penetration of water molecules in small cavities near the dimerization interface (29, 33, 49). Remarkably, the pressure titration experiments revealed that upon binding, PEP stabilizes the dimeric state by +2.3 kcal/mol relative to the apo 3m-EIC, which is significantly greater than the effect of  $\alpha$ KG (Fig. 1E and Table S1). PEP and  $\alpha$ KG bind to the same site in EIC and the differences between the binding modes of these natural substrates have been explored by solution NMR experiments and docking simulations (4) but the actual differences in terms of dimerization thermodynamics have yet never been described. Our high-pressure NMR experiments provide here the first quantitative thermodynamic characterization of the allosteric coupling between substrate binding and dimerization. These results show that PEP stabilizes EIC dimeric state significantly more than  $\alpha$ KG does, likely due to the additional interactions between PEP's phosphate group with the side chains of R296, R332 and K340 (4, 34).

Application of hydrostatic pressure from 1 bar to 2.5 kbar shifts the equilibrium toward the monomeric state of EIC while preserving the overall tertiary structure of the protein (Fig. 1D and Fig. S2). We found that 3m-EIC becomes fully monomeric at pressure  $\geq 2$  kbar, which allowed us to directly determine the structural features of EIC monomeric state by measuring  $^1\text{DNH}$  RDCs in high-pressure conditions. Comparison of the experimental  $^1\text{DNH}$  RDCs with the



RDCs predicted for a reference X-ray structure demonstrates that the dimer-to-monomer transition of 3m-EIC is accompanied by significant structural changes (Fig. S3). With the help of all-atom accelerated molecular dynamics simulations, we were then able to generate a 20-member conformational ensemble of the monomeric 3m-EIC that would satisfy the experimental  $^1\text{DNH}$  RDCs (Fig. S4). Examination of the conformational ensemble and average structure revealed that while the overall tertiary structure is preserved, three catalytic loops become significantly disordered in the monomeric state (Fig. 2). Indeed, the loops  $\alpha 3\beta 3$ ,  $\alpha 6\beta 6$  and to a lesser extent  $\alpha 7\beta 7$ , show large structural deviations from the reference X-ray structure indicative of partial unfolding upon monomerization (Fig. 2C). Since EIC is inactive and unable to bind PEP in the monomeric state (Fig. 3A and B), these results provide the first mechanistic framework explaining why dimerization is strictly required for EI to be active. The catalytic loops  $\alpha 3\beta 3$ ,  $\alpha 6\beta 6$  and  $\alpha 7\beta 7$  seem to play a key role in establishing the allosteric coupling between the active site and the dimerization interface. Overall, our experiments suggest that dimerization is required for these catalytic loops to be fully structured, which in turn allows the physiological ligands PEP and  $\alpha\text{KG}$  to bind to the EI active site (Fig. 3C).

### Materials and Methods

wt-EIC was cloned into a pET21a vector incorporating a His-tagged EIN solubility tag at the N-terminus (50). The R400E, D440R, and R559E mutations were introduced using QuikChange II Site-Directed Mutagenesis Kit (Agilent), and the results were verified by DNA sequencing. Expression and purification of uniformly  $^{15}\text{N}$ -,  $^2\text{H}/^{15}\text{N}$ -, and  $^2\text{H}/^{15}\text{N}/^{13}\text{C}$ -labelled wt-EIC and 3m-EIC were performed as previously described (37). All NMR spectra were acquired at 40 °C on Bruker 600, 700 and 800 MHz spectrometers equipped with Z-shielded gradient triple resonance cryoprobes. Hydrostatic pressure in the sample was controlled using a commercial ceramic high-pressure NMR cell and an automatic pump system (Daedalus

Innovations, Philadelphia, PA).  $^{15}\text{N}$ -R<sub>1</sub> and  $^{15}\text{N}$ -R<sub>1ρ</sub> experiments for  $^{15}\text{N}$ -labelled wt- and 3m-EIC were carried using heat-compensated pulse schemes with a TROSY readout (51). Backbone amide  $^1\text{DNH}$  RDCs were measured for on  $^2\text{H}$ ,  $^{15}\text{N}$ -labelled samples of wt- and 3m-EIC at the 700MHz by taking the difference in  $^1\text{JNH}$  scalar couplings in aligned and isotropic media. The alignment media employed was phage pf1 (16 mg/mL; ASLA Biotech, Riga, Latvia) (52), and  $^1\text{JNH}$  couplings were measured using the amide RDCs by TROSY (ARTSY) pulse scheme (53). SVD analysis of RDCs was carried out using Xplor-NIH (54). aMD simulations were run using AMBER 16 (55). For details, see SI Materials and Methods.

### Acknowledgement

This work was supported by funds from NIGMS R35GM133488 (to V.V.), from the Roy J. Carver Charitable Trust (to V.V.), and by the Intramural Research Program of the National Institutes of Health, the National Institute of Diabetes and Digestive and Kidney Disease) (to R.G.). J.R. acknowledges the Iowa State University College of Liberal Arts and Sciences and the Roy J. Carver Charitable Trust for their support.

### References

1. Deutscher J, et al. (2014) The Bacterial Phosphoenolpyruvate:Carbohydrate Phosphotransferase System: Regulation by Protein Phosphorylation and Phosphorylation-Dependent Protein-Protein Interactions. *Microbiology and Molecular Biology Reviews* 78(2):231.
2. Postma PW, Lengeler JW, & Jacobson GR (1993) Phosphoenolpyruvate:carbohydrate phosphotransferase systems of bacteria. *Microbiological Reviews* 57(3):543.
3. Clore GM & Venditti V (2013) Structure, dynamics and biophysics of the cytoplasmic protein-protein complexes of the bacterial phosphoenolpyruvate: sugar phosphotransferase system. *Trends Biochem Sci* 38(10):515-530.
4. Venditti V, Ghirlando R, & Clore GM (2013) Structural Basis for Enzyme I Inhibition by  $\alpha$ -Ketoglutarate. *ACS Chemical Biology* 8(6):1232-1240.

5. Doucette CD, Schwab DJ, Wingreen NS, & Rabinowitz JD (2011)  $\alpha$ -ketoglutarate coordinates carbon and nitrogen utilization via enzyme I inhibition. *Nature Chemical Biology* 7(12):894-901.
6. Nguyen TT, Ghirlando R, & Venditti V (2018) The oligomerization state of bacterial enzyme I (EI) determines EI's allosteric stimulation or competitive inhibition by  $\alpha$ -ketoglutarate. *Journal of Biological Chemistry*.
7. Venditti V & Clore GM (2012) Conformational Selection and Substrate Binding Regulate the Monomer/Dimer Equilibrium of the C-terminal domain of Escherichia coli Enzyme I. *Journal of Biological Chemistry* 287(32):26989-26998.
8. Venditti V, Tugarinov V, Schwieters CD, Grishaev A, & Clore GM (2015) Large interdomain rearrangement triggered by suppression of micro- to millisecond dynamics in bacterial Enzyme I. *Nature Communications* 6(1):5960.
9. Venditti V, Schwieters CD, Grishaev A, & Clore GM (2015) Dynamic equilibrium between closed and partially closed states of the bacterial Enzyme I unveiled by solution NMR and X-ray scattering. *Proceedings of the National Academy of Sciences* 112(37):11565.
10. Suh J-Y, Cai M, & Clore GM (2008) Impact of phosphorylation on structure and thermodynamics of the interaction between the N-terminal domain of enzyme I and the histidine phosphocarrier protein of the bacterial phosphotransferase system. *J Biol Chem* 283(27):18980-18989.
11. Teplyakov A, et al. (2006) Structure of phosphorylated enzyme I, the phosphoenolpyruvate:sugar phosphotransferase system sugar translocation signal protein. *Proceedings of the National Academy of Sciences* 103(44):16218.
12. Schwieters CD, et al. (2010) Solution Structure of the 128 kDa Enzyme I Dimer from Escherichia coli and Its 146 kDa Complex with HPr Using Residual Dipolar Couplings and Small- and Wide-Angle X-ray Scattering. *Journal of the American Chemical Society* 132(37):13026-13045.
13. Patel HV, Vyas KA, Savtchenko R, & Roseman S (2006) The Monomer/Dimer Transition of Enzyme I of the Escherichia coli Phosphotransferase System. *Journal of Biological Chemistry* 281(26):17570-17578.
14. Kok M, Bron G, Erni B, & Mukhija S (2003) Effect of enzyme I of the bacterial phosphoenolpyruvate:sugar phosphotransferase system (PTS) on virulence in a murine model. *Microbiology* 149(9):2645-2652.
15. Edelstein PH, Edelstein MA, Higa F, & Falkow S (1999) Discovery of virulence genes of Legionella pneumophila by using signature tagged mutagenesis in a guinea pig pneumonia model. *Proc Natl Acad Sci U S A* 96(14):8190-8195.
16. Hava DL & Camilli A (2002) Large-scale identification of serotype 4 Streptococcus pneumoniae virulence factors. *Mol Microbiol* 45(5):1389-1406.

17. Nguyen TT & Venditti V (2020) An allosteric pocket for inhibition of bacterial Enzyme I identified by NMR-based fragment screening. *Journal of Structural Biology*: X 4:100034.
18. Jones AL, Knoll KM, & Rubens CE (2000) Identification of *Streptococcus agalactiae* virulence genes in the neonatal rat sepsis model using signature-tagged mutagenesis. *Mol Microbiol* 37(6):1444-1455.
19. Lau GW, et al. (2001) A functional genomic analysis of type 3 *Streptococcus pneumoniae* virulence. *Mol Microbiol* 40(3):555-571.
20. Chubukov V, et al. (2017) Engineering glucose metabolism of *Escherichia coli* under nitrogen starvation. *npj Systems Biology and Applications* 3(1):16035.
21. Yan Q & Fong SS (2018) Increasing carbon source uptake rates to improve chemical productivity in metabolic engineering. *Current Opinion in Biotechnology* 53:254-263.
22. Gosset G (2005) Improvement of *Escherichia coli* production strains by modification of the phosphoenolpyruvate:sugar phosphotransferase system. *Microbial Cell Factories* 4(1):14.
23. Floras N, Xiao J, Berry A, Bolivar F, & Valle F (1996) Pathway engineering for the production of aromatic compounds in *Escherichia coli*. *Nature Biotechnology* 14(5):620-623.
24. Zampieri M, Hörl M, Hotz F, Müller NF, & Sauer U (2019) Regulatory mechanisms underlying coordination of amino acid and glucose catabolism in *Escherichia coli*. *Nature Communications* 10(1):3354.
25. Long CP, Au J, Sandoval NR, Gebreselassie NA, & Antoniewicz MR (2017) Enzyme I facilitates reverse flux from pyruvate to phosphoenolpyruvate in *Escherichia coli*. *Nature Communications* 8(1):14316.
26. Shimizu K & Matsuoka Y (2019) Regulation of glycolytic flux and overflow metabolism depending on the source of energy generation for energy demand. *Biotechnology Advances* 37(2):284-305.
27. Chauvin F, Brand L, & Roseman S (1996) Enzyme I: the first protein and potential regulator of the bacterial phosphoenolpyruvate: glycolate phosphotransferase system. *Research in Microbiology* 147(6):471-479.
28. Mattoo RL & Waygood EB (1983) Determination of the levels of HPr and enzyme I of the phosphoenolpyruvate–sugar phosphotransferase system in *Escherichia coli* and *Salmonella typhimurium*. *Canadian Journal of Biochemistry and Cell Biology* 61(1):29-37.
29. Roche J, et al. (2012) Cavities determine the pressure unfolding of proteins. *Proceedings of the National Academy of Sciences* 109(18):6945.
30. Grigera JR & McCarthy AN (2010) The Behavior of the Hydrophobic Effect under Pressure and Protein Denaturation. *Biophysical Journal* 98(8):1626-1631.

31. Chalikian TV & Macgregor RB (2009) Origins of Pressure-Induced Protein Transitions. *Journal of Molecular Biology* 394(5):834-842.
32. Alderson TR, et al. (2019) Local unfolding of the HSP27 monomer regulates chaperone activity. *Nature Communications* 10(1):1068.
33. Louis JM & Roche J (2016) Evolution under Drug Pressure Remodels the Folding Free-Energy Landscape of Mature HIV-1 Protease. *Journal of Molecular Biology* 428(13):2780-2792.
34. Dotas RR, et al. (2020) Hybrid Thermophilic/Mesophilic Enzymes Reveal a Role for Conformational Disorder in Regulation of Bacterial Enzyme I. *Journal of Molecular Biology* 432(16):4481-4498.
35. Navdaeva V, et al. (2011) Phosphoenolpyruvate: Sugar Phosphotransferase System from the Hyperthermophilic *Thermoanaerobacter tengcongensis*. *Biochemistry* 50(7):1184-1193.
36. Oberholzer AE, et al. (2005) Crystal Structure of the Phosphoenolpyruvate-binding Enzyme I-Domain from the *Thermoanaerobacter tengcongensis* PEP: Sugar Phosphotransferase System (PTS). *Journal of Molecular Biology* 346(2):521-532.
37. Dotas RR & Venditti V (2019) Resonance assignment of the 128 kDa enzyme I dimer from *Thermoanaerobacter tengcongensis*. *Biomol NMR Assign* 13(2):287-293.
38. Kitahara R, Hata K, Li H, Williamson MP, & Akasaka K (2013) Pressure-induced chemical shifts as probes for conformational fluctuations in proteins. *Progress in Nuclear Magnetic Resonance Spectroscopy* 71:35-58.
39. Roche J, et al. (2013) Effect of Internal Cavities on Folding Rates and Routes Revealed by Real-Time Pressure-Jump NMR Spectroscopy. *Journal of the American Chemical Society* 135(39):14610-14618.
40. Kay LE, Torchia DA, & Bax A (1989) Backbone dynamics of proteins as studied by nitrogen-15 inverse detected heteronuclear NMR spectroscopy: application to staphylococcal nuclease. *Biochemistry* 28(23):8972-8979.
41. Patel HV, et al. (2006) Properties of the C-terminal Domain of Enzyme I of the *Escherichia coli* Phosphotransferase System. *Journal of Biological Chemistry* 281(26):17579-17587.
42. Purslow JA, et al. (2018) Active Site Breathing of Human Alkbh5 Revealed by Solution NMR and Accelerated Molecular Dynamics. *Biophysical Journal* 115(10):1895-1905.
43. Roche J & Royer CA (2018) Lessons from pressure denaturation of proteins. *Journal of The Royal Society Interface* 15(147):20180244.
44. Roche J, Royer CA, & Roumestand C (2019) Chapter Eleven - Exploring Protein Conformational Landscapes Using High-Pressure NMR. *Methods in Enzymology*, ed Wand AJ (Academic Press), Vol 614, pp 293-320.

45. Nguyen LM & Roche J (2017) High-pressure NMR techniques for the study of protein dynamics, folding and aggregation. *Journal of Magnetic Resonance* 277:179-185.
46. Caro JA & Wand AJ (2018) Practical aspects of high-pressure NMR spectroscopy and its applications in protein biophysics and structural biology. *Methods* 148:67-80.
47. Roche J (2019) High-Pressure NMR of Biological Systems in Solution. *eMagRes*:121-126.
48. Venditti V, Egner TK, & Clore GM (2016) Hybrid Approaches to Structural Characterization of Conformational Ensembles of Complex Macromolecular Systems Combining NMR Residual Dipolar Couplings and Solution X-ray Scattering. *Chem Rev* 116(11):6305-6322.
49. Rouget J-B, et al. (2011) Size and Sequence and the Volume Change of Protein Folding. *Journal of the American Chemical Society* 133(15):6020-6027.
50. Khatiwada B, Purslow JA, Underbakke ES, & Venditti V (2020) N-terminal fusion of the N-terminal domain of bacterial enzyme I facilitates recombinant expression and purification of the human RNA demethylases FTO and Alkbh5. *Protein Expression and Purification* 167:105540.
51. Lakomek N-A, Ying J, & Bax A (2012) Measurement of  $^{15}\text{N}$  relaxation rates in perdeuterated proteins by TROSY-based methods. *J Biomol NMR* 53(3):209-221.
52. Clore GM, Starich MR, & Gronenborn AM (1998) Measurement of Residual Dipolar Couplings of Macromolecules Aligned in the Nematic Phase of a Colloidal Suspension of Rod-Shaped Viruses. *Journal of the American Chemical Society* 120(40):10571-10572.
53. Fitzkee NC & Bax A (2010) Facile measurement of  $^1\text{H}$ – $^{15}\text{N}$  residual dipolar couplings in larger perdeuterated proteins. *J Biomol NMR* 48(2):65-70.
54. Schwieters CD, Kuszewski JJ, Tjandra N, & Marius Clore G (2003) The Xplor-NIH NMR molecular structure determination package. *Journal of Magnetic Resonance* 160(1):65-73.
55. Case DA, et al. (2005) The Amber biomolecular simulation programs. *Journal of Computational Chemistry* 26(16):1668-1688.

## Figures

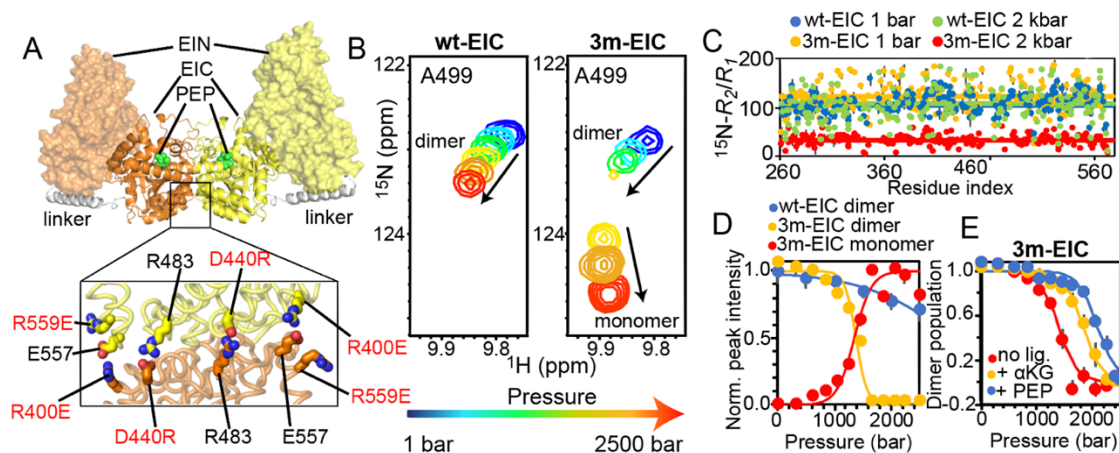


**Figure 1. A folded EIC monomer at high pressure.** (A) Solution structure of the full-length EI dimer. The two subunits are colored orange and yellow, respectively. The EIC and EIN domains are shown as transparent surface and solid cartoon, respectively. The helical linker is colored white. PEP modeled in the active site on EIC is shown as green spheres. In the lower panel, the three single point mutations introduced at the dimer interface to engineer the 3m-EIC construct are highlighted. (B) Pressure titration for a representative  $^1\text{H}$ - $^{15}\text{N}$  NMR cross-peak that reports on the monomer/dimer equilibrium in wt-EIC (left) and 3m-EIC (right). The relationship between cross-peak color and pressure is given by the arrow underneath the spectra (i.e. blue: 1 bar; red: 2.5 kbar). (C)  $^{15}\text{N}$ - $R_2/R_1$  data measured for wt-EIC at 1 bar (blue), wt-EIC at 2 kbar (green), 3m-EIC at 1 bar (orange) and 3m-EIC at 2 kbar (red) are plotted versus the residue index. The average  $R_2/R_1$  value of each construct is shown as a solid line. (D) Normalized signal intensities are averaged over all NMR cross-peaks displaying distinct signals for the monomer and dimer species during the pressure titration on 3m-EIC (i.e. see panel B). The normalized averaged intensities for the wt-EIC dimer (blue circles), 3m-EIC dimer (orange circles) and 3m-EIC monomer (red circles) are plotted versus the external pressure (note that no NMR signal is

observable for the wt-EIC monomer in the tested pressure range). Modeling of the data (see SI Materials and Methods) is shown as solid curves. (E) The fractional population of dimer obtained by pressure titration experiments on 3m-EIC in the absence of ligands (red circles) and in the presence of 20 mM  $\alpha$ KG (orange circles) or PEP (blue circles) is plotted versus the external pressure. Modeled curves (see SI Materials and Methods) are shown as solid lines.

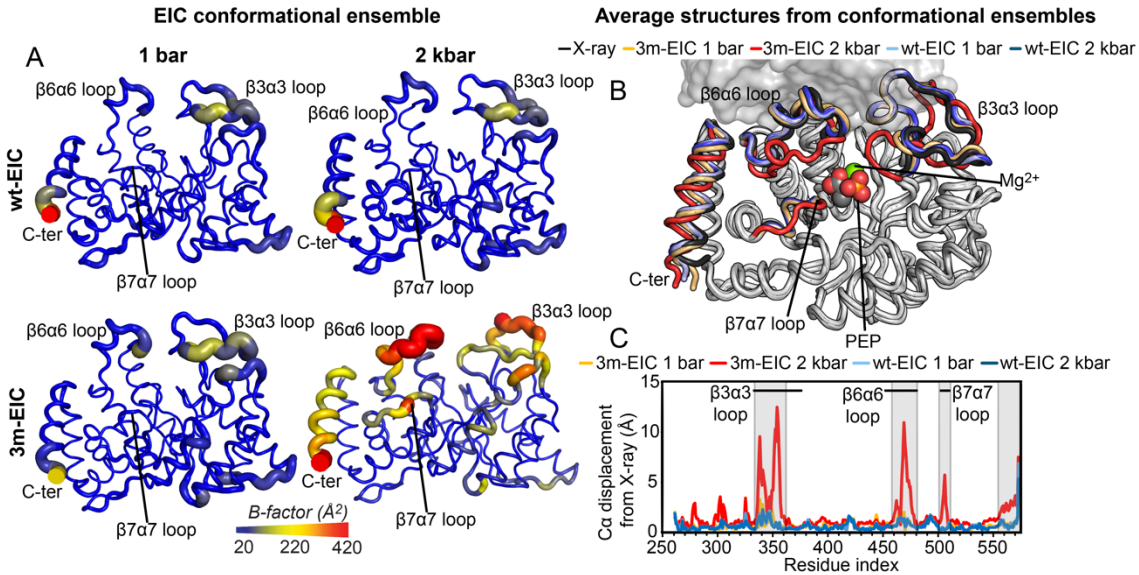


**Figure 2. Monomerization affects the structure and dynamics of the EIC active site. (A)**

Sausage representation of the aMD/RDC conformational ensembles generated for wt-EIC at 1 bar (top left), wt-EIC at 2 kbar (top right), 3m-EIC at 1 bar (bottom left), and 3m-EIC and 2 kbar (bottom right). Cartoons are colored according to the B-factor, as indicated by the color bar. B-factors were calculated using the formula  $B_i = 8\pi^2 U_i^2$ , where  $B_i$  and  $U_i$  are the B-factor and mean-square displacement of atom  $i$ , respectively. (B) The average structures from the conformational ensembles are superimposed on the crystal structure of wt-EIC. Ensembles were calculated for a single subunit of the EIC dimer (see SI Materials and Methods). The second subunit from the crystal structure is displayed as a transparent gray surface as a reference. PEP and  $\text{Mg}^{2+}$  (not used in the ensemble calculation) are shown as spheres in the EIC active site. The



C-terminal helix and the  $\alpha 3\beta 3$ ,  $\alpha 6\beta 6$  and  $\alpha 7\beta 7$  loops are colored black, light blue, dark blue, orange, and red for the X-ray structure, wt-EIC at 1 bar, wt-EIC at 2 kbar, 3m-EIC at 1 bar and 3m-EIC at 2 kbar, respectively. (C) The  $C\alpha$  displacement from the X-ray structure calculated for the average structure of wt-EIC at 1 bar (light blue), wt-EIC at 2 kbar (dark blue), 3m-EIC at 1 bar (orange), and 3m-EIC at 2 kbar (red) is plotted versus the residue index. Residues experiencing large  $C\alpha$  displacement upon monomerization are boxed. The location on the  $\alpha 3\beta 3$ ,  $\alpha 6\beta 6$  and  $\alpha 7\beta 7$  is indicated by black horizontal lines.

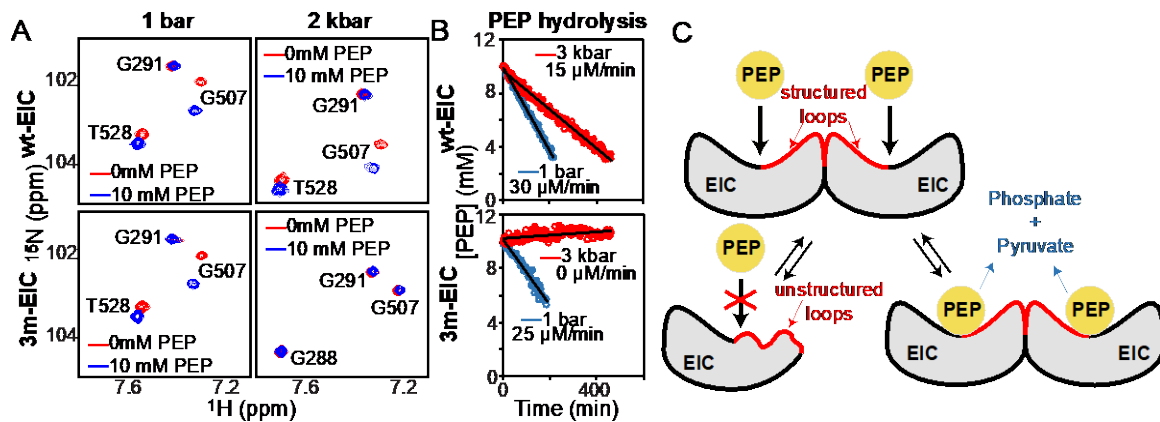


**Figure 3. Monomeric EIC does not bind nor hydrolyze PEP.** (A) A selected region of the  $^1\text{H}$ - $^{15}\text{N}$  TROSY spectrum of wt-EIC at 1 bar (top left), wt-EIC at 2 kbar (top right), 3m-EIC at 1 bar (bottom left), and 3m-EIC at 2 kbar (bottom right) acquired in the absence (red) and in the presence (blue) of 10 mM PEP is shown. Note that monomerization of 3m-EIC at 2 kbar generates large shifts for T528 and G288 cross-peaks. (B) Rate of the PEP hydrolysis reaction catalyzed by 150  $\mu\text{M}$  wt-EIC (top) and 3m-EIC (bottom) at 65  $^{\circ}\text{C}$  and an external pressure of 1 bar (blue) and 3 kbar (red). A pressure of 3 kbar was used to ensure that the monomer-dimer equilibrium of 3m-EIC is fully shifted toward the monomeric species. (C) Schematic representation of the effect of monomerization on the structure and biological activity of EIC.

The catalytic loops  $\alpha 3\beta 3$ ,  $\alpha 6\beta 6$ , and  $\alpha 7\beta 7$ , which form a large portion of the dimer interface, are largely disordered in monomeric EIC and become ordered upon dimerization.

### Supporting Materials

**NMR Spectroscopy.** NMR samples were prepared in 20 mM Tris-HCl (pH 7.4), 100 mM NaCl, 4 mM MgCl<sub>2</sub>, 1 mM EDTA, 2 mM DTT, and 90% H<sub>2</sub>O/10% D<sub>2</sub>O (v/v). Protein concentration was 0.4–0.8 mM (unless stated otherwise). Spectra were processed in NMRPipe (1) and analyzed using the program and SPARKY (<http://www.cgl.ucsf.edu/home/sparky>), respectively.

Assignments of the <sup>1</sup>H-<sup>15</sup>N TROSY spectrum of wt-EIC at 1 bar 40 °C was obtained previously (2). The <sup>1</sup>H-<sup>15</sup>N TROSY spectrum of wt-EIC at 2 kbar and 40 °C was assigned by tracking the peaks over a series of 2D spectra collected from 1 bar to 2 kbar. Sequential <sup>1</sup>H-<sup>15</sup>N, <sup>13</sup>C backbone resonance assignment of the 3m-EIC at 1 bar and 2 kbar, was carried out 40 °C using a TROSY versions of conventional 3D triple resonance correlation experiments (HNCO, HN(CA)CO, HNCA, HN(CO)CA, HNCB and HN(COCA)CB) (3). The chemical shifts assigned for 3m-EIC at 1 bar and 2 kbar have been deposited in the BioMagResBank (accession nos. 50695 and 50694, respectively).

The thermodynamics of the EIC dimer-to-monomer equilibrium were investigated by running <sup>1</sup>H-<sup>15</sup>N TROSY spectra of <sup>15</sup>N-labelled wt- and 3m-EIC at increasing hydrostatic pressure from 1 bar to 2.5 kbar. Data were measured in the absence and in the presence of 10 mM  $\alpha$ KG or PEP. Signal intensities for the NMR peaks reporting on the monomer/dimer equilibrium (i.e. NMR resonances for which distinct peaks for the monomer and dimer species are observed in the pressure titration on 3m-EIC) were quantified and their pressure dependence was fit globally using a two-state equilibrium model to obtain the free energy difference ( $\Delta G$  in cal/mol) and volume changes ( $\Delta V$  in mL/mol) between the dimeric and monomeric states.

$$I(p) = \frac{D + M e^{\left(\frac{\Delta G + p\Delta V}{-RT}\right)}}{e^{\left(\frac{\Delta G + p\Delta V}{-RT}\right)} + 1} \quad (1)$$

Here,  $I(p)$  is the intensity at each pressure,  $D$  is the maximum intensity (fully dimeric state) and  $M$  is the minimum intensity (fully monomeric state).  $T$  is the temperature in K and  $R$  is the universal gas constant.

The dimer dissociation constant is calculated from  $\Delta G$  using the following procedure:

$$K_d = \frac{[monomer]^2}{[dimer]} = \frac{[EIC_M]^2}{0.5[EIC_D]} \quad (2)$$

where  $[EIC_M]$  is the concentration of EIC in the monomeric state and  $[EIC_D]$  is the concentration of EIC subunits in the dimeric state (which corresponds to two times the concentration of dimer). The relationship among  $[EIC_M]$ ,  $[EIC_D]$  and  $\Delta G$  is given by:

$$[EIC_D] = \frac{C}{1 + e^{-\Delta G/RT}} \quad (3)$$

$$[EIC_M] = C - [EIC_D] \quad (4)$$

where  $C$  is the total concentration of EIC in the NMR sample.

The spin-lock field for the  $^{15}\text{N}$ - $R_{1\rho}$  experiment was set to 1 kHz. Decay durations were set to 0, 240, 560, 880, 1280, 1600, 2080, and 2400 ms for  $^{15}\text{N}$ - $R_1$  and 0.2, 4.2, 7.2, 15, 23.4, 32.4, 42, 52.2, and 60 ms for  $^{15}\text{N}$ - $R_{1\rho}$ .  $R_1$  and  $R_{1\rho}$  values were determined by fitting time-dependent exponential decays of peak intensities at increasing relaxation delays.  $R_2$  values were extracted from the measured  $R_1$  and  $R_{1\rho}$  values.

**Enzymatic assay.** The PEP hydrolase activity of wt- and 3m-EIC was assayed by monitoring the disappearance of the alkene proton signals of PEP using real-time  $^1\text{H}$  NMR, as previously described (4). The reaction mixtures were prepared in 20 mM Tris buffer (pH 7.4), 100 mM NaCl, 4 mM  $\text{MgCl}_2$ , 1 mM EDTA, 2 mM DTT, 1 mM trimethylsilylpropanoic acid (TSP), and 99.99%  $\text{D}_2\text{O}$ . Enzyme concentration was 50  $\mu\text{M}$  for both wt- and 3m-EIC, unless stated otherwise.

Enzymatic assays were run in duplicate at 50 °C and 1 bar. The integrals of the signals measured for the alkene protons were converted to mM units by reference to the internal standard TSP. Integration of the NMR signals was performed using the software MNova (<https://mestrelab.com/download/mnova/>). Initial velocities were determined from the linear portion of the progress curves and were fit using the Michaelis–Menten equation.

Enzymatic activities reported in Figure 3B (main text) were measured at 65 °C and hydrostatic pressures of 1 and 3 kbar using the same protocol described above. The enzyme concentration was ~150  $\mu$ M.

**Analytical Ultracentrifugation.** Sedimentation velocity experiments were conducted at 50,000 rpm and 20 °C on a Beckman Coulter ProteomeLab XLI analytical ultracentrifuge following standard protocols (5). Samples of the  $^{15}$ N labeled wt-EIC and unlabeled 3m-EIC were studied at concentrations ranging from ~ 3 to 25  $\mu$ M in 100 mM NaCl, 20 mM Tris (pH 7.4), 2 mM DTT, and 4 mM  $\text{MgCl}_2$ . Samples were loaded in standard 12-mm, two-channel centerpiece cells, and data were collected using both the absorbance (280 nm) and Rayleigh interference (655 nm) optical detection systems. Time-corrected sedimentation data (6) were analyzed in SEDFIT 16.01c (7) in terms of a continuous  $c(s)$  distribution of sedimenting species with a resolution of 0.05 S and a maximum entropy regularization confidence level of 0.68. The solution density, solution viscosity, and protein partial specific volume were calculated in SEDNTERP (8) and corrected for isotopic labeling. Sedimentation coefficients  $s$  were corrected to standard conditions  $s_{20,w}$ .

**Molecular Dynamic simulations.** The X-ray structure of dimer EIC (PDB code: 2XZ7) was used as the starting structure for the simulation of wt-EIC. The 3m-EIC dimer was created by introducing the R400E, D440R and R559E mutations on both subunits of the dimer using the

PyMol/Mutagenesis tool. Three 700-ns Gaussian accelerated molecular dynamics (GaMD) simulation (9) of dimer wt-EIC, dimer 3m-EIC and monomer 3m-EIC (chain A of the 3m-EIC dimer) were performed in explicit solvent by using the Amber ff14SB force field (10) on GPU version of AMBER 16 (11).

The starting structure was centered in a truncated octahedron box and solvated with TIP3P water molecules (12) at least 10 Å away from the solute surface. Counter ions were added to neutralize the system. Each system was initially minimized for 10000 steps (50000 steepest descent then 50000 conjugate gradient) with the solute atoms fixed, and then another minimization was performed with all atoms relaxed. The system was slowly heated to 310K over 5 ns. Final system equilibration was achieved by a 5 ns of NVT and 5 ns of NPT to ensure that the simulated system had reached the appropriate density at 1 bar, following by a conventional MD (cMD) for 200 ns at 310 K. The GaMD module implemented in the GPU version of AMBER 16 was then applied to each system which included a 10 ns short cMD simulation used to collect the potential statistics for calculating GaMD acceleration parameters, a 50 ns equilibration after adding the boost potentially, and finally a GaMD production simulation with randomized initial atomic velocities. All GaMD simulations were run at the “dual-boost” level in which the total potential energies and the dihedral energies were boosted.

Periodic boundary conditions were applied for all of the simulation systems. Bonds containing hydrogen atoms were restrained with the SHAKE algorithm (13), and a 2 fs time step was used. Weak coupling to an external temperature and pressure bath was used to control both temperature and pressure (14). The electrostatic interactions were calculated using the PME (particle mesh Ewald summation) with a cutoff of 10.0 Å for long-range interactions (15). Data analysis was carried out using CPPTRAJ (16) and in-house scripts.

**Generation of structural ensembles.** To generate a structural ensemble representation of the monomeric and dimeric EIC tertiary fold, 700 ns aMD simulations were run in Amber 16 starting from the 3D structures of wt-EIC and 3m-EIC as described above. In the cases of dimeric wt-EIC and 3m-EIC, 1400-ns trajectories were created by appending the 700-ns trajectory of the second subunit to the 700-ns trajectory of the first subunit of the dimer. Each trajectory was clustered to produce representative structures of the aMD with a high degree of structural diversity. Each representative structure was energy minimized, and the ensemble of representative structures was used to fit the experimental RDC data as described previously (17). In brief, back-calculation of RDCs from conformational ensembles was done using the following equation:

$$RDC_i = \sum_k D_k \left[ (3 \cos^2 \theta - 1) + \frac{3}{2} (\sin^2 \theta \cos 2\phi) \right] \quad (5)$$

where  $\theta$  is the angle formed between the internuclear bond vector of the amide group of residue  $i$  and the  $z$  axis of the alignment tensor,  $\phi$  is the angle between the  $xy$  plane projection of the internuclear bond vector and the  $x$  axis, and  $D_k$  is the magnitude of the alignment tensor for ensemble member  $k$  multiplied by its fractional population in the ensemble.  $D_k$ ,  $\theta$  and  $\phi$  were optimized to reduce the discrepancy between experimental and back-calculated RDCs using the MATLAB script downloadable at <http://group.chem.iastate.edu/Venditti/downloads.html>.

The consistency between experimental and back-calculated RDC data was evaluated in terms of R-factor:

$$R - factor = \sum_i \sqrt{(RDC_i^{exp} - RDC_i^{calc})^2 / (2RDC_i^{exp2})} \quad (6)$$

where  $RDC_i^{exp}$  and  $RDC_i^{calc}$  are the experimental and back-calculated RDC for residue  $i$ , respectively. The protocol was iterated by increasing the number of clusters (and therefore the representative structures in the pool) until a stable R-factor was obtained.

## Supporting Figures

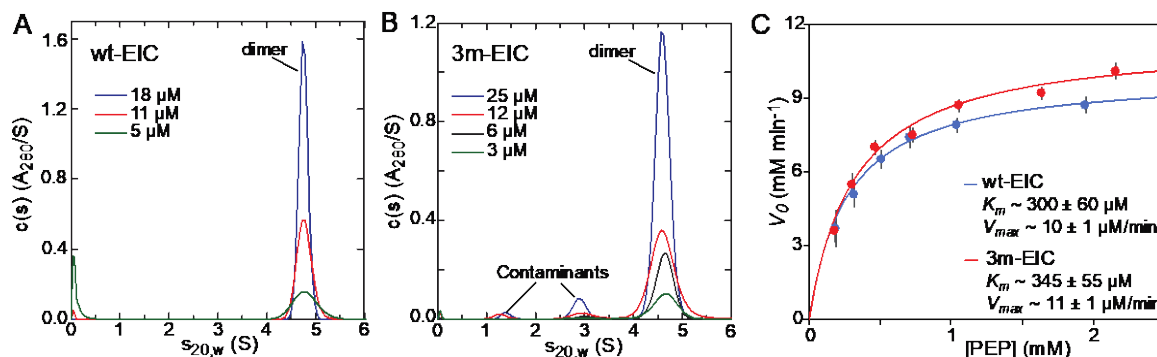


**Figure S1. 3m-EIC retains the oligomeric state and activity of wt-EIC at 1 bar.  $c(s)$**

distributions for (A)  $^{15}\text{N}$  wt-EIC and (B) 3m-EIC obtained at different loading concentrations (ranging from 25 to 3  $\mu\text{M}$ ) based on sedimentation velocity absorbance data collected at 50,000 revolutions per minute and 20  $^{\circ}\text{C}$  (see *SI Materials and Methods*). The sedimentation experiments indicate that wt-EIC and 3m-EIC are fully dimeric within the tested concentration range. Peaks at  $s_{20,w} < 4$  S do not show concentration dependent  $c(s)$  absorbance profiles (i.e. they do not report on the monomer–dimer equilibrium) and are attributed to small amounts of contaminants in the 3m-EIC AUC sample. (C) Michaelis-Menten kinetics obtained for the PEP hydrolysis reaction catalyzed by 50  $\mu\text{M}$  wt-EIC (blue circles) or 3m-EIC (red circles) at 50  $^{\circ}\text{C}$  and 1 bar. Modelling of the experimental data (solid curves) returns the Michaelis constant ( $K_m$ ) and maximum velocity ( $V_{max}$ ) of the enzymatic reaction.

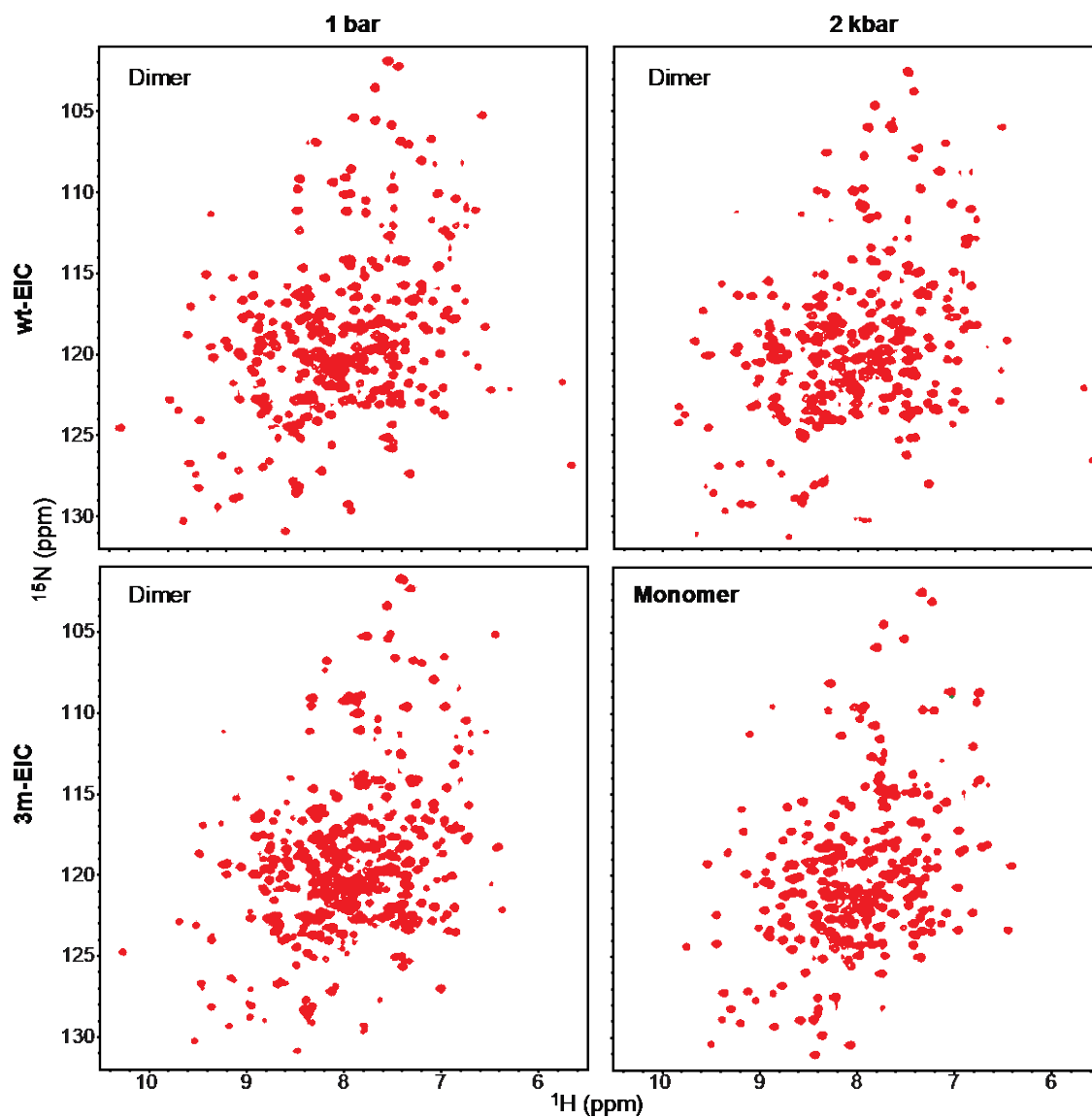


**Figure S2. A folded 3m-EIC monomer at 2 kbar.** 700 MHz  $^1\text{H}$ - $^{15}\text{N}$  TROSY spectra of  $^{15}\text{N}$ -labeled wt-EIC (top) and 3m-EIC (bottom) at 1bar (left) and 2 kbar (right).



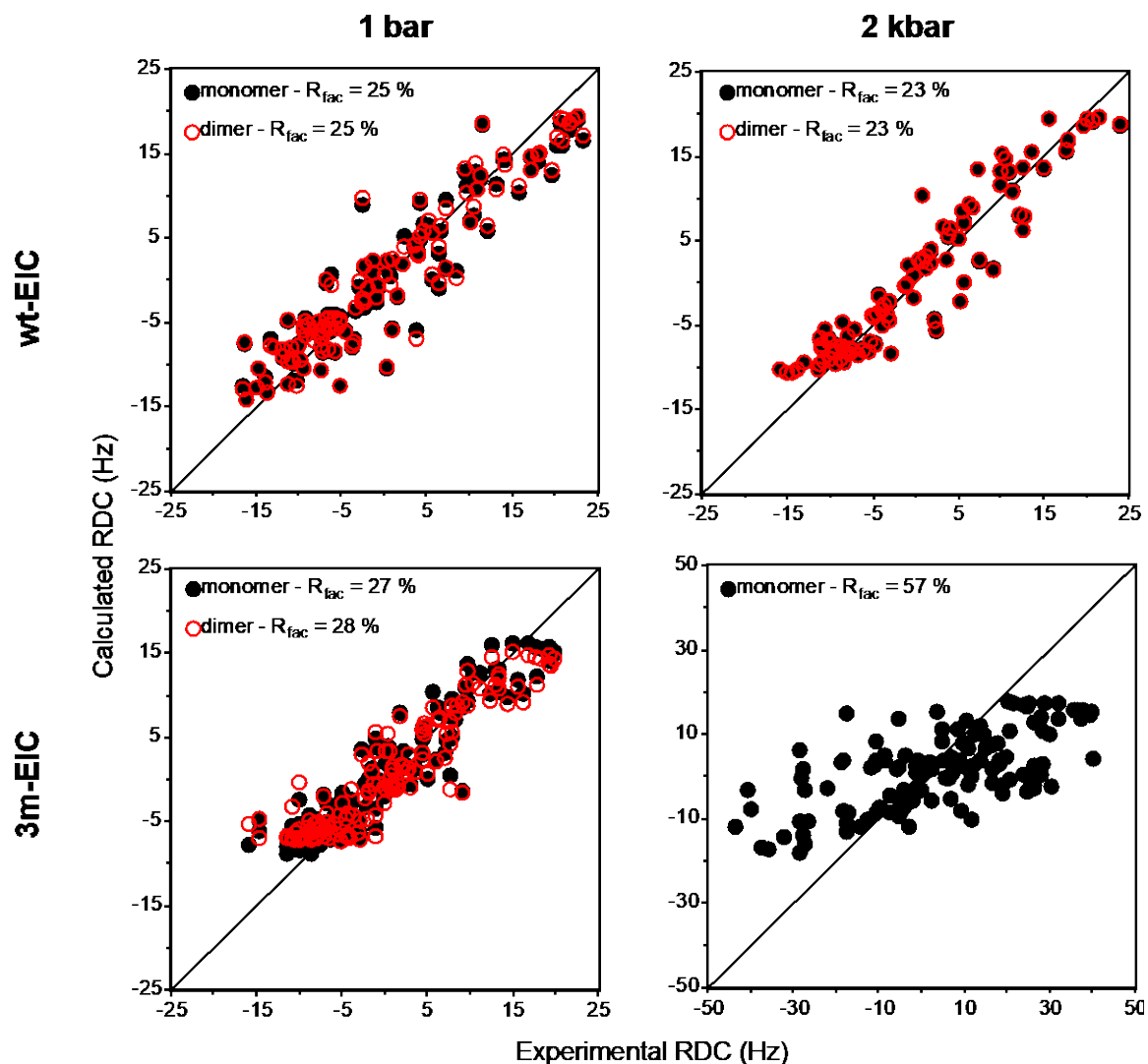


**Figure S3. The tertiary fold of 3m-EIC is affected by monomerization.** SVD fit of the experimental  $^1\text{D}_{\text{NH}}$  RDC data acquired for well-defined secondary structures of 3m-EIC (top) and wt-EIC (bottom) at 1 bar (left) and 2 kbar (right) to the coordinates of the X-ray structure of wt-EIC (PDB code: 2XZ7). Fits to a single subunit and to the full dimer are shown as filled black and open red circles, respectively. More details are reported in Table S2.

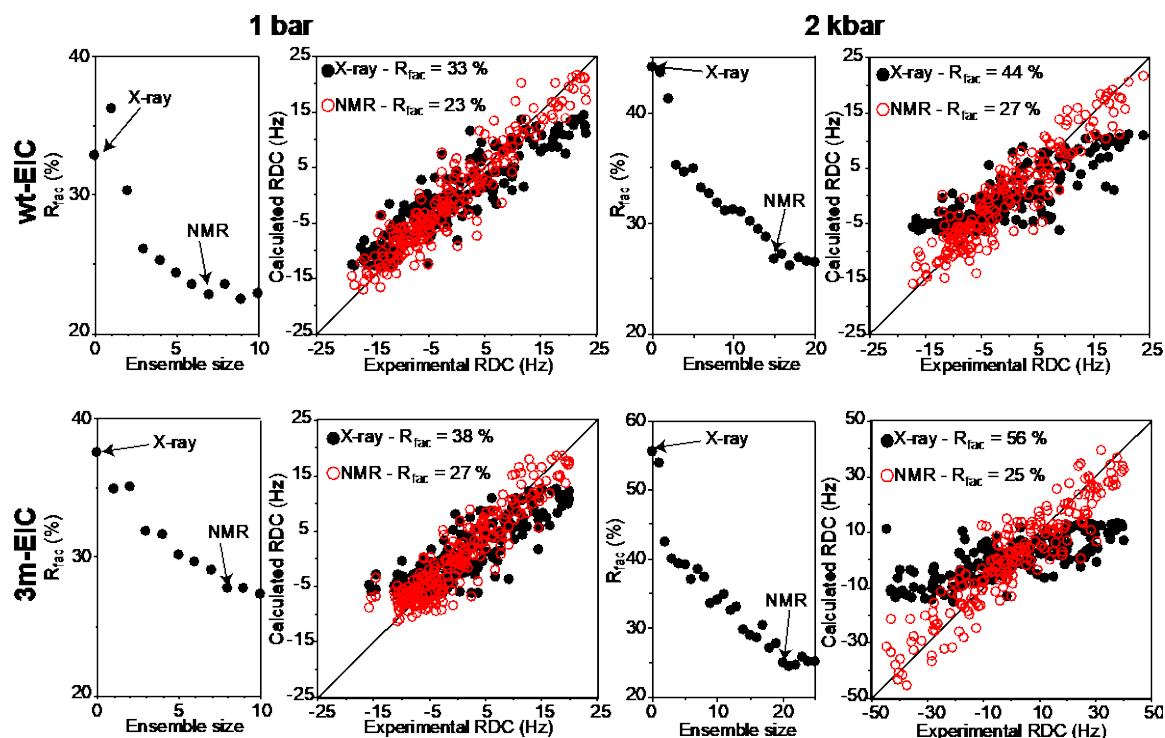


**Figure S4. Ensemble refinement results.** The results of the ensemble refinement are shown for wt-EIC (top) and 3m-EIC (bottom) at 1 bar (left) and 2 kbar (right). The plot of the R-factor versus ensemble size was used to determine the smallest ensemble size needed to obtain a stable R-factor. Ensemble sizes of 7, 15, 8 and 20 were needed to satisfy the solution NMR data for wt-EIC at 1bar, wt-EIC at 2 kbar, 3m-EIC at 1 bar and 3m-EIC at 2 kbar, respectively. The R-factor to the X-ray structure of wt-EIC is displayed at ensemble size = 0. The correlation between the experimental RDCs and the RDCs back-calculated from the best conformational ensemble (open red circles) or from the reference X-ray structure (filled black circles) is also shown. Note that all RDC data (including the ones from flexible loops) are included in these calculations. More details are reported in Table S2.

## Supporting Tables

**Table S1.** Thermodynamics of the 3m-EIC dimer-to-monomer equilibrium

	<b>3m-EIC</b>	<b>3m-EIC</b>	<b>3m-EIC</b>
	<b>3m-EIC</b>	<b>+ 20 mM <math>\alpha</math>KG</b>	<b>+ 20 mM PEP</b>
$\Delta G$ (kcal/mol)	$5.0 \pm 0.1$	$6.6 \pm 0.1$	$7.3 \pm 0.2$
$\Delta V$ (ml/mol)	$-153 \pm 2$	$-152 \pm 2$	$-146 \pm 3$
$K_d$ (M)	$9.10^{-11} \pm 2.10^{-13}$	$5.10^{-13} \pm 7.10^{-15}$	$6.10^{-14} \pm 3.10^{-15}$

**Table S2.** Backbone amide  $^1D_{NH}$  RDC analysis

<b>Used RDC</b>	<b>Number of RDCs</b>	<b><math>D_a^{NH}</math> (Hz)</b>	<b>Rhombicity</b>	<b>R-factor (%)</b>
<b>SVD fit to the X-ray structure (PDB code 2XZ7)</b>				
wt-EIC 1 bar (fit to monomer)	115	9.5	0.36	25
wt-EIC 1 bar (fit to dimer)	230	9.7	0.34	25
wt-EIC 2 kbar (fit to monomer)	95	9.8	0.12	23
wt-EIC 2 kbar (fit to dimer)	190	9.8	0.12	23
3m-EIC 1 bar (fit to monomer)	137	8.0	0.13	27
3m-EIC 1 bar (fit to dimer)	274	7.5	0.02	28
3m-EIC 2 kbar (fit to monomer)	129	9.9	0.51	57
<b>Ensemble refinement (only one subunit was considered)</b>				
wt-EIC 1 bar (fit to X-ray)	208	7.2	0.56	33
wt-EIC 1 bar (fit to ensemble)	208	ND	ND	23
wt-EIC 2 kbar (fit to X-ray)	190	5.6	0.15	44
wt-EIC 2 kbar (fit to ensemble)	190	ND	ND	27
3m-EIC 1 bar (fit to X-ray)	239	6.3	0.15	38
3m-EIC 1 bar (fit to ensemble)	239	ND	ND	27
3m-EIC 2 kbar (fit to X-ray)	196	7.8	0.44	56
3m-EIC 2 kbar (fit to ensemble)	196	ND	ND	25

### Supporting References

1. Delaglio F, *et al.* (1995) NMRPipe: A multidimensional spectral processing system based on UNIX pipes. *J Biomol NMR* 6(3):277-293.
2. Dotas RR & Venditti V (2019) Resonance assignment of the 128 kDa enzyme I dimer from *Thermoanaerobacter tengcongensis*. *Biomol NMR Assign* 13(2):287-293.
3. Clore GM & Gronenborn AM (1998) Determining the structures of large proteins and protein complexes by NMR. *Trends in Biotechnology* 16(1):22-34.
4. Dotas RR, *et al.* (2020) Hybrid Thermophilic/Mesophilic Enzymes Reveal a Role for Conformational Disorder in Regulation of Bacterial Enzyme I. *Journal of Molecular Biology* 432(16):4481-4498.
5. Zhao H, Brautigam CA, Ghirlando R, & Schuck P (2013) Overview of Current Methods in Sedimentation Velocity and Sedimentation Equilibrium Analytical Ultracentrifugation. *Current Protocols in Protein Science* 71(1):20.12.21-20.12.49.
6. Ghirlando R, *et al.* (2013) Improving the thermal, radial, and temporal accuracy of the analytical ultracentrifuge through external references. *Analytical Biochemistry* 440(1):81-95.
7. Schuck P (2000) Size-Distribution Analysis of Macromolecules by Sedimentation Velocity Ultracentrifugation and Lamm Equation Modeling. *Biophysical Journal* 78(3):1606-1619.
8. Cole JL, Lary JW, P Moody T, & Laue TM (2008) Analytical ultracentrifugation: sedimentation velocity and sedimentation equilibrium. *Methods Cell Biol* 84:143-179.
9. Miao Y, Feher VA, & McCammon JA (2015) Gaussian Accelerated Molecular Dynamics: Unconstrained Enhanced Sampling and Free Energy Calculation. *Journal of Chemical Theory and Computation* 11(8):3584-3595.
10. Maier JA, *et al.* (2015) ff14SB: Improving the Accuracy of Protein Side Chain and Backbone Parameters from ff99SB. *Journal of Chemical Theory and Computation* 11(8):3696-3713.
11. Case DA, *et al.* (2005) The Amber biomolecular simulation programs. *Journal of Computational Chemistry* 26(16):1668-1688.
12. Mark P & Nilsson L (2001) Structure and Dynamics of the TIP3P, SPC, and SPC/E Water Models at 298 K. *The Journal of Physical Chemistry A* 105(43):9954-9960.
13. Ryckaert J-P, Ciccotti G, & Berendsen HJC (1977) Numerical integration of the cartesian equations of motion of a system with constraints: molecular dynamics of n-alkanes. *Journal of Computational Physics* 23(3):327-341.

14. Berendsen HJC, Postma JPM, van Gunsteren WF, DiNola A, & Haak JR (1984) Molecular dynamics with coupling to an external bath. *The Journal of Chemical Physics* 81(8):3684-3690.
15. Essmann U, *et al.* (1995) A smooth particle mesh Ewald method. *The Journal of Chemical Physics* 103(19):8577-8593.
16. Roe DR & Cheatham TE (2013) PTRAJ and CPPTRAJ: Software for Processing and Analysis of Molecular Dynamics Trajectory Data. *Journal of Chemical Theory and Computation* 9(7):3084-3095.
17. Purslow JA, *et al.* (2018) Active Site Breathing of Human Alkbh5 Revealed by Solution NMR and Accelerated Molecular Dynamics. *Biophysical Journal* 115(10):1895-1905.

## CHAPTER 4. AN ALLOSTERIC POCKET FOR INHIBITION OF BACTERIAL ENZYME I IDENTIFIED BY NMR-BASED FRAGMENT SCREENING

Trang T. Nguyen<sup>1</sup> and Vincenzo Venditti<sup>1,2</sup>

<sup>1</sup> Department of Chemistry, Iowa State University, Ames, Iowa 50011, USA.

<sup>2</sup> Roy J. Carver Department of Biochemistry, Biophysics and Molecular Biology, Iowa State University, Ames, Iowa 50011, USA.

Modified from a manuscript published in *Journal of Structural Biology*

### Abstract

Enzyme I (EI), which is the key enzyme to activate the bacterial phosphotransferase system (PTS), plays an important role in the regulation of several metabolic pathways and controls the biology of bacterial cells at multiple levels. The conservation and ubiquity of EI among different types of Gram-positive and negative bacteria but not in eukaryotes has elected the enzyme as a potential target for antimicrobial research. Here, we use NMR-based fragment screening to identify novel inhibitors of EI. We identify three molecular fragments that allosterically inhibit the phosphoryl transfer reaction catalyzed by EI by interacting with the enzyme at a surface pocket located more than 10 Å away from the substrate binding site. Characterization of the structure and dynamics of the enzyme-inhibitor complexes reveals key interactions that perturb the fold of the active site and provides structural foundation for the inhibitory activity of the identified molecular fragments. We expect our results to provide the basis for the development of second generation allosteric inhibitors of increased potency and to suggest novel molecular strategies to combat drug-resistant infections.

### Introduction

The bacterial phosphoenolpyruvate (PEP):carbohydrate phosphotransferase system (PTS) is a signal transduction pathway that is involved in both transport and phosphorylation of a large

number of carbohydrates (PTS carbohydrates), in the movement of cells toward these carbon sources (chemotaxis), in biofilm formation, in the regulation of interactions between carbon and nitrogen metabolisms, and in the regulation of a number of other metabolic pathways, including catabolic gene expression, potassium transport, and inducer exclusion [1, 2]. For all these different regulatory processes, the signal is provided by the phosphorylation state of the PTS components [1], which varies according to the intracellular availability of PEP [3]. PEP acts as phosphoryl donor for enzyme I (EI), which, together with the phosphocarrier protein HPr and one of sugar-specific EI<sub>IA</sub> and EI<sub>IB</sub> pairs, forms a phosphorylation cascade that allows phosphorylation of the PTS carbohydrate bound to the membrane-spanning EI<sub>IC</sub> [4]. PTS-mediated regulatory mechanisms are based either on direct phosphorylation of the target protein by one of the PTS components or on phosphorylation-dependent interactions [1]. As such, the regulatory functions of PTS are strongly impaired by inhibition of EI phosphorylation by PEP. Indeed, an *Escherichia coli* strain engineered to not express EI only grows in complex media containing cyclic adenosine monophosphate (which is needed to activate catabolic gene expression in EI-deficient strains) [2], and the growth of wild-type *E. coli*, *Pseudomonas aeruginosa*, and *Staphylococcus aureus* on Luria-Bertani (LB) or Tryptic Soy broth is severely affected by addition of EI inhibitors designed in silico [5]. Moreover, a virulence study in a murine model has shown that EI-deficient strains of *Salmonella typhimurium*, *S. aureus*, and *Haemophilus influenzae* are 10 to 1,000 times less virulent than wild type bacteria [6], and PTS genes have been identified on several occasions in experimental screens for virulence factors [7-10]. Therefore, potent inhibitors of EI could show antimicrobial activity by attenuating both growth rate and virulence of the infective agent. Interestingly, EI is ubiquitous and one of the best-conserved proteins in both Gram-positive and Gram-negative bacteria, and does not share

any significant sequence similarity with eukaryotic proteins, making EI a possible target for development of wide-spectrum antimicrobials.

The functional form of EI is a 128 kDa symmetric dimer of identical subunits. Each subunit is composed of two structurally and functionally distinct domains separated by a long helical linker [11]. The N-terminal domain (EIN, residues 1-249) contains the phosphorylation site (H189) and the binding site for HPr (the second PTS protein). The C-terminal domain (EIC, residues 261-575) is responsible for EI dimerization and contains the binding site for PEP. Functional regulation of EI is achieved through synergistic coupling of multiple intra and interdomain conformational equilibria that are modulated by substrate and cofactor binding. Specifically, EI undergoes (i) a monomer-dimer equilibrium [12, 13], (ii) a compact-to-expanded equilibrium within the EIC domain [14, 15], (iii) a g<sup>+</sup>-to-g<sup>-</sup> equilibrium within the rotameric state of the H189 side chain [16], (iv) a state A-to-state B equilibrium within the EIN domain [17, 18], and (v) an open-to-close equilibrium describing a reorientation of EIN relative to EIC [15, 17-19]. PEP binding to EIC stabilizes the dimer/compact/g<sup>-</sup>/state B/closed form of EI and activates the enzyme for catalysis [12, 15]. Therefore, in addition to its pharmacological relevance, EI is also an important model system for biophysical investigations on long-range allosteric communication in multi-domain, oligomeric proteins.

Here, we use NMR-based fragment screening to identify novel strategies for selective inhibition of *E. coli* EI. Starting from a library of 1,000 molecular fragments, we identify three novel inhibitors of the enzyme (Figure 1) that bind the EIC domain at a surface pocket separated more than 10 Å from the active site. Interestingly, although the three allosteric inhibitors share the same binding pocket, investigation of the reaction kinetics indicates that they inhibit the enzyme using different mechanisms. Computational studies reveal that the intrinsic flexibility of



the inhibitors is chiefly responsible for their different mechanism of action, and provide hints as to how to evolve second generation inhibitors of increased potency. Such molecules will provide novel molecular tools to interrogate allosteric communication in EI and could potentially function as a new class of wide-spectrum antimicrobials.

## Results and Discussion

*Identification of small-molecule ligands of EI.* Novel small-molecule ligands of EI were identified by screening a rule-of-three-compliant library of 1,000 molecular fragments against EI by Saturation Transfer Difference (STD) and Chemical Shift Perturbation (CSP) NMR experiments [20]. In STD NMR, the target protein is mixed with one (or more) small molecule(s) and the transfer of saturation from the protein to the small molecule is investigated by solution NMR [21]. Ligand protons that are in close contact with the receptor protein receive a higher degree of saturation and generate stronger STD NMR signals. In contrast, protons that are not in contact with the target protein reveal no STD NMR signals. Therefore, STD NMR is an excellent tool to rapidly screen a small library of potential ligands against EI, as only ligands of the enzyme will return an STD NMR signal (Figure 2a). To reduce the experimental time for STD screening, fragments were screened in pools of five, corresponding to a total of 200 NMR samples. Pools were ranked by their signal intensities, which were calculated as the sum of the intensity of the STD spectrum over the entire spectral width (Figure 2b). The 25 pools returning the strongest STD signals were counterscreened against the enzyme by CSP experiments. These protein-detected NMR experiments are orthogonal to the ligand-detected STD experiments, and provide an independent validation for the ligand-protein interactions revealed by STD screening [22]. CSP-based screening consists in measuring  $^1\text{H}$ - $^{15}\text{N}$  heteronuclear single quantum coherence (HSQC) spectra of the target protein in the absence and in the presence of the molecular fragment pool. Pools containing one (or more) ligand(s) of the receptor protein

generate shifts of the NMR signals that are easily observable by overlaying the measured HSQC spectra (Figure 2c) [23]. To facilitate acquisition and analysis of the NMR data, CSP experiments were measured on  $^{15}\text{N}$ -labeled samples of the isolated N- (EIN) and C-terminal (EIC) domains of EI that, being considerably smaller than the full-length protein, generate highly resolved NMR spectra characterized by high signal-to-noise ratio. In total, 30 EI ligands were identified from 20 fragment pools selected by our combined STD/CSP screening. The EI ligands were recognized from the other molecules comprising the fragment pools by comparing the pattern of the STD-NMR signals with reference  $^1\text{H}$  NMR spectra provided by the commercial supplier of the fragment library.

The affinity of the newly discovered EI ligands was investigated by acquiring CSP-based, NMR titration experiments on  $^{15}\text{N}$ -labeled EIN or EIC at increasing concentration of small molecule [24]. The data were fit using a standard equilibrium dissociation equation [25] to obtain the equilibrium dissociation constant ( $K_D$ ) per each analyzed complex (Figure 2d). This analysis identified six small molecules that bind the EIC domain of EI with low mM affinity (Figure 2e).

*Identification of small-molecule inhibitors of EI.* The six small-molecule ligands of EI identified above (compounds 1-6 in Figure 2e) were characterized for their ability to inhibit the phosphoryl-transfer reaction from PEP to HPr catalyzed by the enzyme. The activity of full-length EI was assayed in the presence of 0.0, 1.5, and 6.0 mM of compounds 1-6 by  $^1\text{H}$ - $^{15}\text{N}$  SOFAST NMR experiments [12], and results are reported in Figure 3a as Lineweaver–Burk plots. In such graphs, the y and x intercepts are equivalent to the inverse of the maximum velocity ( $1/V_{\text{max}}$ ) and the negative inverse of the Michaelis constant ( $-1/K_m$ ), respectively. We observed that only compounds 1-3 are inhibitors of EI. In particular, compounds 1 and 2 act as competitive inhibitors (i.e. their presence increases the  $K_m$  for PEP binding to EI, Figure 3a),

while compound 3 acts as mixed inhibitor of EI (i.e. its presence increases  $K_m$  and decreases  $V_{max}$  for the enzymatic reaction, Figure 3a).

The enzyme kinetic data were modelled using a competitive inhibition model (equation 3) for compounds 1 and 2, and a mixed inhibition model (equation 4) for compound 3. Modelling was performed by keeping  $K_{m,0}$  (the value of  $K_m$  in the absence of inhibitor) to its literature value (350  $\mu M$ ) and the  $K_i$ 's for compounds 1-3 to the corresponding  $K_D$ 's measured by NMR titration experiments (2.5, 2.6, and 3.2 mM for compound 1, 2, and 3, respectively - Figure 2e).  $V_{max,0}$  (the value of  $V_{max}$  in the absence of inhibitor) and  $K_{I,S}$  (the dissociation constant for inhibitor binding to the enzyme substrate complex that is used by the mixed inhibition model – see equation 4) were optimized to maximize the agreement between experimental and simulated data (Figure 3b). Best fit  $V_{max,0}$  and  $K_{I,S}$  values of  $19 \pm 2 \mu M \text{ min}^{-1}$  and  $5.0 \pm 0.5 \text{ mM}$  were obtained, respectively.

*Structural basis for inhibition of EI.* To gain structural insight into the interaction between EI and compounds 1-3, the combined  $^1H/^{15}N$  CSP ( $\Delta H/N$ ) generated by 8 mM inhibitor on the  $^1H$ - $^{15}N$  HSQC spectrum of isolated EIC are plotted on the enzyme structure in Figure 4. NMR chemical shifts depend on the local electronic environment at the observed nuclei. Therefore, CSP data report on local changes of the electronic structure due to the presence of the ligand or to protein conformational changes occurring upon ligand binding. Figure 4 displays that compounds 1-3 generate large  $\Delta H/N$  values at a small pocket formed by the C-terminal ends of  $\alpha$ -helix 1 (residues 268-278) and 2 (residues 310-325) of the EIC domain, suggesting that the three molecules share the same binding site. Interestingly, this surface pocket is located  $> 10 \text{ \AA}$  away from the binding site for PEP (Figure 4), indicating that compounds 1-3 perturb the affinity of the EI-PEP complex (Figure 3) in an allosteric manner. Of note, compound

3 generates additional CSP at the N-terminal end of the EIC domain and at the  $\beta 3\alpha 3$  loop of the active site (Figure 4). This observation suggests that compound 3 induces conformational changes at the active site of EI that might be responsible for the ability of compound 3 to reduce the  $V_{max}$  for the phosphoryl-transfer reaction (Figure 3).

Atomic-resolution structural models for the complexes formed by EIC with compounds 1-3 were constructed by molecular docking of one copy of the ligand into the binding pocket defined by CSP data (i.e. the surface pocket defined by the C-terminal ends of  $\alpha$ -helix 1 and 2, Figure 4a). Calculations were run with AutoDock as described in Methods, and the resulting structures are displayed in Figure 4. As expected from the close similarity of the chemical structures of the three ligands (Figure 2e), compounds 1-3 adopt a similar binding mode on EIC. Indeed, for all ligands, the hydrophobic aromatic ring dives into the hydrophobic pocket formed by  $\alpha$ -helices 1 and 2, while hydrophilic groups remain solvent exposed. Of note, all small molecules make close contacts with the side chain of V292, which is located at the N-terminal end of  $\beta$ -strand 2 (residues 292-296). As  $\beta$ -strand 2 is responsible for two key interactions that stabilize binding of PEP to EIC (namely: an hydrophobic contact between the L294 side-chain and the CH<sub>2</sub> group of PEP, and a salt-bridge between the side chain of R296 and the phosphate group of PEP) [14, 26], these contacts between the inhibitors and V292 are most likely responsible for the effects of compounds 1-3 on the KM of the EIC-PEP complex. Significant differences in the way compounds 1-3 bind the enzyme are observed at the level of  $\alpha$ -helix 2. Indeed, while compounds 1 and 2 make minimal contacts with the C-terminal end of  $\alpha$ -helix 2, the presence of the sp<sup>3</sup> C bridging the two aromatic groups of compound 3 allows this inhibitor to bend and form extensive contacts with S326 and Q327 (Figure 4). As this helix is directly connected to the protein active site via the  $\beta 2\alpha 2$  loop (which directly contacts the active site

$\beta 3\alpha 3$  loop), we hypothesize that the interactions established by compound 3 with S326 and Q327 perturb the structure of the active-site and are, therefore, responsible for the effect of this inhibitor on  $V_{\max}$ .

The structural basis for the mixed inhibition of EI caused by compound 3 has been investigated further by means of Molecular Dynamics (MD) simulations. In particular, 400-ns long MD simulations were run by using the docking EIC-inhibitor complexes as the starting structures. EIC was simulated in its physiological, dimeric form [12-14] with inhibitors bound to both subunits. Stability of the simulations was evaluated by plotting the heavy-atom root mean square deviation (r.m.s.d.) from the starting structure versus time (Figure 5a-c). Analysis of these plots highlights the greater rigidity of compound 2 compared to compounds 1 and 3, which show recurrent transitions to alternative rotameric structures (note the sharp transitions in r.m.s.d. versus time observed for compounds 1 and 3 in the MD simulations). Despite this intrinsic flexibility, the hydrophilic ring of compound 3 contacts the C-terminal end of  $\alpha$ -helix 2 for the entire 400-ns trajectory, as evidenced by the fact that the hydrogen-bond between the hydroxyl group of S296 and the amine group of the inhibitor persists for the majority of the MD simulation (Figure 5d).

To analyze if EIC undergoes different dynamics when bound to the three small molecule inhibitors, we performed a ‘combined’ principal component analysis (PCA) on the simulated trajectories [27]. In this method, two or more trajectories (fitted on the same reference structure) are concatenated, and a covariance matrix is constructed and diagonalized to obtain a common set of eigenvectors, describing the variance of the atomic coordinates in the combined MD simulation, and eigenvalues, describing the extent of the atomic fluctuations in the corresponding eigenvectors. When PCA is performed on a concatenated trajectory and eigenvectors are ordered

by decreasing eigenvalue, significant differences in the structure and dynamics of the simulated systems (in our case the three EIC-inhibitor complexes) are described by the first few eigenvectors [27]. In the particular case of EIC, we have created three 800-ns trajectories (one per each EIC-inhibitor complex) by appending the 400-ns trajectory of the second subunit to the 400-ns trajectory of the first subunit of the EIC dimer. These three 800-ns trajectories were concatenated together and investigated by combined PCA performed on the coordinates of C $\alpha$  atoms of EIC. Once a common set of PC's are obtained, the separate 800-ns trajectories are projected onto the resulting eigenvectors, and the properties of these projections are compared for all simulations. In particular, there are two main quantities of interest: the average projection and the root mean square fluctuation (r.m.s.f.) in the projection. Differences in the average projection on a particular eigenvector indicate that the simulations have different average displacement (i.e. average structure) in that PC. In contrast, r.m.s.f. differences in a particular eigenvector indicate that the simulations have different dynamics in the collective motion described by that PC. Analysis of the first 10 PC's indicates that the simulated EIC-inhibitor complexes have similar molecular dynamics (i.e. similar r.m.s.f. versus eigenvector plots) but different equilibrium structures (Figure 6a). In particular, structural changes are described by the first four PC's, in which EIC bound to compound 3 has average projections considerably different from the ones of EIC bound to compounds 1 and 2 (Figure 6a). The collective motions described by the first four PC's are displayed in Figure 6b by superimposing the start and the end frames of the pseudo-trajectory describing each eigenvector. A pseudo-trajectory with a negative average displacement has an equilibrium structure shifted toward the start point of the concerted motion, while a positive average displacement indicates that the average structure of the pseudo-trajectory is shifted toward the end point of the concerted motion. Inspection of Figure 6 reveals

that the first four PC's describe collective motions involving the C-terminal helix and the active site  $\beta 2\alpha 2$ ,  $\beta 3\alpha 3$ , and  $\beta 6\alpha 6$  loops of EIC. In particular, the active site  $\beta 3\alpha 3$  loop undergoes a closed-to-open (start-to-end) conformational equilibrium on PC's 1 and 4, with compounds 1 and 2 favoring the closed conformation (note that the average projections of the simulations with compounds 1 and 2 on PC's 1-4 are negative) and compound 3 favoring the open conformation (note that the average projections of the simulation with molecule 3 on PC's 1-4 are positive). As the  $\beta 3\alpha 3$  loop of EIC has to adopt a fully closed configuration for efficient EI catalysis [28], we ascribe the mixed inhibitor behavior of compound 3 to its ability to destabilize the catalytically-competent, fully closed conformation of the  $\beta 3\alpha 3$  loop.

### Conclusion

EI is emerging as an important model system to study allosteric regulation in multidomain, oligomeric enzymes, and as a promising pharmaceutical target for antimicrobial design. In this contribution, we have characterized a novel surface pocket localized on the EIC domain that is allosterically coupled to the enzyme active site. By using NMR-based fragment screening, we identify three small molecules (referred to as compounds 1, 2, and 3) that bind to the allosteric pocket and inhibit the phosphoryl-transfer activity of EI. Interestingly, the  $K_D$  values measured for the three EIC-inhibitor complexes ( $\sim 3$  mM) are comparable to the equilibrium dissociation constant reported for the EIC interaction with  $\alpha$ -ketoglutarate ( $\sim 2$  mM) [26], a metabolite that acts simultaneously as a competitive inhibitor and an allosteric stimulator of the enzyme [12], and that was shown to regulate the activity of EI in vivo [12, 29]. Therefore, the inhibitors identified here can be used as chemical probes to investigate long-range communication in EI.

On the other hand, testing the druggability of the allosteric pocket identified here for antimicrobial applications will require evolution of compounds 1-3 into second generation inhibitors of increased potency. In this respect, several hints for the development of second generation allosteric inhibitors can be inferred from the computational studies on the EIC-inhibitor complexes summarized in Results and discussion. Importantly, the presence within the inhibitor of a hydrophobic, six-membered aromatic ring and a more hydrophilic moiety seems crucial for orienting the molecule inside the aromatic pocket. In particular, it is imperative that the inhibitor penetrates deep enough into the pocket to form contacts with V292, which allosterically alter the properties of the PEP binding site and reduce the affinity of EI for its substrate. In addition, we notice that formation of contacts between the inhibitor and the C-terminal end of  $\alpha$ -helix 2 allosterically perturbs the structure of the active site at the  $\beta 3\alpha 3$  loop. As the  $\beta 3\alpha 3$  loop is directly involved in stabilization of the catalytic transition state [28], this structural rearrangement negatively affects the efficiency of the enzyme by reducing its turnover number. Our docking and MD results suggest that introducing a flexible element between the hydrophobic and hydrophilic moieties of the inhibitor (such as, for example, the  $sp^3$  C in compound 3) favors formation of extensive contacts with  $\alpha$ -helix 2 by allowing the small molecule to adopt a bent conformation. In alternative, branched molecules could be designed starting from compounds 1 and 2 to increase their interactions with the C-terminal end of  $\alpha$ -helix 2 and confer mixed inhibitor character to these second generation compounds. Finally, in silico screening campaigns targeting the allosteric site at the C-terminal end of  $\alpha$ -helices 1 and 2 of EIC might provide additional clues toward evolution of compounds 1-3 and/or suggest novel lead compounds for inhibition of EI. As the allosteric pocket identified here is conserved across EI from different bacterial strains (including important drug-resistant organisms) (Figure 7), the



results and strategies presented in this work may inspire new, much needed, molecular routes to inhibition of bacterial infections.

## Materials and Methods

*Protein expression and purification.* E.coli EI and uniformly  $^{15}\text{N}$ -labelled EIC, EIN, and HPr were expressed and purified as previously described [12, 14, 16].

*Fragment preparation.* A commercial library of 1,000 molecular fragments was purchased from ChemBridge. The library was designed to meet the “rule of three” for fragment-based screening (i.e., molecular weight less than 300 Da, number of hydrogen bond donors and acceptors does not exceed 3, and cLogP value less than 3) [30]. To speed up the screening procedure, the 1,000 fragments were pooled in groups of 5. The composition of each pool was optimized to reduce the risk of overlap among the  $^1\text{H}$  NMR signals of the molecular fragments. Stock solutions were prepared by dissolving each pool in DMSO- $d_6$  so that each fragment is at final concentration of 2.5 mM.

*NMR spectroscopy.* All spectra were acquired on Bruker 800 MHz spectrometers equipped with a z-shielded gradient triple resonance cryoprobe.  $^1\text{H}$ - $^{15}\text{N}$  HSQC spectra of free EIN, EIC, and HPr were assigned according to previously reported NMR chemical shifts [14, 31, 32]. NMR samples for STD screening were prepared in 20 mM phosphate buffer (pH 7.8), 100 mM NaCl, 4 mM  $\text{MgCl}_2$ , and 99.9%  $\text{D}_2\text{O}$ . The protein concentration was 10  $\mu\text{M}$ . A total of 200 NMR samples were prepared by adding 40  $\mu\text{L}$  of fragment pool stock solution (prepared as described above) directly into the 500  $\mu\text{L}$  (final volume) NMR sample (note that the final concentration of each fragment in the NMR sample was 200  $\mu\text{M}$ ). The  $^1\text{H}$  STD spectra were measured at 37  $^\circ\text{C}$  by applying a selective saturation field for 400 ms at 20 and 0.9 ppm for the off-resonance and the on-resonance experiment, respectively. Acquisition was automated by

using an autosampler. Spectra were processed and analyzed by using MestReNova 14 (<https://mestrelab.com/software/mnova/>).

CSP screening experiments were run at 37 °C in 20 mM Tris (pH 7.4), 100 mM NaCl, 4 mM MgCl<sub>2</sub>, 2 mM DTT, and 5 % D<sub>2</sub>O. The protein concentration was 400 µM. A total of 40 µL of fragment pool stock solution were added to the 500 µL NMR sample.

NMR titration experiments were measured at 37 °C in 20 mM Tris (pH 7.4), 100 mM NaCl, 4 mM MgCl<sub>2</sub>, 2 mM DTT, and 5 % D<sub>2</sub>O. The protein concentration was 400 µM and the concentration of small molecule was varied between 0 and 8 mM. Spectra were processed using NMRPipe [33] and analyzed using the program SPARKY (<http://www.cgl.ucsf.edu/home/sparky>). Assignment of the <sup>1</sup>H-<sup>15</sup>N cross-peaks for the EIC-small molecule complexes was performed by titration experiments, following the change in <sup>1</sup>H-<sup>15</sup>N cross-peak positions as a function of added small molecule. Weighted combined <sup>1</sup>H/<sup>15</sup>N chemical shift perturbations ( $\Delta_{H/N}$ ) resulting from the addition of increasing concentrations of small molecule were calculated using the following equation [34]:

$$\Delta_{H/N} = \sqrt{(\Delta\delta_H W_H)^2 + (\Delta\delta_N W_N)^2} \quad (1)$$

where  $W_H (= 1)$  and  $W_N (= 0.154)$  are weighting factor for the <sup>1</sup>H and <sup>15</sup>N amide shifts, respectively.  $\Delta\delta_H$  and  $\Delta\delta_N$  are the <sup>1</sup>H and <sup>15</sup>N chemical shift differences in ppm, respectively, between free and bound states. The equilibrium dissociation constants ( $K_D$ ) for the EIC-inhibitor complexes were obtained by fitting the changes in  $\Delta_{H/N}$  with increasing concentration of small molecule using the equation [25]:

$$\Delta_{H/N} = \Delta_0 \frac{P+L+K_D - \sqrt{(P+L+K_D)^2 - 4PL}}{2P} \quad (2)$$

where  $\Delta 0$  is the weighted combined  $^1\text{H}/^{15}\text{N}$  chemical shift at saturation, and P and L are the protein and small molecule concentrations, respectively.

*Enzymatic assay.* Enzyme kinetic assay we run by measuring the rate of phosphoryl transfer from PEP to HPr catalyzed by full-length EI by using  $^1\text{H}$ - $^{15}\text{N}$  SOFAST NMR spectra as described previously [12]. Reaction were run at 25 °C in 20 mM Tris (pH 7.4), 100 mM NaCl, 4 mM  $\text{MgCl}_2$ , 2 mM DTT, and 5 %  $\text{D}_2\text{O}$ . The assay was performed in triplicate. The enzyme kinetic data measured at different concentration of inhibitor were fit using a complete or mixed inhibition model:

$$\text{Competitive inhibition - } v_0 = \frac{V_{max,0}[\text{PEP}]}{K_{m,0}\left(1 + \frac{[\text{I}]}{K_I}\right) + [\text{PEP}]} \quad (3)$$

$$\text{Mixed inhibition - } v_0 = \frac{V_{max,0}[\text{PEP}]}{K_{m,0}\left(1 + \frac{[\text{I}]}{K_I}\right) + [\text{PEP}]\left(1 + \frac{[\text{I}]}{K_{I,S}}\right)} \quad (4)$$

where  $v_0$  is the initial velocity of the enzymatic reaction,  $[\text{PEP}]$  and  $[\text{I}]$  are the concentration of substrate and inhibitor, respectively,  $K_I$  is the equilibrium dissociation constant for the enzyme-inhibitor complex,  $K_{I,S}$  is the dissociation constant for the interaction between the inhibitor and the enzyme-PEP complex, and  $K_{m,0}$  and  $V_{max,0}$  are the Michaelis constant and maximum velocity in the absence of inhibitors, respectively. The seven measured datasets (in the absence of inhibitor, and in the presence of two concentrations of each inhibitor) were fit globally. In the global fitting procedures  $K_I$  and  $K_{m,0}$  values were kept fixed to their measured values.  $K_{I,S}$  for compound 3 and  $V_{max,0}$  were optimized to maximize the agreement between experimental and simulated data.

*Molecular docking simulations.* Molecular docking simulations were run using the coordinates of the EIC domain from the crystallographic structure of the full-length E. coli EI (PDB: 2HWG) as the target. Before the actual docking run, the protein structure was energy

minimized by 1000 steps of steep descended followed by 1000 steps of conjugated gradient algorithm. Energy minimization was performed using the Amber 16 simulation package [35] and the Amber ff14SB force field [36]. The structures of compounds 1-3 were docked into the protein using AutoDockTools 1.5.4 and Autodock 4.2 [37]. A cubic grid box (grid spacing = 0.373 Å;  $40 \times 40 \times 40$  grid points) was placed at the C-terminal ends of  $\alpha$ -helix 1 and 2 of EIC. Docking was performed using the Lamarckian genetic algorithm (LGA) and allowing the side chains of E285 and N327 conformational flexibility during the simulations. For the small molecules, the 5 and 6-membered aromatic rings were considered rigid, while all other bonds were treated as rotatable. Most of docking parameters were kept as default, with the exception of the population size (set to 150 with 2,500,000 evaluations) and the maximum number of generations (set to 27,000). Cluster analysis was performed with a r.m.s.d. tolerance of 2 Å. The best conformation is considered to be the conformation with the lowest free energy of binding.

Molecular Dynamics simulations. The structures of the EIC-inhibitor complexes obtained by molecular docking simulations were used as the starting point for 400 ns MD simulations ran using the Amber 16 package [35] and the Amber ff14SB force field [36]. EIC was simulated in its dimer form with inhibitors bound to both subunits. The small molecules were parameterized with the AM1-BCC charge model [38] and the GAFF force field [39]. The initial complex was centered in a truncated octahedron, filled with TIP3P water model [40] and neutralizing ions, and the distance between the protein atoms and the boundaries was set to 10 Å. Energy minimization of the initial structures, including 1000 steps of steepest descent and 1000 steps of conjugate gradient, was performed in 3 stages. First, ions and water positions were relaxed. Then, the EIC-inhibitor complex was allowed to relax. Finally, the full system was energy minimized. The system was equilibrated with a 1 ns run in which the temperature was gradually raised from 0 to

310 K, followed by a 5 ns run in which the temperature was held constant at 310 K. The equilibrated system was simulated for 400 ns by keeping the temperature (310 K) and pressure (1 atm) constant. Periodic boundary conditions were applied, and bonds were restrained with the SHAKE algorithm [41]. An integration step of 2 fs was used. Weak coupling to an external pressure and temperature bath was used [42]. Particle-Mesh Ewald summation with a cutoff of 10 Å for long-range interactions was used to treat electrostatic interactions [43].

Analysis of the MD trajectories was performed in Amber 16 using the CPPTRAJ tool [44]. CPPTRAJ was also employed for combined PCA analysis [27]. Analysis was performed on the C $\alpha$  atoms using the protocol described at <https://amberhub.chpc.utah.edu/introduction-to-principal-component-analysis/>.

### Acknowledgement

We thank Drs. Davit Potoyan and Julien Roche for critical reading of the manuscript.

### References

- [1] Deutscher J, Ake FM, Derkaoui M, Zebre AC, Cao TN, Bouraoui H, et al. The bacterial phosphoenolpyruvate:carbohydrate phosphotransferase system: regulation by protein phosphorylation and phosphorylation-dependent protein-protein interactions. *Microbiol Mol Biol Rev.* 2014;78:231-56.
- [2] Postma PW, Lengeler JW, Jacobson GR. Phosphoenolpyruvate:Carbohydrate Phosphotransferase Systems. In: Neidhardt FC, Lin EC, Curtiss R, editors. *Escherichia coli and Salmonella: Cellular and Molecular Biology* 1996. p. 1149-74.
- [3] Hogema BM, Arents JC, Bader R, Eijkemans K, Yoshida H, Takahashi H, et al. Inducer exclusion in *Escherichia coli* by non-PTS substrates: the role of the PEP to pyruvate ratio in determining the phosphorylation state of enzyme IIAGlc. *Mol Microbiol.* 1998;30:487-98.
- [4] Clore GM, Venditti V. Structure, dynamics and biophysics of the cytoplasmic protein-protein complexes of the bacterial phosphoenolpyruvate: sugar phosphotransferase system. *Trends Biochem Sci.* 2013;38:515-30.
- [5] Huang KJ, Lin SH, Lin MR, Ku H, Szkaradek N, Marona H, et al. Xanthone derivatives could be potential antibiotics: virtual screening for the inhibitors of enzyme I of bacterial phosphoenolpyruvate-dependent phosphotransferase system. *J Antibiot.* 2013;66:453-8.

- [6] Kok M, Bron G, Erni B, Mukhija S. Effect of enzyme I of the bacterial phosphoenolpyruvate : sugar phosphotransferase system (PTS) on virulence in a murine model. *Microbiology*. 2003;149:2645-52.
- [7] Edelstein PH, Edelstein MA, Higa F, Falkow S. Discovery of virulence genes of *Legionella pneumophila* by using signature tagged mutagenesis in a guinea pig pneumonia model. *Proc Natl Acad Sci U S A*. 1999;96:8190-5.
- [8] Hava DL, Camilli A. Large-scale identification of serotype 4 *Streptococcus pneumoniae* virulence factors. *Mol Microbiol*. 2002;45:1389-406.
- [9] Jones AL, Knoll KM, Rubens CE. Identification of *Streptococcus agalactiae* virulence genes in the neonatal rat sepsis model using signature-tagged mutagenesis. *Mol Microbiol*. 2000;37:1444-55.
- [10] Lau GW, Haataja S, Lonetto M, Kensit SE, Marra A, Bryant AP, et al. A functional genomic analysis of type 3 *Streptococcus pneumoniae* virulence. *Mol Microbiol*. 2001;40:555-71.
- [11] Chauvin F, Brand L, Roseman S. Enzyme I: the first protein and potential regulator of the bacterial phosphoenolpyruvate: glycolate phosphotransferase system. *Res Microbiol*. 1996;147:471-9.
- [12] Nguyen TT, Ghirlando R, Venditti V. The oligomerization state of bacterial enzyme I (EI) determines EI's allosteric stimulation or competitive inhibition by alpha-ketoglutarate. *J Biol Chem*. 2018;293: 2631-9.
- [13] Patel HV, Vyas KA, Savtchenko R, Roseman S. The monomer/dimer transition of enzyme I of the *Escherichia coli* phosphotransferase system. *J Biol Chem*. 2006;281:17570-8.
- [14] Venditti V, Clore GM. Conformational selection and substrate binding regulate the monomer/dimer equilibrium of the C-terminal domain of *Escherichia coli* enzyme I. *J Biol Chem*. 2012;287:26989-98.
- [15] Venditti V, Tugarinov V, Schwieters CD, Grishaev A, Clore GM. Large interdomain rearrangement triggered by suppression of micro- to millisecond dynamics in bacterial Enzyme I. *Nat Commun*. 2015;6:5960.
- [16] Suh JY, Cai M, Clore GM. Impact of phosphorylation on structure and thermodynamics of the interaction between the N-terminal domain of enzyme I and the histidine phosphocarrier protein of the bacterial phosphotransferase system. *J Biol Chem*. 2008;283:18980-9.
- [17] Schwieters CD, Suh JY, Grishaev A, Ghirlando R, Takayama Y, Clore GM. Solution structure of the 128 kDa enzyme I dimer from *Escherichia coli* and its 146 kDa complex with HPr using residual dipolar couplings and small- and wide-angle X-ray scattering. *J Am Chem Soc*. 2010;132:13026-45.

- [18] Teplyakov A, Lim K, Zhu PP, Kapadia G, Chen CC, Schwartz J, et al. Structure of phosphorylated enzyme I, the phosphoenolpyruvate:sugar phosphotransferase system sugar translocation signal protein. *Proc Natl Acad Sci U S A*. 2006;103:16218-23.
- [19] Venditti V, Schwieters CD, Grishaev A, Clore GM. Dynamic equilibrium between closed and partially closed states of the bacterial Enzyme I unveiled by solution NMR and X-ray scattering. *Proc Natl Acad Sci U S A*. 2015;112:11565-70.
- [20] Carr RA, Congreve M, Murray CW, Rees DC. Fragment-based lead discovery: leads by design. *Drug Discov Today*. 2005;10:987-92.
- [21] Mayer M, Meyer B. Group epitope mapping by saturation transfer difference NMR to identify segments of a ligand in direct contact with a protein receptor. *J Am Chem Soc*. 2001;123:6108-17.
- [22] Ma R, Wang P, Wu J, Ruan K. Process of Fragment-Based Lead Discovery-A Perspective from NMR. *Molecules*. 2016;21.
- [23] Purslow JA, Khatiwada B, Bayro MJ, Venditti V. NMR Methods for Structural Characterization of Protein-Protein Complexes. *Front Mol Biosci* 2020;7:9.
- [24] Fielding L. NMR methods for the determination of protein-ligand dissociation constants. *Prog Nucl Magn Reson Spectrosc*. 2007;51:2190242.
- [25] Granot J. Determination of dissociation constants of 1:1 complexes from NMR data. Optimization of the experimental setup by statistical analysis of simulated experiments. *J Magn Reson*. 1983;55:216-24.
- [26] Venditti V, Ghirlando R, Clore GM. Structural basis for enzyme I inhibition by alpha-ketoglutarate. *ACS Chem Biol*. 2013;8:1232-40.
- [27] van Aalten DM, Amadei A, Linssen AB, Eijssink VG, Vriend G, Berendsen HJ. The essential dynamics of thermolysin: confirmation of the hinge-bending motion and comparison of simulations in vacuum and water. *Proteins*. 1995;22:45-54.
- [28] Dotas RR, Nguyen TT, Stewart Jr. CE, Ghirlando R, Potoyan DA, Venditti V. Hybrid thermophilic/mesophilic enzymes reveal a role for conformational disorder in regulation of bacterial Enzyme I. *J Mol Biol*. 2020;in press.
- [29] Doucette CD, Schwab DJ, Wingreen NS, Rabinowitz JD. alpha-Ketoglutarate coordinates carbon and nitrogen utilization via enzyme I inhibition. *Nat Chem Biol*. 2011;7:894-901.
- [30] Jhoti H, Williams G, Rees DC, Murray CW. The 'rule of three' for fragment-based drug discovery: where are we now? *Nat Rev Drug Discov*. 2013;12:644-.
- [31] Garrett DS, Seok YJ, Peterkofsky A, Gronenborn AM, Clore GM. Solution structure of the 40,000 Mr phosphoryl transfer complex between the N-terminal domain of enzyme I and HPr. *Nat Struct Biol*. 1999;6:166-73.

- [32] Venditti V, Fawzi NL, Clore GM. Automated sequence- and stereo-specific assignment of methyl-labeled proteins by paramagnetic relaxation and methyl-methyl nuclear Overhauser enhancement spectroscopy. *J Biomol NMR*. 2011;51:319-28.
- [33] Delaglio F, Grzesiek S, Vuister GW, Zhu G, Pfeifer J, Bax A. NMRPipe: A multidimensional spectral processing system based on UNIX pipes. *Journal Biomol NMR*. 1995;6:277-93.
- [34] Mulder FAA, Schipper D, Bott R, Boelens R. Altered flexibility in the substrate-binding site of related native and engineered high-alkaline *Bacillus subtilis*ins. *J Mol Biol*. 1999;292:111-23.
- [35] Case DA, Cheatham Iii TE, Darden T, Gohlke H, Luo R, Merz Jr KM, et al. The Amber biomolecular simulation programs. *J Comput Chem*. 2005;26:1668-88.
- [36] Maier JA, Martinez C, Kasavajhala K, Wickstrom L, Hauser KE, Simmerling C. ff14SB: Improving the Accuracy of Protein Side Chain and Backbone Parameters from ff99SB. *J Chem*. 2015;11:3696-713.
- [37] Morris GM, Huey R, Lindstrom W, Sanner MF, Belew RK, Goodsell DS, et al. AutoDock4 and AutoDockTools4: Automated docking with selective receptor flexibility. *J Comput Chem*. 2009;30:2785-91.
- [38] Jakalian A, Jack DB, Bayly CI. Fast, efficient generation of high-quality atomic charges. AM1-BCC model: II. Parameterization and validation. *J Comput Chem*. 2002;23:1623-41.
- [39] Huang L, Roux B. Automated Force Field Parameterization for Nonpolarizable and Polarizable Atomic Models Based on Ab Initio Target Data. *J Chem*. 2013;9:3543-56.
- [40] Mark P, Nilsson L. Structure and Dynamics of the TIP3P, SPC, and SPC/E Water Models at 298 K. *J Phys Chem A*. 2001;105:9954-60.
- [41] Ryckaert J-P, Ciccotti G, Berendsen HJC. Numerical integration of the cartesian equations of motion of a system with constraints: molecular dynamics of n-alkanes. *J Comput Phys*. 1977;23:327-41.
- [42] Berendsen HJC, Postma JPM, van Gunsteren WF, DiNola A, Haak JR. Molecular dynamics with coupling to an external bath. *J Chem Phys*. 1984;81:3684-90.
- [43] Essmann U, Perera L, Berkowitz ML, Darden T, Lee H, Pedersen LG. A smooth particle mesh Ewald method. *J Chem Phys*. 1995;103:8577-93.
- [44] Roe DR, Cheatham TE. PTRAJ and CPPTRAJ: Software for Processing and Analysis of Molecular Dynamics Trajectory Data. *J Chem*. 2013;9:3084-95.



## Figures

### Fragment screening pipeline

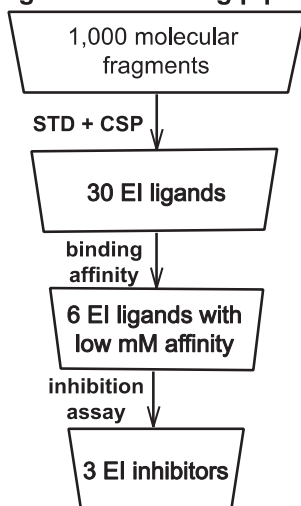


**Figure 1. Fragment screening pipeline.** Scheme of the experimental protocol employed for discovery of novel inhibitors of EI. A library of 1,000 molecular fragments is screened against EI by STD and CSP NMR experiments. The affinity of 30 positive hits for the enzyme is characterized by NMR titration experiments. 6 low-millimolar ligands are tested for their ability to inhibit the phosphoryl-transfer reaction catalyzed by the enzyme, resulting in discovery of 3 allosteric inhibitors of EI.

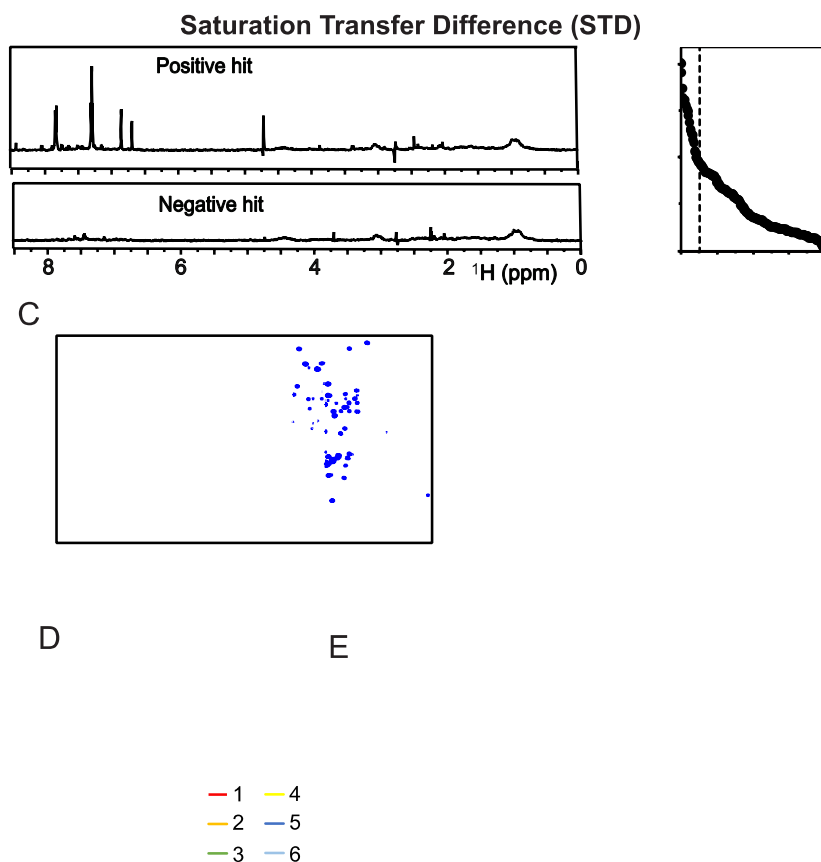


**Figure 2. STD/CSP screening against EI.** (a) Example STD-NMR spectra of a positive (top) and a negative (bottom) hit of the fragment screening. (b) The intensity of the STD spectra is plotted versus the pool index. Pools are ordered for decreasing intensity of the STD spectrum. The vertical dashed line indicates the best 25 pools that were counterscreened by CSP. (c) <sup>1</sup>H-<sup>15</sup>N HSQC spectra of <sup>15</sup>N-labeled EIC acquired in the absence (red) and in the presence (blues) of a pool of molecular fragments. Example of a negative (left) and a positive (red) hit are provided. (d) Binding isotherms obtained for the best six ligands of EI by NMR titration experiments (compounds 1-6). Experimental data are shown as circles. Modelling of the data is shown as solid lines. Color code is red, orange, green, yellow, blue, and light blue for compound 1, 2, 3, 4, 5, and 6, respectively. (e) Line structures of compounds 1-6. *K<sub>D</sub>* values fitted from the binding isotherms are shown.

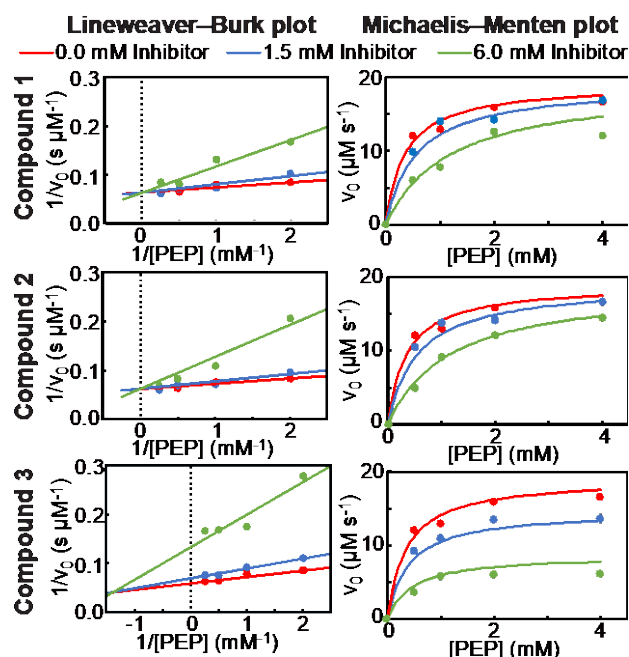


**Figure 3. Enzyme inhibition assays.** Enzyme inhibition assays run in the presence of compound 1 (top), 2 (center), and 3 (bottom) are shown as Lineweaver-Burk (left) and Michaelis-Menten (right) plots. Data were measured at three different concentrations of inhibitor (0.0 mM, red; 1.5 mM, blue; 6.0 mM, green) and fitted simultaneously to a competitive or mixed inhibition model (see equations 3 and 4). Experimental data are shown as circles. Modelled data are shown as solid lines. The vertical dotted lines indicate the position of the y-axis.

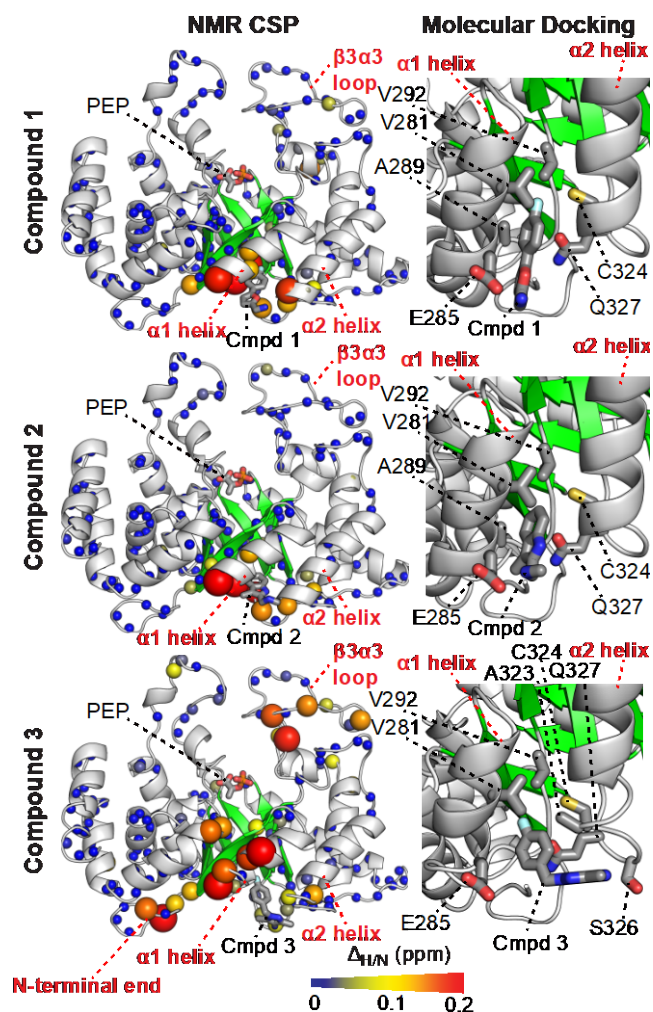


**Figure 4. Structures of the EIC-inhibitor complexes.** In the left panel are reported the weighted combined chemical shift perturbations ( $\Delta_{H/N}$ ) induced by 8 mM of compound 1 (top), 2 (center) and 3 (bottom) on the  $^1\text{H}$ - $^{15}\text{N}$  HSQC spectrum of EIC.  $\Delta_{H/N}$  values are displayed on the structure of the EIC-PEP complex as spheres with the relationship between size and color of each sphere and chemical shift perturbation depicted by the color bar. The PEP molecule is shown as solid sticks. Structure and localization of compounds 1, 2, and 3 resulting from molecular docking calculation is also displayed as solid sticks. In the right panel a close-up view of the inhibitor binding site is provided. Inhibitors and EIC side-chains involved in complex formation are shown as solid sticks.

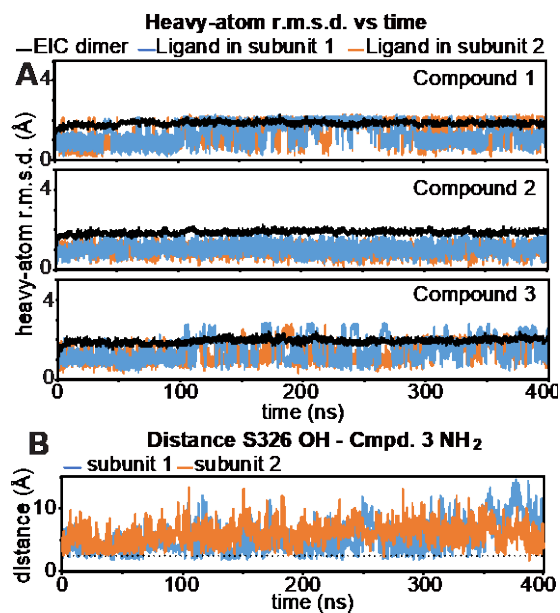


**Figure 5. MD simulations of the EIC-inhibitor complexes.** (a) Heavy-atom r.m.s.d. to the docking structure versus time calculated for the 400-ns MD run on the EIC-inhibitor complexes. EIC was simulated in its physiological dimeric form with inhibitors bound to both subunits. The r.m.s.d. calculated for the EIC, the inhibitor bound to the first subunit, and the inhibitor bound to the second subunit are colored black, light blue, and orange, respectively. Top, center, and bottom plots are for the complexes with compound 1, 2, and 3, respectively. (b) The distance between the hydroxyl group of S326 and the amine group of compound 3 is plotted versus time. Data for subunit 1 and 2 are colored light blue and orange, respectively. The dotted line is at 2.4 Å to indicate the distance required for hydrogen-bond formation.

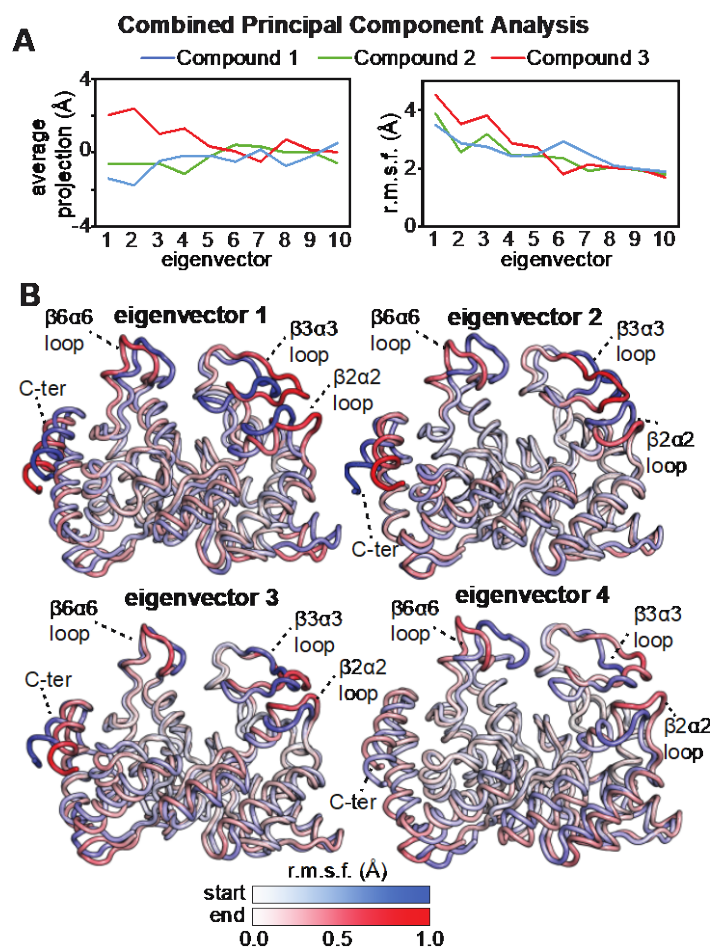


**Figure 6. Combined PCA analysis of the MD trajectories.** (a) Average projection (left) and root mean square fluctuations (r.m.s.f.) (right) obtained by projecting the MD trajectories of EIC bound to compound 1 (blue), 2 (green), and 3 (red) on a common set of eigenvectors obtained from the concatenated trajectory (see main text). Combined PCA analysis was performed using the coordinates of the C $\alpha$  atoms of EIC. Results for the first 10 eigenvectors are shown. (b) Start (blue) and end (red) points of the pseudo-trajectories describing eigenvectors 1-4. Residue-specific r.m.s.f. values in the eigenvector calculated over the concatenated trajectory are plotted as color gradient on the start and end structures to emphasize the specific contribution of different EIC regions to each eigenvector.

**X: allosteric pocket**    **— EIN**    **— EIC**    **--- relevant secondary structures**

E.coli	236	IDKMRAVQEQVASEKAELAKLKDLPAITLDGHQVEVCANIGTVRD	VEGAERNGAEGVGLY	295
C.freundii	236	IEQLRAVQEQVATEKAELAKLKDLPAITLDGHQVEVCANIGTVRD	VEGAERNGAEGVGLY	295
K.pneumoniae	236	IEALRSIQAQVAEEKAEELAKLKDLPAITLDGHQVEVCANIGTVRD	VEGAERNGAEGVGLY	295
S.aureus	238	LIAYQDKRERYFADKKELQKLRDADTVTVDGVHAELAANIGTPND	LPGVIENTGAQGI	397
E.faecalis	238	KSEFEAEAKAYADQKAEDWKLKNAETVTADGKHVELAANIGTPKD	LEGVHKNGGEAVGLY	297
N.gonorrhoeae	241	INEYRRRRAREYRSHKRDNLKLTAAATADGVCIELVGNIESAED	VKPLHNLGADGIGLF	300
			α-helix 1    β-strand 2	
E.coli	296	RTEFLFMDRDALPTEEEQFAAYKAVAEA	CGSQAVIVRTMDIGGDKELPYMNFPEE----	351
C.freundii	296	RTEFLFMDRESLPTEEEQFAAYKAVAEA	CGSQAVIVRTMDIGGDKELPYMNFPEE----	351
K.pneumoniae	296	RTEFLFMDRDALPTEEEQFAAYKAVAEA	CGSQAVIVRTMDIGGDKELPYMNFPEE----	351
S.aureus	298	RTEFLYMGRDQMPTEEEQFEAYKEVLEA	MGGKRVVVRTLDIGGDKELSYLNLPEEM----	353
E.faecalis	298	RTEFLYMDSSDFPTEEDQYQAYKAVLEG	MEGKPVVVRTMDIGGDKELPYLTLPEEM----	353
N.gonorrhoeae	301	RSEFLYLNRDTMPSEDEQEYVSAIVKK	MKGKSVTIRTVDLGVGDKNPRW--FGKNSTPNG	358
		α-helix 2		

**Figure 7. EI sequence alignment.** The sequence of the E. coli EI is aligned against EI from other, randomly selected, drug-resistant bacteria: *Citrobacter freundii* (identity 97%; similarity 99%; gaps 0%), *Klebsiella pneumoniae* (identity 96%; Similarity 98%; gaps 0%), *Staphylococcus aureus* (identity 51%; similarity 70%; gaps 0%), *Enterococcus faecalis* (identity 49%; similarity 68%; gaps 1%), and *Neisseria gonorrhoeae* (identity 36%; similarity 58%; gaps 2%). Residues forming the allosteric pocket are in red. Blue and red lines indicate the EIN and EIC domains, respectively. Dashed lines indicate the locations of  $\alpha$ -helices 1 and 2 and  $\beta$ -strand 1. Full sequence alignments are shown in Supplementary Figure S1.

E.coli	1	MISGILASPGIAFGKALLLKEDEIVDRKKISADQVDQEVERFLSGRAKASAQLETKTK	60
C.freundii	1	MISGILASPGIAFGKALLLKEDEIVDRKKISADKVDQEVERFLSGRAKASAQLEAIKTK	60
K.pneumoniae	1	MISGILASPGIAFGKALLLKEDEIVDRKKISADKVDQEVERFLSGRAKASAQLEVIKTK	60
S.aureus	4	LKGTAAASDGVAAKAYLLVEPDLTFDKNEKVTD-VEGEVAKFNSAIEASKVELTKIRNN	62
E.faecalis	4	MLKGTAAASDGVAAKAYLLVQPDLSFN--KTSVEDTDAEATRLDDALAKSTFEELQAIRDK	61
N.gonorrhoeae	4	VLHGVAAGKGIAVGCAHLIARGTEEVPPQYDVAQADTDAEAERFDAAVKATRKELEQLRSA	63
E.coli	61	AGETFGEKEKAIFFEGHIMLLEDEELEQEIIALIKDKHMTADAAAHEVIEGQASALEELDD	120
C.freundii	61	AGETFGEKEKAIFFEGHIMLLEDEELEQEIIALIKDKHMTADAAAHEVIEGQATALEELDD	120
K.pneumoniae	61	AGETFGEKEKAIFFEGHIMLLEDEELEQEIIALIKDKHMTADAAAHEVIDGQATALEELDD	120
S.aureus	63	AEVQLGADKAAIFDAHLILVLDPELIQPTQDKIKNNENANAATALTDTVTTFVTTIFESMDN	122
E.faecalis	62	AAQSLGEAEAQVFD AHLMLVSDPEMVGQIKQNIQDNKVNAEAALEKVTDMYIGMFAMDD	121
N.gonorrhoeae	64	IPENAPTELGAFTISLHMLLTDTVTLREPVDTLREQKINAEWALKQQSDKLAQAQFDNMD	123
E.coli	121	E-YLKERAADVDRDIGKRLLRNILG----LKIIDLSAIQDEVILVAADLTPSETAQLNLKK	175
C.freundii	121	E-YLKERAADVDRDIGKRLLRNILG----LAIIDLSAIQEEVILVAADLTPSETAQLNLNK	175
K.pneumoniae	121	E-YLKERAADVDRDIGKRLLRNILG----LAIIDLSAIQDEVILVAADLTPSETAQLNLKK	175
S.aureus	123	E-YMKERAADIRDVSKRVLSHILG----VELPNPSMIDESVIVGNDLTPSDTAQLNKEF	177
E.faecalis	122	NAYMQERAADIRDVAKRIIAHLILG----VTLPNPSMINEEVIVVAHDLTPSDTAQLDRTY	177
N.gonorrhoeae	124	A-YLKERKQDMLQVVRRIHNNLIGQGNELEVAD--NLFDETVLIANDLSPADTVLFKEQR	180
E.coli	176	VLGFITDAGGRTSHTSIMARSLEIPAIVGTSVTSQVKNDDYLILDAVNNQVYVNPTEFV	235
C.freundii	176	VLGFITDAGGRTSHTSIMARSLEIPAIVGTSVTSQVKNDDYLILDAVNNQVYVNPTEFV	235
K.pneumoniae	176	VLGFITDAGGRTSHTSIMARSLEIPAIVGTSITAQVKNDDYLILDAVNNQVILNPSNEQ	235
S.aureus	178	VLGFATNIGGRTSHTSIMARSLEIPAIVGTSITQEVKQGDMIIVDGLNGDVIVNPTEDE	237
E.faecalis	178	VKAFTVDIGGRTSHTSIMARSLEIPAIVGTSITQEVKQGDILAVNGIIGDVIIDPTDAE	237
N.gonorrhoeae	181	IAAFVTDAGGPTGHTAILGRSLDIPSVVGLHNARKLITEGETVIVDGINGVLIISPDES	240
E.coli	236	IDKMRVQEQVASEKAELAKLKDLPATITLDGHQVEVCANIGTVRDVEGAERNGAEGVGLY	295
C.freundii	236	IEQLRAVQEQVATEKAELAKLKDLPATITLDGHQVEVCANIGTVRDVEGAERNGAEGVGLY	295
K.pneumoniae	236	IEALRSIQVAAEKAELAKLKDLPATITLDGHQVEVCANIGTVRDVEGAERNGAEGVGLY	295
S.aureus	238	LIAQDKRERYFADKKELQKLRDADTVTVDGVAELAANI GTPNDLPGVLENGAQGIGLY	397
E.faecalis	238	KSEFEAEAKAYADQKAEDKLKNAETVTADGKHVELAANI GTPKDLGVBKNGEAVGLY	297
N.gonorrhoeae	241	LNEYRRRAREYRSHKRDNLKLTAAATADGVCI ELVGNIESAEDVKPLBNLGA DGI GLF	300
E.coli	296	RTEFLMDRDALPTEEEQFAAYKAVAEACGSQAVIVRTMDIGGDKELPYMNFPEE----	351
C.freundii	296	RTEFLMDRESLPTEEEQFAAYKAVAEACGSQAVIVRTMDIGGDKELPYMNFPEE----	351
K.pneumoniae	296	RTEFLMDRDALPTEEEQFAAYKAVAEACGSQAVIVRTMDIGGDKELPYMNFPEE----	351
S.aureus	298	RTEFLYMGDRDQMPTEEEQFAAYKEVLEAMGCKRVVVRTLDIGGDKELSYLNLPEEM----	353
E.faecalis	298	RTEFLYMDSSDEPTEEDQYQAYKAVLEGMCKRPVVVRTMDIGGDKELPYLTPHEM----	353
N.gonorrhoeae	301	RSEFLYLNRDTPSEDEQYEVYSAIVKMKCKSVTIRTVDLGVDKNPRW--FGKNSTPNG	358
E.coli	352	--NPFLGWRAIRIAMDR--REILRDQRLRAILRASAFGKLRIMFPMIISVEEVRALRKEIE	407
C.freundii	352	--NPFLGWRAVRIAMDR--KEILRDQVRRAILRASAFGKLRIMFPMIISVEEVRALRKEIE	407
K.pneumoniae	352	--NPFLGWRAVRIAMDR--KEILRDQVRRAILRASAFGKLRIMFPMIISVEEVRALRKEIE	407
S.aureus	354	--NPFLGWRAIRLCLAQ--QDIFRPQLRALLRASVYGKLNIMFPMVATINEFREAKAILL	409
E.faecalis	354	--NPFLGWRAIRLISLSELGDMFRTQMRALLRASVHGNLRIMFPMVATLKEFRAAKAIFE	411
N.gonorrhoeae	359	SLNPALGMTGIRLCLAE--PVMFRTQMRALLRAAVHGPVRMMWPMITSVSEVRQCLIHL	415
E.coli	408	IYKQELRDEGKAFDESIEIGVMEVTPAAAT IARHLAKEVDFEFSIGTNDLIQYTLAVDRGN	467
C.freundii	408	IYKQELRDEGKAFDESIEIGVMEVTPAAAT IARHLAKEVDFEFSIGTNDLIQYTLAVDRGN	467
K.pneumoniae	408	IYKQELRDEGKAFDESIEIGVMEVTPAAAT IARHLAKEVDFEFSIGTNDLIQYTLAVDRGN	467
S.aureus	410	EEKENLNKNEGHDISDDIELGIMVEIPATAALADVFAKEVDFEFSIGTNDLIQYTLAADRMS	469
E.faecalis	412	DEKQKLVNEGVEVSNDIQVGIMIEIPAAAVLADKFAKEVDFEFSVGTNDLIQYTMADRMN	471
N.gonorrhoeae	416	TAQRQLAERGDAGE-VGIGCMIEIPSAALTGVGSLKLVDVFSVGTNDLIQYILSVDRGD	475
E.coli	468	DMISHLYQPMSPSVLNLKQVIDASHAEGKWTGMCGLAGDERATLLLLGMGLDEFMSMA	527
C.freundii	468	DMISHLYQPMSPSVLNLKQVIDASHAEGKWTGMCGLAGDERATLLLLGMGLDEFMSMA	527
K.pneumoniae	468	DMISHLYQPMSPSVLNLKQVIDASHAEGKWTGMCGLAGDERATLLLLGMGLDEFMSMA	527
S.aureus	470	ERVSILYQPYNPISILRLVKQVIEASHKEGKWTGMCCEMAGDETAIPLLLGLGLDEFMSMA	529
E.faecalis	472	ERVSILYQPYNPISILRLIKNVIDAAHAEGKWAGMCEMAGDQTAVPLLLGMGLDEFMSMA	531
N.gonorrhoeae	476	DSVSHLYQPGHPSVLKMLQHVIRTANRMDKDVSVCEMAGDTAFTRVLLGMGLRRFSMNP	535
E.coli	528	ISIPRIKKIIRNTNFEDAKVLAEQALAQ-PTTDELMTLVNKFIEEKTIC	575
C.freundii	528	ISIPRIKKIIRNTNFEDAKVLAEQALAQ-PTTDELMTLVNKFIEEKTIC	575
K.pneumoniae	528	ISIPRIKKIIRNTNFEDAKVLAEQALAQ-PTTDELMTLVNKFIEEKTIC	575
S.aureus	530	TSILKARRQINGLSKNEMTELANRAVDC-ATQEEVIELVNNYVK	572
E.faecalis	522	TSILKTRSLMKRLDTTKMAELADRALKECDTMEEFVALVEEY	573
N.gonorrhoeae	536	NNILPVKNIIILHSN	549

**Figure S1. EI sequence alignment.** The sequence of the *E. coli* EI is aligned against EI from other, randomly selected, drug-resistant bacteria: *Citrobacter freundii* (identity 97%; similarity



99%; gaps 0%), *Klebsiella pneumoniae* (identity 96%; Similarity 98%; gaps 0%),  
*Staphylococcus aureus* (identity 51%; similarity 70%; gaps 0%), *Enterococcus faecalis* (identity 49%; similarity 68%; gaps 1%), and *Neisseria gonorrhoeae* (identity 36%; similarity 58%; gaps 2%). Residues forming the allosteric pocket are in red. Active site residues are in bold. Blue and red lines indicate the EIN and EIC domains, respectively.

## CHAPTER 5. GENERAL CONCLUSION

EI is emerging as an important model system to study allosteric regulation in multidomain, oligomeric enzymes, and as a promising pharmaceutical target for antimicrobial design. This study has developed a novel method based on fast NMR technique to justify the role of  $\alpha$ KG as an inhibitor or stimulator of EI activity. The results highlight the determining role of the oligomeric states of the enzyme. Specifically, at experimental conditions favoring the dimeric form of EI,  $\alpha$ KG inhibits the phosphoryl transfer activity of the enzyme. In contrast, at experimental conditions favoring monomeric EI, addition of  $\alpha$ KG results in a shift of the monomer-dimer equilibrium toward the enzymatically active dimeric form and a consequential stimulation of enzymatic activity. This study also shows how the activity of small molecule metabolites against their biological targets can change significantly in response to small changes in experimental conditions and illustrates that the dependence of the oligomeric state of the enzyme on the experimental conditions must be considered with great care when interpreting enzyme kinetic data.

Although the monomer-dimer equilibrium of EI plays a crucial role in regulation of its activity and potentially controls the phosphorylation state of the overall PTS, the changes in structure, dynamics, and substrate binding properties that EI undergoes upon monomerization have not been analyzed yet. The high dimer affinity of EI hampers the structural characterization of the monomeric state. Obtaining an atomic-level description of this intermediate state, however, is crucial to fully understand the molecular mechanisms underlying EI catalytic activity and regulation. Our study combined protein engineering and pressure perturbation to shift the dimer-monomer equilibrium of EIC in order to isolate and determine the structural ensemble of the monomeric state in solution. Application of hydrostatic pressure from 1 bar to 2.5 kbar shifts

the equilibrium toward the monomeric state of EIC while preserving the overall tertiary structure of the protein. However, three catalytic loops which become significantly disordered in the monomeric state are unable to orient PEP into the binding site, causing monomeric EI to be inactive. Those catalytic loops seem to play a key role in establishing the allosteric coupling between the active site and the dimerization interface. Overall, our experiments suggest that dimerization is required for these catalytic loops to be maintain a functional form.

In the journey toward blocking the PTS pathway by targeting EI, we have characterized a novel surface pocket localized on the EIC domain that is allosterically coupled to the enzyme active site. By using NMR-based fragment screening, we identified three small molecules that bind to the allosteric pocket and inhibit the phosphoryl-transfer activity of EI. Therefore, the inhibitors identified here can be used as chemical probes to investigate long-range communication in EI. To further promote these inhibitors for antimicrobial applications, evolution of the three inhibitors to enhance their potency and specificity is necessary. Several hints for the development can be inferred from the computational studies on the EIC-inhibitor complexes. Our docking and MD results suggest that introducing a flexible element between the hydrophobic and hydrophilic moieties of the inhibitor favors formation of extensive contacts with  $\alpha$ -helix 2 by allowing the small molecule to adopt a bent conformation. In alternative, branched molecules could be designed starting from compounds 1 and 2 to increase their interactions with the C-terminal end of  $\alpha$ -helix 2 and confer mixed inhibitor character. Finally, in silico screening campaigns targeting the allosteric site at the C-terminal end of  $\alpha$ -helices 1 and 2 of EIC might provide additional clues toward evolution of compounds 1-3 and/or suggest novel lead compounds for inhibition of EI. As the allosteric pocket identified here is conserved across

EI from different bacterial strains, the results and strategies presented in this work may inspire new molecular routes to inhibition of bacterial infections.

### References

1. Bhabha, G.; Lee, J.; Ekiert, D. C.; Gam, J.; Wilson, I. A.; Dyson, H. J.; Benkovic, S. J.; Wright, P. E., A dynamic knockout reveals that conformational fluctuations influence the chemical step of enzyme catalysis. *Science* 2011, 332 (6026), 234-8.
2. Eisenmesser, E. Z.; Millet, O.; Labeikovsky, W.; Korzhnev, D. M.; Wolf-Watz, M.; Bosco, D. A.; Skalicky, J. J.; Kay, L. E.; Kern, D., Intrinsic dynamics of an enzyme underlies catalysis. *Nature* 2005, 438 (7064), 117-21.
3. Fraser, J. S.; Clarkson, M. W.; Degnan, S. C.; Erion, R.; Kern, D.; Alber, T., Hidden alternative structures of proline isomerase essential for catalysis. *Nature* 2009, 462 (7273), 669-73.
4. Henzler-Wildman, K. A.; Lei, M.; Thai, V.; Kerns, S. J.; Karplus, M.; Kern, D., A hierarchy of timescales in protein dynamics is linked to enzyme catalysis. *Nature* 2007, 450 (7171), 913-6.
5. Henzler-Wildman, K. A.; Thai, V.; Lei, M.; Ott, M.; Wolf-Watz, M.; Fenn, T.; Pozharski, E.; Wilson, M. A.; Petsko, G. A.; Karplus, M.; Hubner, C. G.; Kern, D., Intrinsic motions along an enzymatic reaction trajectory. *Nature* 2007, 450 (7171), 838-44.
6. Tuttle, L. M.; Dyson, H. J.; Wright, P. E., Side-chain conformational heterogeneity of intermediates in the Escherichia coli dihydrofolate reductase catalytic cycle. *Biochemistry* 2013, 52 (20), 3464-77.
7. Clore, G. M.; Venditti, V., Structure, dynamics and biophysics of the cytoplasmic protein-protein complexes of the bacterial phosphoenolpyruvate: sugar phosphotransferase system. *Trends Biochem Sci* 2013, 38 (10), 515-30.
8. van den Bedem, H.; Fraser, J. S., Integrative, dynamic structural biology at atomic resolution--it's about time. *Nat Methods* 2015, 12 (4), 307-18.
9. Venditti, V.; Clore, G. M., Conformational selection and substrate binding regulate the monomer/dimer equilibrium of the C-terminal domain of Escherichia coli enzyme I. *J Biol Chem* 2012, 287 (32), 26989-98.
10. Motlagh, H. N.; Wrabl, J. O.; Li, J.; Hilser, V. J., The ensemble nature of allostery. *Nature* 2014, 508 (7496), 331-9.
11. Dill, K. A., Polymer principles and protein folding. *Protein Sci* 1999, 8 (6), 1166-80.
12. Frauenfelder, H.; Sligar, S. G.; Wolynes, P. G., The energy landscapes and motions of proteins. *Science* 1991, 254 (5038), 1598-603.

13. Tang, C.; Schwieters, C. D.; Clore, G. M., Open-to-closed transition in apo maltose-binding protein observed by paramagnetic NMR. *Nature* 2007, 449 (7165), 1078-82.
14. Tsai, C. J.; Ma, B.; Nussinov, R., Folding and binding cascades: shifts in energy landscapes. *Proc Natl Acad Sci U S A* 1999, 96 (18), 9970-2.
15. Suh, J. Y.; Tang, C.; Clore, G. M., Role of electrostatic interactions in transient encounter complexes in protein-protein association investigated by paramagnetic relaxation enhancement. *Journal of the American Chemical Society* 2007, 129 (43), 12954-5.
16. Tsai, C. J.; Del Sol, A.; Nussinov, R., Protein allostery, signal transmission and dynamics: a classification scheme of allosteric mechanisms. *Mol Biosyst* 2009, 5 (3), 207-16.
17. Deutscher, J.; Ake, F. M.; Derkaoui, M.; Zebre, A. C.; Cao, T. N.; Bouraoui, H.; Kentache, T.; Mokhtari, A.; Milohanic, E.; Joyet, P., The bacterial phosphoenolpyruvate:carbohydrate phosphotransferase system: regulation by protein phosphorylation and phosphorylation-dependent protein-protein interactions. *Microbiol Mol Biol Rev* 2014, 78 (2), 231-56.
18. Clore, G. M.; Venditti, V., Structure, dynamics and biophysics of the cytoplasmic protein-protein complexes of the bacterial phosphoenolpyruvate: sugar phosphotransferase system. *Trends Biochem Sci* 2013, 38 (10), 515-30.
19. Postma, P. W.; Lengeler, J. W.; Jacobson, G. R., Phosphoenolpyruvate:Carbohydrate Phosphotransferase Systems. In *Escherichia coli and Salmonella: Cellular and Molecular Biology*, Neidhardt, F. C.; Lin, E. C.; Curtiss, R., Eds. 1996; pp 1149-1174.
20. Deutscher, J.; Ake, F. M.; Derkaoui, M.; Zebre, A. C.; Cao, T. N.; Bouraoui, H.; Kentache, T.; Mokhtari, A.; Milohanic, E.; Joyet, P., The bacterial phosphoenolpyruvate:carbohydrate phosphotransferase system: regulation by protein phosphorylation and phosphorylation-dependent protein-protein interactions. *Microbiol Mol Biol Rev* 2014, 78 (2), 231-56.
21. Hogema, B. M.; Arents, J. C.; Bader, R.; Eijkemans, K.; Yoshida, H.; Takahashi, H.; Aiba, H.; Postma, P. W., Inducer exclusion in *Escherichia coli* by non-PTS substrates: the role of the PEP to pyruvate ratio in determining the phosphorylation state of enzyme IIAGlc. *Mol Microbiol* 1998, 30 (3), 487-98.
22. Postma, P. W.; Lengeler, J. W.; Jacobson, G. R., Phosphoenolpyruvate:Carbohydrate Phosphotransferase Systems. In *Escherichia coli and Salmonella: Cellular and Molecular Biology*, Neidhardt, F. C.; Lin, E. C.; Curtiss, R., Eds. 1996; pp 1149-1174.
23. Huang, K. J.; Lin, S. H.; Lin, M. R.; Ku, H.; Szkaradek, N.; Marona, H.; Hsu, A.; Shiuan, D., Xanthone derivatives could be potential antibiotics: virtual screening for the inhibitors of enzyme I of bacterial phosphoenolpyruvate-dependent phosphotransferase system. *J Antibiot* 2013, 66 (8), 453-8.
24. Kok, M.; Bron, G.; Erni, B.; Mukhija, S., Effect of enzyme I of the bacterial phosphoenolpyruvate : sugar phosphotransferase system (PTS) on virulence in a murine model. *Microbiology* 2003, 149 (Pt 9), 2645- 52.

25. Edelstein, P. H.; Edelstein, M. A.; Higa, F.; Falkow, S., Discovery of virulence genes of *Legionella pneumophila* by using signature tagged mutagenesis in a guinea pig pneumonia model. *Proc Natl Acad Sci U S A* 1999, 96 (14), 8190-5.
26. Hava, D. L.; Camilli, A., Large-scale identification of serotype 4 *Streptococcus pneumoniae* virulence factors. *Mol Microbiol* 2002, 45 (5), 1389-406.
27. Jones, A. L.; Knoll, K. M.; Rubens, C. E., Identification of *Streptococcus agalactiae* virulence genes in the neonatal rat sepsis model using signature-tagged mutagenesis. *Mol Microbiol* 2000, 37 (6), 1444- 55.
28. Lau, G. W.; Haataja, S.; Lonetto, M.; Kensit, S. E.; Marra, A.; Bryant, A. P.; McDevitt, D.; Morrison, D. A.; Holden, D. W., A functional genomic analysis of type 3 *Streptococcus pneumoniae* virulence. *Mol Microbiol* 2001, 40 (3), 555-71.
29. Mukhija, S.; Germeroth, L.; Schneider-Mergener, J.; Erni, B., Identification of peptides inhibiting enzyme I of the bacterial phosphotransferase system using combinatorial cellulose-bound peptide libraries. *Eur J Biochem* 1998, 254 (2), 433-8.
30. Huang, K. J.; Lin, S. H.; Lin, M. R.; Ku, H.; Szkaradek, N.; Marona, H.; Hsu, A.; Shiuan, D., Xanthone derivatives could be potential antibiotics: virtual screening for the inhibitors of enzyme I of bacterial phosphoenolpyruvate-dependent phosphotransferase system. *J Antibiot* 2013, 66 (8), 453-8.
31. Kee, J. M.; Muir, T. W., Chasing phosphohistidine, an elusive sibling in the phosphoamino acid family. *ACS Chem Biol* 2012, 7 (1), 44-51.
32. Venditti, V.; Clore, G. M., Conformational selection and substrate binding regulate the monomer/dimer equilibrium of the C-terminal domain of *Escherichia coli* enzyme I. *J Biol Chem* 2012, 287 (32), 26989-98.